**Republic of Türkiye's 100th Anniversary.
We are stronger together, our beloved
Turkish Nation.**

PROCEEDINGS

OF THE 16th INTERNATIONAL CONFERENCE ON NUCLEAR STRUCTURE PROPERTIES

NSP2023

May 8 – 10, 2023

Karabük University

Science Faculty, Physics Department

Karabük, Türkiye

KARABÜK ÜNİVERSİTESİ

16th International Conference on **Nuclear Structure Properties**

PREFACE

The NSP conference series is a technical event which focuses on advances in nuclear structure, astrophysics, nuclear reactions, nuclear energy, high energy & physics, and other related topics.

The purpose of this conference series is to provide a platform for researchers, academicians, and practitioners to make them familiar with recent advances in nuclear sciences. The organization committee accepts a wide range of papers to encourage young and experienced researchers to present their work and the possibility of initiating mutual collaboration with internationally renowned researchers and experts of the relevant industries. The conference format comprises of multiple sessions and the selected works in these sessions are based on substantial and novel research.

The series of events was initiated in 2004 at Anadolu University, Eskişehir / Türkiye. The following is a list of subsequent meetings in the series:

I. Workshop on Nuclear Structure Properties (NSP2004),
Anadolu University, Eskişehir, Türkiye

II. Workshop on Nuclear Structure Properties (NSP2005),
Anadolu University, Eskişehir, Türkiye

III. Workshop on Nuclear Structure Properties (NSP2006),
Dumlupınar University, Kütahya, Türkiye

IV. Workshop on Nuclear Structure Properties (NSP2007),
Gazi University, Ankara, Türkiye

V. Workshop on Nuclear Structure Properties (NSP2011),
Muş Alparslan University, Muş, Türkiye

VI. International Workshop on Nuclear Structure Properties (NSP2013),
Karabük University, Karabük, Türkiye

VII. International Workshop on Nuclear Structure Properties (NSP2014),
Sinop University, Sinop, Türkiye

VIII. International Workshop on Nuclear Structure Properties (NSP2015),
Sakarya University, Sakarya, Türkiye

IX. International Conference on Nuclear Structure Properties (NSP2016),
Sivas Cumhuriyet University, Sivas, Türkiye

X. International Conference on Nuclear Structure Properties (NSP2017),
Karabük University University, Karabük, Türkiye

XI. International Conference on Nuclear Structure Properties (NSP2018),
Karadeniz Technical University, Trabzon, Türkiye

XII. International Conference on Nuclear Structure Properties (NSP2019),
Bitlis Eren University, Bitlis, Türkiye

XIII. International Conference on Nuclear Structure Properties (NSP2020)
It has been attributed to Covid-19.

XIV. International Conference on Nuclear Structure Properties (NSP2021)
as an online event due to Covid-19 – Selçuk University, Konya, Türkiye

XV. International Conference on Nuclear Structure Properties (NSP2022),
Kırıkkale University, Kırıkkale, Türkiye

We were wishing that 16th NSP conference would be a face-to-face event in which we could enjoy international collaborations between young and renowned researchers in a direct and more accessible way. However, on **February 6 - 2023**, Türkiye hit and affected by a massive earthquake. As shattered by the devastating images of the quake and trying to manage the aftermath, it was now impossible to organize this event in a way that we can manage accommodations, travel problems, and other issues related to having some or all participants required to be in the same physical location. Therefore, we decided to conduct 16th of the series as **an online event** starting on May 8, 2023 and ending on May 10, 2023. **Collected fees were directed to AFAD as aid for the survivals of the earthquake.**

Hosted and organized by the Physics Department of University of Karabük, the conference was comprised of a series of online presentations contributed by researchers from different countries. **11** renowned researchers across different countries were invited to give talks on various subjects that can give directions to future scientific studies. **40** speakers from **18** different countries presented their works (**48 speeches in total**). The countries represented by their respective fellow researchers were *Türkiye, USA, United Kingdom, France, Japan, Italy, Greece, Russia, Croatia, Romania, Malaysia, Pakistan, Iraq, Iran, Azerbaijan, Uzbekistan,* *Algeria, Nigeria*. There were also non-speaker participants from these countries along with other non-speaker participants from *Germany, Australia, China, Brazil, the Czech Republic, Slovakia, Bulgaria, and Kazakhstan*. These participants had a chance of watching and listening to presentations, asking some important questions on the possible future directions of presented works, and igniting useful discussions. In total, the number of participants were **99** attending from across **26** different countries.

The event was conducted with the aim of honouring **100th anniversary of foundation of Turkish Republic**, and we believe, we achieved that. The topics of the meeting were more diverse compared to the previously held ones, but we managed to keep the integrity of the series intact. The quality of the works presented was evident. Respected researchers around the world appreciated our sincere efforts and praised useful discussions among peers that made the event even more delightful. Our hope is that this meeting will have a positive impact on future collaborations among participants and guide our young Turkish researchers to the right path on their respective scientific studies.

Thanks to **Mustafa Kemal ATATÜRK** and his reforms, we achieved significant advances in science in the first century of our republic’s history. We wish a brighter future for our beloved country and its young researchers.

Prof. Dr. Necla ÇAKMAK
Chief of NSP 2023 Conference

ACKNOWLEDGEMENTS

First of all, we would like to thank all participants for their important contributions. Sounded and well-researched works presented in these meetings will encourage future participants to have even more quality in their respective works. The organizers of this conference make every effort to keep conference fees as low as possible to facilitate the attendance of young researchers. These efforts were relatively successful, and a lot of new young faces could be seen at the conference.

We also thank the chairs of each session who successfully managed to let each presentation start and finish on time. Thanks to their patience and persisten in keeping track of the time we could have enough time for question-answer sessions that was necessary to ignite useful discussions along the lines of relevant topics. They also helped young presenters when they needed some encouragement during their presentations, and they kindly handled some difficulties that are inherit in any online meeting. The organizing committee also wishes to acknowledge the assistance and encouragement that we have received from our organizations and the many other individuals, who helped prepare this event. In some stages of preparations, there were only a handful of people who could sacrifice their time and they did it without asking favours. We are also very grateful to the reviewers, whose very consistent reviewing of abstracts was of great help in improving the quality of many papers.

Finally, we would like to note that this year is the 100th anniversary of foundation of the Turkish Republic. 100 years ago, Mustafa Kemal ATATÜRK and his fellow fighters fought for the independence of this country with great resolve. Therefore, we like to see this event as a commemoration of their efforts on saving our beloved nation and leading us to create a modern Turkish state. The following quotation united us in the past and will always guide us to the future:

"My moral heritage is science and reason. Anyone willing to appropriate my ideas for themselves after me will be my moral inheritors, provided they would approve the guidance of science and reason on this axis".

Mustafa Kemal ATATÜRK

Prof. Dr. Necla ÇAKMAK
Chief of NSP 2023 Conference

COMMITTEES

Honorary Committee

- Prof. Dr. Refik Polat *(Rector, Karabük University, Karabük, Türkiye)*
- Prof. Dr. Ayşe Nallı *(Dean, Science Faculty, Karabük University, Karabük, Türkiye)*

Advisory Committee – Founders of the NSP Group

- Ali Ekber Kuliyev *(The National Aviation Academy of Azerbaijan, Bakü, Azerbaijan)*
- Cevad Selam *(Independent Researcher – retired from Muş Alparslan University, Muş, Türkiye)*
- Hasan Gümüş *(Independent Researcher – retired from Ondokuz Mayıs University, Samsun, Türkiye)*
- İhsan Uluer *(OSTIM Technical University, Ankara, Türkiye)*
- Saim Selvi *(Independent Researcher – retired from Ege University, İzmir, Türkiye)*
- Saleh Sultansoy *(TOBB University of Economics & Technology, Ankara, Türkiye)*

Scientific Committee

- Abdullah Aydın *(Kırıkkale University, Kırıkkale, Türkiye)*
- Ahmet Hakan Yılmaz *(Karadeniz Technical University, Trabzon, Türkiye)*
- Aybaba Hançerlioğulları *(Kastamonu University, Kastamonu, Türkiye)*
- Dennis Bonatsos *(Institute of Nuclear and Particle Physics, NCSR Demokritos, Greece)*
- Ekber Guliyev *(State Agency for Nuclear and Radiological Activity Regulations, MES, Baku, Republic of Azerbaijan)*
- Emre Tabar *(Sakarya University, Sakarya, Türkiye)*
- Erhan Eser *(Hacı Bayram Veli University, Ankara, Türkiye)*
- Esra Yüksel *(Surrey University, Guilford, United Kingdom)*
- Eyyüp Tel *(Osmaniye Korkut Ata University, Osmaniye, Türkiye)*
- Ergash Makhkamovich Tursunov *(Institute of Nuclear Physics, Academy of Sciences of the Republic of Uzbekistan, Tashkent, Uzbekistan)*
- Fabrice Pelestor *(Toulon, France)*
- Fatima Benrachi *(Universite des Freres Mentouri Constantine, Constantine, Algeria)*
- Francesco Cappuzzello *(Catania University, Catania, Italy)*
- Hatice Duran Yıldız *(Institute of Technology Accelerator, Ankara University, Ankara, Türkiye)*
- İlkay Türk Çakır *(Institute of Technology Accelerator, Ankara Un., Ankara, Türkiye)*
- İsmail Hakkı Sarpün *(Akdeniz University, Antalya, Türkiye)*
- Izyan Hazwani Hashim *(Universiti Teknologi Malaysia, Jahor, Malaysia)*
- Jameel-Un Nabi *(Wah University, Wah, Pakistan)*
- José M. Arias *(Sevilla University, Sevilla, Spain)*
- Kaan Manisa *(Kütahya Dumlupinar University, Kütahya, Türkiye)*
- Khusniddin K. Olimov *(Physical-Technical Institute of Uzbekistan Academy of Sciences, Tashkent, Uzbekistan)*
- Mannap Yusupovich Tashmetov *(Institute of Nuclear Physics, Academy of Sciences of the Republic of Uzbekistan, Tashkent, Uzbekistan)*
- Manuela Cavallaro *(Laboratori Nazionali del Sud - INFN, Catania, Italy)*

- ✓ Mehmet Erdoğan *(Selçuk University, Konya, Türkiye)*
- ✓ Mohammadreza Hadizadeh *(Central State University, Wilberforce, Ohio, USA)*
- ✓ Necati Çelik *(Gümüşhane University, Gümüşhane, Türkiye)*
- ✓ Osman Yılmaz *(Middle East Technical University, Ankara, Türkiye)*
- ✓ Robert Poenaru *(Horia Hulubei National Institute of Physics and Engineering, Magurele, Romania)*
- ✓ Sabin Stoica *(International Centre for Advanced Training and Research in Physics, Bucharest, Romania)*
- ✓ Serdar Ünlü *(Burdur Mehmet Akif Ersoy University, Burdur, Türkiye)*
- ✓ Tahmasib Aliyev *(Middle East Technical University, Ankara, Türkiye)*
- ✓ Takehiko R. Saito *(High Energy Nuclear Physics Laboratory, RIKEN, Saitama, Japan)*
- ✓ Valentin Olegovich Nesterenko *(Joint Institute for Nuclear Research, Dubna, Moskow Region, Russia)*

Organizing Committee

- ✓ Aybaba Hançerlioğulları *(Kastamonu University, Kastamonu, Türkiye)*
- ✓ Mahmut Böyükata *(Kırıkkale University, Kırıkkale, Türkiye)*
- ✓ Nihal Büyükçizmeci *(Selçuk University, Konya, Türkiye)*
- ✓ Serkan Akkoyun *(Sivas Cumhuriyet University, Sivas, Türkiye)*
- ✓ Tuncay Bayram *(Karadeniz Technical University, Trabzon, Türkiye)*

Local Organizing Committee (*Karabük University – Physics Department*)

- ✓ Ahmet Mustafa Erer
- ✓ Hüseyin Yıldırım
- ✓ Khalid Hadi Mahdi Aal-Shabeeb
- ✓ Necla Çakmak ***(Chair)***
- ✓ Savaş Ağduk
- ✓ Ulvi Kanbur
- ✓ Taufiq Abdullah

INVITED SPEAKERS

Esra YÜKSEL

(Surrey University, Guilford, United Kingdom)

Constraining the nuclear symmetry energy using parity-violating electron scattering experiments

Fabrice PÉLESTOR

(Toulon, France)

Anti-Missile Reactive Net

İlkay TÜRK ÇAKIR

(Institute of Technology Accelerator, Ankara University, Ankara, Türkiye)

Future Circular Collider (FCC) Project

Izyan Hazwani HASHIM

(Universiti Teknologi Malaysia, Jahor, Malaysia)

Ordinary Muon Capture Delayed Gamma Ray Analysis for double beta decays (DBDs) and anti-neutrino nuclear responses

Jameel-Un NABI

(University of Wah, Vice Chancellor, Wah, Pakistan)

Half-life of heavy and exotic nuclei to investigate the r-process

Khusniddin K. OLIMOV

(Physical-Technical Institute of Uzbekistan Academy of Sciences, Tashkent, Uzbekistan)

Correlations between parameters of the Tsallis distribution and Hagedorn function with transverse flow in proton-protons collisions at the LHC

Mannap Yusupovich TASHMETOV

(Institute of Nuclear Physics, Academy of Sciences of the Republic of Uzbekistan, Tashkent, Uzbekistan)

The development and implementation of perspective technologies

Manuela CAVALLARO

(Laboratori Nazionali del Sud – INFN, Catania, Italy)

Double charge-exchange reactions for the nuclear matrix elements of neutrinoless double beta decay

Serkan AKKOYUN

(Sivas Cumhuriyet University, Department of Physics, Sivas, Türkiye)

Creating an Online Calculation Tool for Fission Barrier Energy based on Machine Learning Methods

Takehiko R. SAITO

(High Energy Nuclear Physics Laboratory – RIKEN, Saitama, Japan)

Experimental studies of light hypernuclei

Valentin Olegovich NESTERENKO

(Joint Institute for Nuclear Research, Dubna, Moscow Region, Russia)

Anomalous behavior of nuclear moment of inertia

TOPICS

- ✓ Nuclear Structure
- ✓ Nuclear Reactions
- ✓ Nuclear Astrophysics
- ✓ Nuclear Models
- ✓ Nuclear Scattering
- ✓ Nuclear Energy
- ✓ Nuclear Reactors
- ✓ Nuclear Analytical Methods
- ✓ Accelerator Physics
- ✓ Medical and Health Physics
- ✓ High Energy and Particle Physics
- ✓ Nuclear Application in Life Science
- ✓ Radiation Measurements and Dosimeters
- ✓ Nuclear Engineering
- ✓ Other Related Topics

CONTACT

Address: Karabük University, Science Faculty, Head of Physics Department, TR-78050 Karabük / Türkiye

Phone: +90 370 418 91 89

E-mail: nsp2023@karabuk.edu.tr

Website: https://nsp2023.karabuk.edu.tr/en

SCIENTIFIC PROGRAMME

May 8, 2023 Monday

Morning Session 09.15 – 10.50 **Time Zone Istanbul (GMT+3)**
Chair: Necla Çakmak (Karabük Un., Karabük, Türkiye)

09.15 – 09.30 Opening Remarks
09.30 – 09.55 **Takehiko R. Saito** (RIKEN, Japan)
Experimental studies of light hypernuclei

09.55 – 10.20 **Serkan Akkoyun** (Sivas Cumhuriyet Un., Sivas, Türkiye)
Creating an Online Calculation Tool for Fission Barrier Energy based on Machine Learning Methods

10.20 – 10.35 **Mouna Bouhelal** (Echahid Cheikh Larbi Tebessi Un., Algeria)
Theoretical investigation of the T=1/2, A=27 Mirror Nuclei

10.35 – 10.50 **Mouna Bouhelal** (Echahid Cheikh Larbi Tebessi Un., Algeria)
Study of the Energy Spectrum of ^{26}Mg

10.50 – 11.20 COFFEE BREAK
Morning Session 11.20 – 12.30 **Time Zone Istanbul (GMT+3)**
Chair: Serkan Akkoyun (Sivas Cumhuriyet Un., Sivas, Türkiye)

11.20 – 11.35 **Abir Selim** (Echahid Cheikh Larbi Tebessi Un., Tebessa, Algeria)
Shell-Model Study of the Nuclear Structure of ^{25}Al Nucleus

11.35 – 11.50 **Abir Selim** (Echahid Cheikh Larbi Tebessi Un., Tebessa, Algeria)
Investigation of The Energy Spectrum of ^{24}Al Using the PSDPF Interaction

11.50 – 12.05 **Ayşe Çömü** (Selçuk University, Konya, Türkiye)
Analysis of Irradiation Effects on Laroxyl Drug Using EPR Spectroscopy

12.05 – 12.20 **Gamze Ekici** (KTO Karatay University, Konya, Türkiye)
ESR Dating of Old Beyşehir Lake Basin Using Fossil Mollusc Shells

12.30 – 13.30 LUNCH BREAK
Afternoon Session 13.30 – 15.00 **Time Zone Istanbul (GMT+3)**
Chair: Nihal Büyükçizmeci (Selçuk Un., Konya, Türkiye)

13.30 – 13.55 **Fabrice Pelestor** (France)
Anti-Missile Reactive Net

13.55 – 14.20 **Khusniddin K. Olimov** (Uzbekistan Academy of Sciences, Tashkent Uzbekistan)
Correlations between parameters of the Tsallis distribution and Hagedorn function with transverse flow in proton-protons collisions at the LHC

14.20 – 14.35 **Khusniddin K. Olimov** (Uzbekistan Academy of Sciences, Tashkent Uzbekistan)
Dependencies of the average transverse momenta of charged particles on particle species, centrality and collision energy in Au+Au collisions from the BES program at the RHIC

14.35 – 14.50 **Fatima Benrachi** (Frères Mentouri Constantine-1 Un., Algeria)
Nuclear Properties of Even-Even Nuclei in Calcium-40 Region

14.50 – 15.05 **Nadjet Laouet** (Frères Mentouri Constantine-1 Un., Algeria)
Proton Rich A=95 Systems Nuclear Structure: Nushellx@MSU Application

15.10 – 15.30 COFFEE BREAK

Afternoon Session 15.30 – 17.00 **Time Zone Istanbul (GMT+3)**

Chair: Savaş Ağduk (Karabük Un., Karabük, Türkiye)

15.30 – 15.45 **Robert Poenaru** (Horia Hulubei National Institute of Nuclear Physics and Engineering, Romania)
Parity Partner Bands and the Wobbling Motion in 163-Lu

15.45 – 16.00 **Christopher Oluwatobi Adeogun** (Miva University, Nigeria)
Investigation of the Air-Gap Signal in Kalman Filter Under Relative Acceleration

16.00 – 16.15 **Gamze Hoşgör** (Sakarya University, Sakarya, Türkiye)
Polarization Effects on g_R-factors in Odd-Mass Deformed Nuclei

16.15 – 16.30 **Gamze Hoşgör** (Sakarya University, Sakarya, Türkiye)
Understanding the Low-Energy Electromagnetic Dipole Response in ^{155}Sm Nucleus: A Theoretical Perspective

16.30 – 16.45 **Esra Evcin Baydilli** (Hakkari University, Hakkari, Türkiye)
The Detection of the Gamma-Irradiation Effects on Electrical Characteristics of Au/3% Gr-doped PVA/p-Si Type Schottky Structure

May 9, 2023 Tuesday

Morning Session 09.30 – 10.50 **Time Zone Istanbul (GMT+3)**

Chair: Mahmut Böyükata (Kırıkkale Un., Kırıkkale, Türkiye)

09.30 – 09.55 **Jameel-Un Nabi** (University of Wah, Wah Cantt, Pakistan)
Half-life of heavy and exotic nuclei to investigate the r-process

09.55 – 10.20 **Manuela Cavallaro** (Laboratori Nazionali del Sud – INFN, Catania, Italy)
Double charge-exchange reactions for the nuclear matrix elements of neutrinoless double beta decay

10.20 – 10.35 **Francesco Cappuzzello** (Catania University, Catania, Italy)
Heavy-ion induced direct reactions with the MAGNEX spectrometer at INFN-LNS: A multi-channel approach

10.35 – 10.50 **Frederic Lasiaille** (FL Researcher, France)
Relativity in motion

10.50 – 11.20 COFFEE BREAK

Morning Session 11.20 – 12.30 Time Zone Istanbul (GMT+3)

Chair: Tuncay Bayram (Karadeniz Technical Un., Trabzon, Türkiye)

11.20 – 11.35 **Dennis Bonatsos** (Inst. of Nuclear and Particle Phy., NCSR, Greece)
Shape coexistence and shape/phase transitions in even-even nuclei

11.35 – 11.50 **Ergash M. Tursunov** (INP-Academy of Sciences, Uzbekistan)
Detailed Study of the Astrophysical Capture Reaction $\alpha(d, \gamma)^{6}Li$ in a Three-Body Model

11.50 – 12.05 **Majid Gojayev** (Baku State University, Baku, Azerbaijan)
Production of the vector boson and two Higgs bosons in the electron-positron collisions

12.05 – 12.20 **Elif Kemah** (Sakarya Un., Sakarya, Türkiye)
Investigation of the Ground-State M1 moments in ^{229,231}Th Isotopes

12.30 – 13.30 LUNCH BREAK

Afternoon Session 13.30 – 15.00 Time Zone Istanbul (GMT+3)

Chair: Nihal Büyükçizmeci (Selçuk Un., Konya, Türkiye)

13.30 – 13.55 **Mannap Yu.Tashmetov** (INP-Academy of Sciences of the Republic of Uzbekistan)
The development and implementation of perspective technologies

13.55 – 14.20 **Esra Yüksel** (University of Surrey, Surrey, United Kingdom)
Constraining the nuclear symmetry energy using parity-violating electron scattering experiments

14.20 – 14.35 **Sema Küçüksucu** (University of Zagreb, Zagreb, Croatia)
Isotopic dependence of (n, α) reaction cross sections for Fe and Sn nuclei

14.35 – 14.50 **Büruce Öztürk** (Sakarya Un., Sakarya, Türkiye)
Magnetic Moment Inference and Modeling of $^{53\text{-}81}$Cu Nuclei with Anfis

14.50 – 15.05 **Nihal Büyükçizmeci** (Selçuk Un., Konya, Türkiye)
Rapidity distributions of nuclei and hypernuclei

15.10 – 15.30 COFFEE BREAK

Afternoon Session 15.30 – 17.00 Time Zone Istanbul (GMT+3)

Chair: Aybaba Hançerlioğulları (Kastamonu Un., Kastamonu, Türkiye)

15.30 – 15.45 **Mohammad Reza Hadizadeh** (Central State University, Ohio, USA)
Investigating Few-Body Systems in 2D Materials: Adapting Faddeev Method from Nuclear Physics

15.45 – 16.00 **Aybaba Hançerlioğulları** (Kastamonu Un., Kastamonu, Türkiye)
Utilization Of Some Boron Containing Minerals as Fast Neutron Shielding in Nuclear Power Plants

16.00 – 16.15 **Rezvan Rezaeizadeh** (University of Guilan, Rasht, İran)
Solutions of Klein-Gordon equation with Woods-Saxon potential through PQR method

---

May 10, 2023 Wednesday

Morning Session 09.30 – 10.50 Time Zone Istanbul (GMT+3)

Chair: Nihal Büyükçizmeci (Selçuk Un., Konya, Türkiye)

09.30 – 09.55 **Valentine O. Nesterenko** (JINR, Dubna, Russia)
Anomalous behavior of nuclear moment of inertia

09.55 – 10.20 **Izyan Hashim** (Universiti Teknologi Malaysia, Malaysia)
Ordinary Muon Capture Delayed Gamma Ray Analysis for double beta decays (DBDs) and anti-neutrino nuclear responses

10.20 – 10.35 **Mehmet Dağ** (Karabük Un., Karabük, Türkiye)
Gamow-Teller Transition Logft Value for Pd-114 Isotope

10.35 – 10.50 **Huseynqulu Quliyev** (National Aviation Academy of Azerbaijan, Azerbaijan)
Distribution of dipole excitation up to 10 MeV: The case of ^{124}Xe nucleus

10.50 – 11.20 COFFEE BREAK

Morning Session 11.20 – 12.30 Time Zone Istanbul (GMT+3)

Chair: Savaş Ağduk (Karabük Un., Karabük, Türkiye)

11.20 – 11.45 **İlkay Türk Çakır** (Institute of Technology Accelerator, Ankara Un., Türkiye)
Future Circular Collider (FCC) Project

11.45 – 12.00 **Sultan Şahin Bal** (Bitlis Eren Un., Bitlis, Türkiye)
The Determination of ^{238}U, ^{232}Th and ^{40}K Radioactivity Concentrations of Some Healing and Spa Water in Bitlis

12.00 – 12.15 **Sultan Şahin Bal** (Bitlis Eren Un., Bitlis, Türkiye)
The Determination of ^{222}Rn Gas Radioactivity Concentrations of Some Healing and Spa Water in Bitlis

12.15 – 12.30 **Khalid H. Mahdi Aal-Shabeeb** (Karabük Un., Karabük, Türkiye)
Comparing the concentration of radon in the old and new residential houses in Karabük city/Türkiye using the passive method

12.30 – 13.30 LUNCH BREAK
Afternoon Session 13.00 – 14.15 **Time Zone Istanbul (GMT+3)**
Chair: Mahmut Böyükata (Kırıkkale Un., Kırıkkale, Türkiye)

13.30 – 13.45 **Abdurahman Büber** (Kırıkkale Un., Kırıkkale, Türkiye)
Nuclear Structure of even-even $^{100\text{-}128}$Cd isotopes under the framework of IBM-1

13.45 – 14.00 **Najm Abdullah Saleh Saleh** (University of Duhok, Duhok, Iraq)
U1F Transition Logft Value for As-74 Isotope by pn-QRPA

14.00 – 14.15 **Esranur Yalçınkaya** (Sakarya Un., Sakarya, Türkiye)
Investigation of $I^{\pi}=1^{-}$ excited states properties in neutron-deficient ^{162}Yb nucleus

14.30 – 15.00 Closing Remarks

16th International Conference on Nuclear Structure Properties NSP 2023 8 – 10 May, 2023, Karabük University, Karabük, Türkiye					
TIME ZONE ISTANBUL (GMT+3)					
8 May 2023 Monday		9 May 2023 Tuesday		10 May 2023 Wednesday	
Chair: Necla Çakmak		Chair: Mahmut Böyükata		Chair: Nihal Büyükçizmeci	
09.15 - 09.30	Opening Remarks				
09.30 - 09.55	Take R. Saito	09.30 – 09.55	Jameel-Un Nabi	09.30 – 09.55	Valentine O. Nesterenko
09.55 - 10.20	Serkan Akkoyun	09.55 – 10.20	Manuela Cavallaro	09.55 – 10.20	Izyan Hashim
10.20 – 10.35	Mouna Bouhelal	10.20 – 10.35	Francesco Cappuzzello	10.20 – 10.35	Mehmet Dağ
10.35 – 10.50	Mouna Bouhelal	10.35 – 10.50	Frederic Lasiaille	10.35 – 10.50	Huseynqulu Quliyev
10.50 – 11.20 COFFEE BREAK					
Chair: Serkan Akkoyun		Chair: Tuncay Bayram		Chair: Aysuhan Ozansoy	
11.20 – 11.35	Abir Selim	11.20 – 11.35	Dennis Bonatsos	11.20 – 11.45	İlkay Türk Çakır
11.35 – 11.50	Abir Selim	11.35 – 11.50	Ergash M. Tursunov	11.45 – 12.00	Sultan Şahin Bal
11.50 – 12.05	Ayşe Çömü	11.50 – 12.05	Emilya Omarova	12.00 – 12.15	Sultan Şahin Bal
12.05 – 12.20	Gamze Ekici	12.05 – 12.20	Elif Kemah	12.15 – 12.30	Khalid H. Mahdi Aal-Shabeeb
12.30 – 13.30 LUNCH BREAK					
Chair: Nihal Büyükçizmeci		Chair: Nihal Büyükçizmeci		Chair: Mahmut Böyükata	
13.30 – 13.55	Fabrice Pelestor	13.30 – 13.55	Mannap Yu.Tashmetov	13.30 – 13.45	Abdurahman Büber
13.55 – 14.20	Khusniddin K. Olimov	13.55 – 14.20	Esra Yüksel	13.45 – 14.00	Najm Abdullah Saleh Saleh
14.20 – 14.35	Khusniddin K. Olimov	14.20 – 14.35	Sema Küçüksucu	14.00 – 14.15	Esranur Yalçınkaya
14.35 – 14.50	Fatima Benrachi	14.35 – 14.50	Büruce Öztürk	14.15 – 14.30	Closing Remarks
14.50 – 15.05	Nadjet Laouet	14.50 – 15.05	Nihal Büyükçizmeci		
15.10 – 15.30 COFFEE BREAK					
Chair: Savaş Ağduk		Chair: Aybaba Hançerlioğulları			
15.30 – 15.45	Robert Poenaru	15.30 – 15.45	Mohammad Reza Hadizadeh		
15.45 – 16.00	Christopher Oluwatobi	15.45 – 16.00	Aybaba Hançerlioğulları		
16.00 – 16.15	Gamze Hoşgör	16.00 – 16.15	Rezvan Rezaeizadeh		
16.15 – 16.30	Gamze Hoşgör				
16.30 – 16.45	Esra Evcin Baydilli				

FULL-TEXTS

Shape coexistence and shape/phase transitions in even-even nuclei

Dennis Bonatsos[1*], Andriana Martinou[1], S. K. Peroulis[1], T. J. Mertzimekis[2], and N. Minkov[3]

[1]Institute of Nuclear and Particle Physics, National Centre for Scientific Research "Demokritos", GR-15310 Aghia Paraskevi, Attiki, Greece
[2]Department of Physics, National and Kapodistrian University of Athens, Zografou Campus, GR-15784 Athens, Greece
[3]Institute of Nuclear Research and Nuclear Energy, Bulgarian Academy of Sciences, 72 Tzarigrad Road, 1784 Sofia, Bulgaria

* Corresponding author e-mail address: bonat@inp.demokritos.gr

ORCID Numbers: 0000-0003-1728-0910 (Dennis.Bonatsos), 0000-0003-3140-2136 (Andriana.Martinou), 0000-0002-2321-4242 (Spyridon.Peroulis), 0000-0001-9191-7903 (Theo.Mertzimekis), 0000-0002-4416-6497 (Nikolay.Minkov)

Abstract— The subtle relation between shape coexistence (SC) and shape/phase transitions in even-even nuclei is explored by looking at the systematics of the B(E2) transition rates between the first excited state of angular momentum zero, which is the bandhead of the intruder band, and the first excited state with angular momentum two, which belongs to the ground state band. It turns out that shape coexistence should be expected in nuclei lying within the stripes of nucleon numbers 7-8, 17-20, 34-40, 59-70, and 96-112 predicted by the dual shell mechanism of the proxy-SU(3) model, avoiding their junctions, within which high deformation is expected. Along major proton shell closures, one sees SC due to neutron-induced proton particle-hole excitations, while SC due to proton-induced neutron particle-hole excitations is related to a first-order shape/phase transition from spherical to deformed shapes and appears away from major shell closures.

Keywords— *shape coexistence, shape/phase transitions*

Introduction

Shape coexistence (SC) in an even-even nucleus refers to the situation in which the ground state band is lying close in energy with another K=0 band having a radically different structure, for example, one of them being spherical and the other one deformed. Several review articles exist, in which nuclei known to exhibit SC are reported, appearing to cluster into islands on the nuclear chart (see, for example, Fig. 8 of [1]). It is then of interest to find some practical rules, which could predict in which parts of the nuclear chart SC can be expected to appear, to guide the experimental effort.

Formalism

In the present work, we summarize some rules found by looking at the systematics of experimental data for energy levels and B(E2) transition rates among them. A detailed version of the present report will be published elsewhere [2]. In what follows we are going to use the energy ratios

$$R_{4/2} = E(4_1^+) / E(2_1^+), \quad R_{0/2} = E(0_2^+) / E(2_1^+), \quad R_{2/0} = 1 / R_{0/2}, \tag{1}$$

as well as the B(E2)s ratio

$$B_{02} = B(E2; 0_2^+ \rightarrow 2_1^+) / B(E2; 2_1^+ \rightarrow 0_1^+). \tag{2}$$

Results and Discussion

In Fig. 1(a) we have collected all nuclei for which the ratio B_{02} is known [3], plotted against $R_{0/2}$. We remark that all nuclei for which SC is known to occur appear on the left of the N=90 isotones ^{150}Nd, ^{152}Sm, and ^{154}Gd, which are known to be the textbook examples of the X(5) critical point symmetry between spherical and prolate deformed shapes [4], while nuclei not showing SC are lying on the right of the X(5) bump. Since X(5) is characterized by $R_{0/2} = 5.7$, Fig. 1(a) implies that SC can be expected in nuclei with $R_{0/2} < 5.7$ and $B_{02} > 0.1$. The behavior shown by the data in Fig. 1(a) is corroborated in Fig. 1(b) by the predictions of several theoretical models based on the Bohr Hamiltonian [5].

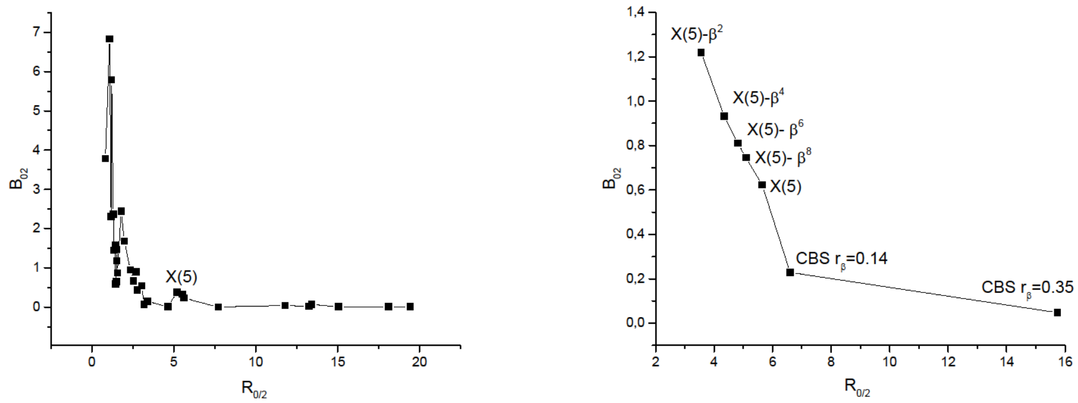

Fig. 1. Experimental (a) and theoretical (b) B_{02} ratios vs. $R_{0/2}$.

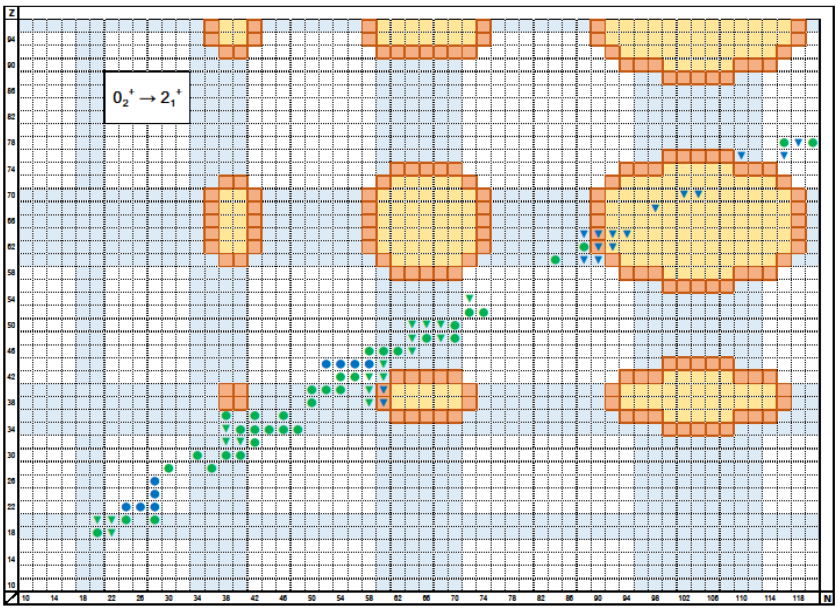

Fig. 2. Nuclei exhibiting SC (green symbols) and nuclei not showing SC (blue symbols) across the nuclear chart, on which the azure stripes of SC, predicted by the dual shell mechanism [6] within the proxy-SU(3) model [7] and the orange contours of P~5 [5] are also shown.

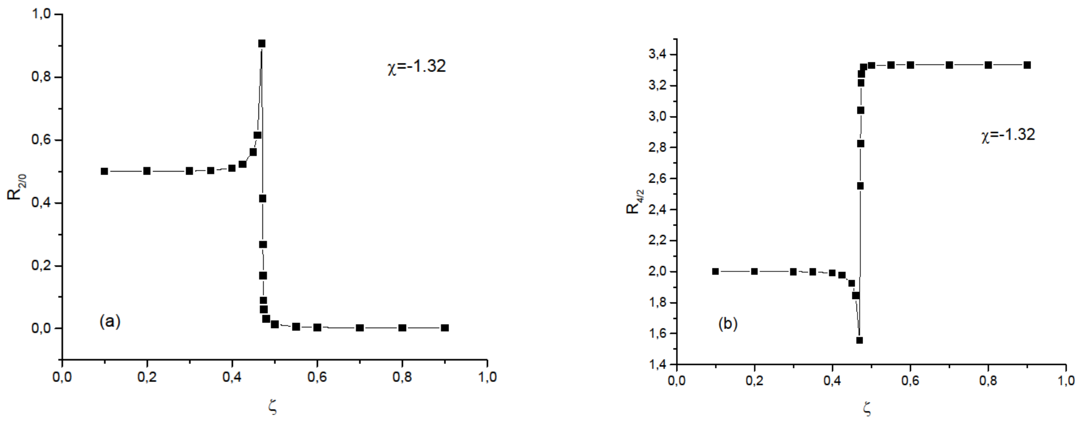

Fig. 3. Evolution of the $R_{2/0}$ and $R_{4/2}$ ratios across the critical point of the shape/phase transition from spherical to deformed shapes, as predicted by an IBM Hamiltonian [8.9] for 250 bosons.

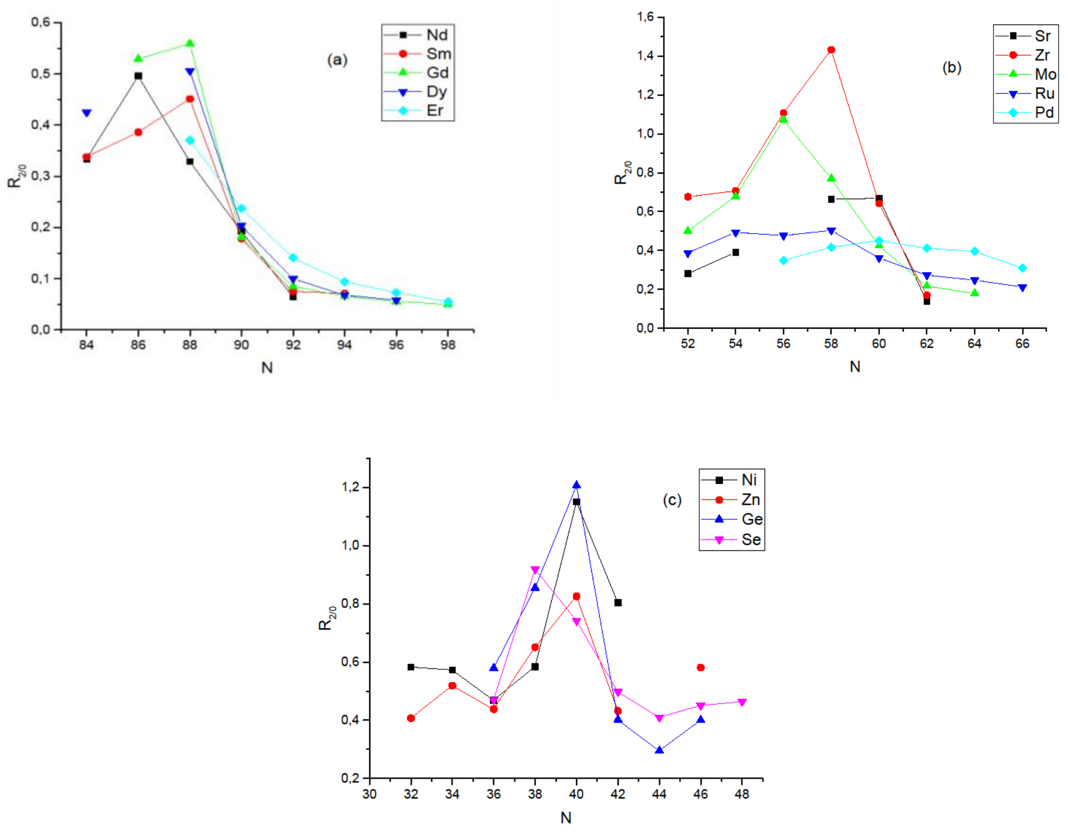

Fig. 4. Evolution of the experimental $R_{2/0}$ ratio across the critical point of the shape/phase transition from spherical to deformed shapes at N=90 (a), 60 (b), 40 (c).

The nuclei appearing in Fig. 1(a) are placed on the nuclear chart in Fig. 2, in which green symbols indicate nuclei exhibiting SC, while blue symbols stand for nuclei not showing SC. We see that the nuclei showing SC are falling within the azure stripes predicted by a dual shell mechanism [6] based on the proxy-SU(3) symmetry [7] as the places in which SC is possible to appear. Furthermore, in Fig. 2 the contours of P~5 are shown in orange, where the P-factor [5], P= NpNn / Np+Nn, with Np (Nn) being the valence protons (neutrons) measured from the nearest closed shell, is a measure of collectivity, corresponding to deformed nuclei for P>5. We observe that nuclei showing SC are lying outside the P~5 contours, while deformed nuclei lie inside. This provides us with a third rule to be obeyed by nuclei showing SC, P < 5, which turns out to be equivalent to $R_{4/2} < 3.05$.

The close relation between SC and shape/phase transitions in the N=90, 60, 40 regions can now be discussed. In Fig. 3 the results of IBM calculations using the IBAR code [8] for the standard IBM Hamiltonian in the consistent-Q formalism [9] are shown. We see that at the critical point, located at the value 0.4721 of the control parameter ζ, the $R_{4/2}$ ratio jumps from a spherical value close to 2 to a deformed value close to 3.33, while the $R_{2/0}$ ratio jumps from higher to lower values after exhibiting a sharp maximum at the critical point. Exactly the same behavior is exhibited by the experimental values of $R_{2/0}$ in the N=90, 60, 40 regions, as seen in Fig. 4, indicating that SC seen in these regions is closely related to the occurrence of a shape/phase transition from spherical to deformed shapes. In contrast, SC near Z=82, 50 is known to be interpreted in terms of particle-hole excitations across the proton major shells [1].

Acknowledgment – Support by the Bulgarian National Science Fund (BNSF) under Contract No. KP-06-N48/1 is gratefully acknowledged.

References

[1] K. Heyde and J.L. Wood, “Shape coexistence in atomic nuclei,” Rev. Mod. Phys. 83, 1467 (2011).
[2] D. Bonatsos, A. Martinou, S.K. Peroulis, T.J. Mertzimekis, and N. Minkov, “Signatures for shape coexistence and shape/phase transitions in even-even nuclei,”, J. Phys. G (2023) to be published.
[3] ENSDF database https://www.nndc.bnl.gov/ensdf
[4] P. Cejnar, J. Jolie, and R.F. Casten, “Quantum phase transitions in the shapes of atomic nuclei,” Rev. Mod. Phys. 82, 2155 (2010).
[5] R.F. Casten, “Quantum phase transitions and structural evolution in nuclei,” Prog. Part. Nucl. Phys. 62, 183 (2009).
[6] A. Martinou, D. Bonatsos, T.J. Mertzimekis, K.E. Karakatsanis, I.E. Assimakis, S.K. Peroulis, S. Sarantopoulou, and N. Minkov, “The islands of shape coexistence within the Elliott and the proxy-SU(3) models,” Eur. Phys. J. A 57, 84 (2021).
[7] D. Bonatsos, A. Martinou, S.K. Peroulis, T.J. Mertzimekis, and N. Minkov, “The proxy-SU(3) symmetry in atomic nuclei,” Symmetry 15, 169 (2023).
[8] R.J. Casperson, “IBAR: Interacting boson model calculations for large system sizes”, Comp. Phys. Commun. 183, 1029 (2012).
[9] D.D. Warner and R.F. Casten, “Revised formulation of the phenomenological Interacting Boson Approximation”, Phys. Rev. Lett. 48, 1385 (1985).

Correlations between parameters of the Tsallis distribution and Hagedorn function with transverse flow in proton-protons collisions at the LHC

Khusniddin K. Olimov [1,2,*], Igor A. Lebedev[3], Anastasiya I. Fedosimova[3,4], Fu-Hu Liu[5], Elena Dmitriyeva[2], Kobil A. Musaev[1], Kosim Olimov[1], Azizjon Tokhirov[1], Bekhzod S. Yuldashev[6]

[1]*Physical-Technical Institute of Uzbekistan Academy of Sciences, Chingiz Aytmatov str. 2[b], 100084 Tashkent, Uzbekistan*
[2]*National University of Science and Technology MISIS (NUST MISIS), Almalyk branch, Almalyk, Uzbekistan*
[3]*Institute of Physics and Technology, Satbayev University, Almaty, Kazakhstan*
[4]*Institute of Nuclear Physics, Almaty, Kazakhstan,*
[5]*Institute of Theoretical Physics & Collaborative Innovation Center of Extreme Optics & State Key Laboratory of Quantum Optics and Quantum Optics Devices, Shanxi University, Taiyuan 030006, China*
[6]*Institute of Nuclear Physics of Uzbekistan Academy of Sciences, Tashkent, Uzbekistan*

* Corresponding author e-mail address: khkolimov@gmail.com; kh.olimov@uzsci.net

ORCID Numbers: 0000-0002-1879-8458 (Khusniddin.Olimov), 0000-0002-7562-9925 (Igor.Lebedev), 0000-0001-9607-6074 (Anastasiya.Fedosimova), 0000-0002-2261-6899 (Fu-Hu.Liu)

Abstract— The correlations among parameters of the thermodynamically consistent Tsallis distribution and Hagedorn function with the embedded transverse flow, obtained from combined analysis of the experimental midrapidity transverse momentum spectra of the charged pions and kaons, protons and antiprotons as a function of the average charged-particle multiplicity density, $\langle dN_{ch}/d\eta \rangle$, measured by ALICE Collaboration at the LHC, have been analyzed in *p*+*p* collisions at $(s)^{1/2}$ = 7 and 13 TeV. The strong anticorrelation between non-extensivity parameter *q* for the charged pions and effective temperature, *T*, of the Tsallis distribution has been observed in *p*+*p* collisions at $(s)^{1/2}$=7 and 13 TeV. The parameter *q* for the protons and antiprotons has been strongly positively correlated with *T* in both *p*+*p* collisions at $(s)^{1/2}$=7 and 13 TeV. Relatively strong positive correlation between parameter *q* (*n*) for the charged pions and *q* (*n*) for the charged kaons has been found in both *p*+*p* collisions at $(s)^{1/2}$=7 and 13 TeV. This could be due to similarity of mechanisms of production of pions and kaons, having a similar quark structure, in high-energy proton-proton collisions. The strong anticorrelation between parameter *q* for the charged pions and *q* for the protons and antiprotons has been obtained in both *p*+*p* collisions at $(s)^{1/2}$=7 and 13 TeV. The obtained significant differences in the characters of parameter correlations for protons and antiprotons, on the one hand, and pions and kaons, on the other hand, are probably due to the significant differences in the quark structure and mechanisms of production of baryons and mesons in proton-proton collisions at high energies. The substantially differing behavior of the *q* (*n*) versus $\langle dN_{ch}/d\eta \rangle$ dependencies in regions $\langle dN_{ch}/d\eta \rangle < 6-7$ and $\langle dN_{ch}/d\eta \rangle > 6-7$ has been obtained for all studied particle types in both *p*+*p* collisions at $(s)^{1/2}$ = 7 and 13 TeV. The totally opposite correlations between parameter *n* (*q*) for pions and kaons and $\langle dN_{ch}/d\eta \rangle$ observed in regions $\langle dN_{ch}/d\eta \rangle < 6$ ($\langle dN_{ch}/d\eta \rangle < 7$) and $\langle dN_{ch}/d\eta \rangle > 6$ ($\langle dN_{ch}/d\eta \rangle > 7$) support the findings of our recent works [*Universe* 8, 174 (2022), *Int. J. Mod. Phys. A* 36, 2150149 (2021)] about a possible onset of deconfinement phase transition at $\langle dN_{ch}/d\eta \rangle \approx 6.1 \pm 0.3$ ($\langle dN_{ch}/d\eta \rangle \approx 7.1 \pm 0.2$) in proton-proton collisions at $(s)^{1/2}$=7 TeV ($(s)^{1/2}$=13 TeV).

Keywords— *proton-proton collisions at the LHC; transverse momentum distributions of hadrons; Tsallis distribution; effective temperature; non-extensivity parameter q; QCD-inspired Hagedorn function; Hagedorn function with embedded transverse flow; transverse flow; kinetic freeze-out temperature; exponent parameter n; onset of deconfinement phase transition; Quark-gluon plasma (QGP)*

Introduction

High-energy heavy-ion collisions at the Large Hadron Collider (LHC, CERN, Switzerland) and Relativistic Heavy-ion Collider (RHIC) at Brookhaven National Laboratory (USA) were used to produce the plasma of nearly free quarks and gluons, called Quark-gluon plasma (QGP). This hot and dense QGP matter, with extremely short life time of the order of 10^{-23} s, was deduced to behave almost as a perfect fluid with very low viscosity [1-4]. The produced QGP decays very rapidly into many hadrons via the process called hadronization. Then, the still hot and dense system of produced hadrons expands and cools down, going very swiftly through the chemical and kinetic freeze-out stages. At the chemical freeze-out, the hadrons stop interacting inelastically and the abundancies of different particle species get fixed. The temperature of the system at the chemical freeze-out, $T_{\rm ch}$, and the corresponding chemical potential, μ, are extracted from analysis of the ratios of yields of various particle species using the thermal or statistical hadronization models [5-8]. At the final kinetic freeze-out, the particles of a fireball stop interacting elastically and their kinematical properties, such as their (transverse) momenta and energies, get "frozen", not changing any more, followed by a free-stream of the final particles towards detectors. Therefore, the measured transverse momentum, p_t, distributions of the final particle species are analyzed to extract the thermodynamic and hydrodynamic properties of a system at the moment of kinetic freeze-out. The present work [9] is an extension of our recent papers [10] and [11], which were devoted to investigation of evolution of the collective properties of p+p collisions at $(s)^{1/2}$ = 7 and 13 TeV with a change in the average charged-particle multiplicity density, $\langle dN_{ch}/d\eta\rangle$, through combined minimum χ^2 fits of the midrapidity p_t distributions of the charged pions and kaons, protons and antiprotons, measured by ALICE Collaboration [12, 13], using the thermodynamically consistent Tsallis distribution and Hagedorn function with embedded transverse flow. In Refs. [10] and [11], the $\langle dN_{ch}/d\eta\rangle$ dependencies of the extracted parameters of the Tsallis distribution and Hagedorn function with the embedded transverse flow have been analyzed and interesting results on possible onset of deconfinement phase transition in p+p collisions at $(s)^{1/2}$ = 7 and 13 TeV obtained. The $\langle dN_{ch}/d\eta\rangle$ values for possible onset of deconfinement phase transition and corresponding energy densities have been estimated and the dependence of the effective temperature, T, on $\langle dN_{ch}/d\eta\rangle$ established in these collisions [10, 11]. However, the correlations among extracted parameters of the Tsallis distribution as well as Hagedorn function with embedded transverse flow have not been studied in these works [10, 11]. Such correlation analysis is extremely important to establish relationships between different parameters, including those, which characterize the collective properties of a system produced in high-energy proton-proton collisions. In the present work [9], we investigate the correlations among parameters of the Tsallis distribution as well as Hagedorn function with embedded transverse flow, extracted recently in p+p collisions at $(s)^{1/2}$ = 7 and 13 TeV in Refs. [10] and [11].

Analysis and Results

To study the correlation between two sets of parameters x and y, we calculate the Pearson correlation coefficient as follows:

$$r_{xy} = \frac{\sum_{i=1}^{n}(x_i - \langle x \rangle)\cdot(y_i - \langle y \rangle)}{\sqrt{\sum_{i=1}^{n}(x_i - \langle x \rangle)^2 \cdot \sum_{i=1}^{n}(y_i - \langle y \rangle)^2}} , \qquad (1)$$

where $\langle x \rangle = \frac{\sum_{i=1}^{n} x_i}{n}$ and $\langle y \rangle = \frac{\sum_{i=1}^{n} y_i}{n}$ are the mean values of the parameters x and y. The Pearson correlation coefficient, r_{xy}, being a statistical measure of a linear correlation between two sets of data, varies from −1 to +1. The values $r_{xy} = \pm 1$ imply that the relationship between x and y is perfectly described by a linear equation, and all data points (x_i, y_i) are lying on a line in XY plane. The value $r_{xy} = 0$ denotes an absence of a linear correlation between x and y. The positive and negative values of r_{xy} mean the positive and negative (linear) correlation, respectively, between x and y. To estimate the uncertainty in the obtained r_{xy} values, we calculate the standard error of Pearson correlation coefficient as

$$s_r = \sqrt{\frac{1 - r_{xy}^2}{n-2}} . \qquad (2)$$

The formula in Eq. (2) is obtained from an assumption that the data are normally distributed and with the null hypothesis that there is a zero correlation between x and y.

As an example, Fig. 1 displays the dependencies of non-extensivity parameter, q, for the charged pions and kaons, protons and antiprotons on effective temperature parameter, T, of Tsallis function in p+p collisions at $(s)^{1/2}$=7 and 13 TeV. As seen from orientations and shapes of 1-sigma confidence ellipses (correspond to 68% confidence level) and r_{xy} values in Figs. 1(a) and 1(b), the parameter q for the charged pions is strongly anticorrelated with parameter T with r_{xy} being close to −0.9 in both p+p collisions at $(s)^{1/2}$=7 and 13 TeV. This result is consistent with a strong negative correlation found in Ref. [14] between temperature, T, and (q−1) for negative pions in p+p, d+Au, and Au+Au collisions at $(s_{nn})^{1/2}$=200 GeV at the RHIC. Quite strong negative correlation between Tsallis function parameters T and q for the charged pions in Au+Au collisions at the RHIC and Pb+Pb collisions at the LHC at wide energy range $(s_{nn})^{1/2}$=62−5020 GeV was obtained in Ref. [15]. Figures 1(c) and 1(d) show quite weak correlation between parameter q for kaons and temperature parameter, T, in case of p+p collisions at $(s)^{1/2}$=7 TeV and almost no correlation with $r_{xy} \approx 0$ in case of p+p collisions at $(s)^{1/2}$=13 TeV. It follows from Figs. 1(e) and 1(f) that the character of a correlation between q for protons and antiprotons and T is totally opposite to that between the parameter q for the charged pions and T in Figs. 1(a) and 1(b). As observed from Figs. 1(e) and 1(f), the parameter q for protons and antiprotons is strongly positively correlated with parameter T with $r_{xy} \approx +1$ in both p+p collisions at $(s)^{1/2}$=7 and 13 TeV.

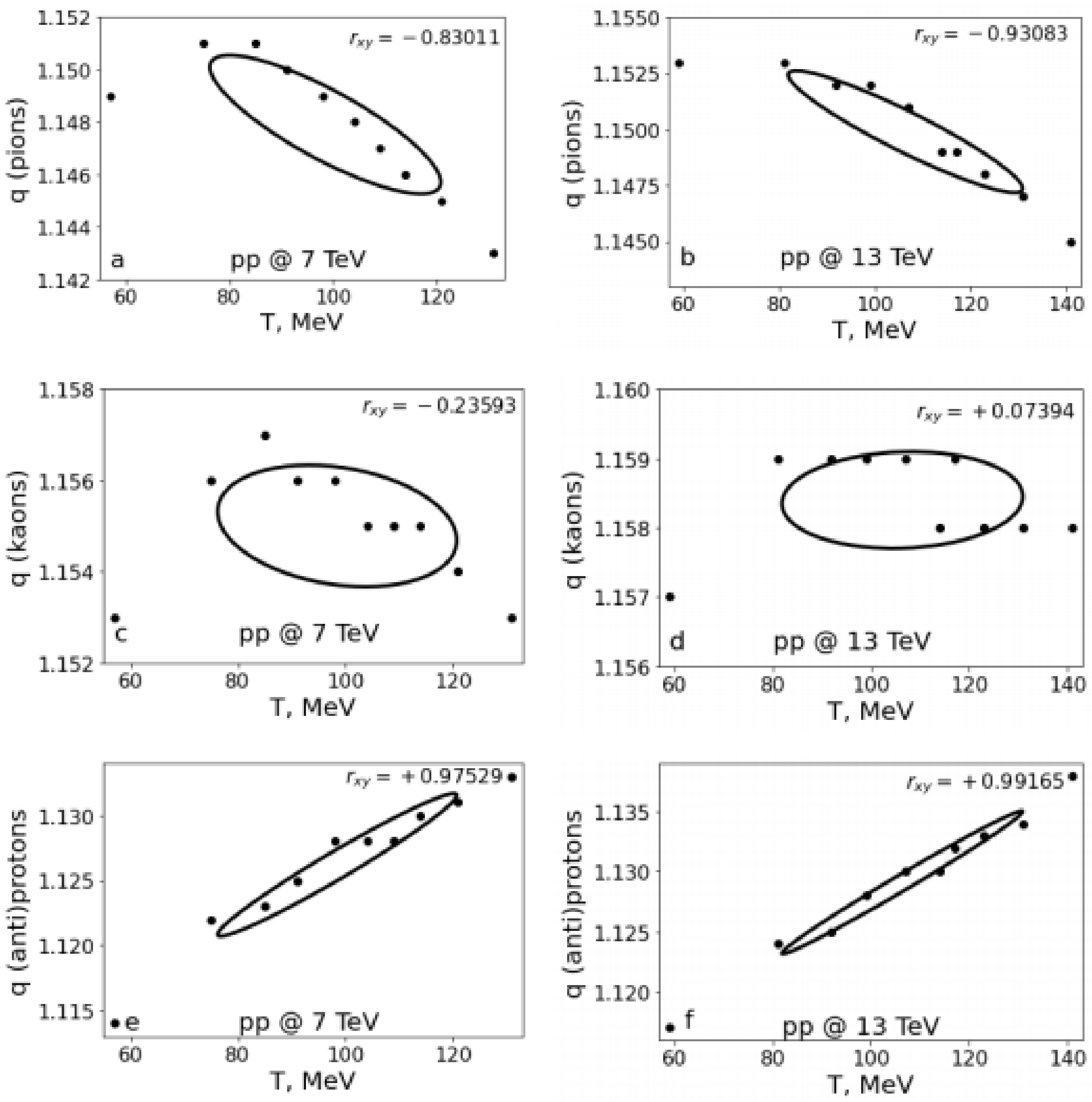

Fig. 1. The dependencies (●) of non-extensivity parameter, q, for the charged pions (a and b) and kaons (c and d), protons and antiprotons (e and f) on the effective temperature parameter T of the Tsallis distribution function in p+p collisions at $(s)^{1/2}$=7 and 13 TeV. The corresponding 1-sigma confidence ellipses are plotted. The corresponding Pearson correlation coefficients, r_{xy}, along with the standard errors are: −0.83±0.20 (a); −0.93±0.13 (b); −0.24±0.34 (c); +0.07±0.35 (d); +0.98±0.08 (e); +0.99±0.05 (f)

Summary and Conclusions

We analyzed [9] the correlations among parameters of the thermodynamically consistent Tsallis distribution and Hagedorn function with embedded transverse flow, obtained from combined analysis of the experimental midrapidity ($|y|$<0.5) transverse momentum spectra of the charged pions and kaons, protons and antiprotons at ten groups of $\langle dN_{ch}/d\eta\rangle$ in inelastic p+p collisions at $(s)^{1/2}$ = 7 and 13 TeV, measured by ALICE Collaboration at the LHC. The correlations were studied by calculating the Pearson coefficient of a linear correlation, r_{xy}, between given two parameters and plotting the corresponding 1-sigma confidence ellipse, which covers a 68% confidence level. We observed strong anticorrelation between the non-extensivity parameter, q, for the charged pions and effective temperature, T, of the Tsallis distribution with the corresponding Pearson correlation coefficient, r_{xy}, being close to −0.9 in both p+p collisions at $(s)^{1/2}$=7 and 13 TeV. The correlation between parameter q for the charged kaons and T proved to be weak both in p+p collisions at $(s)^{1/2}$=7 and 13 TeV. In case of p+p collisions at $(s)^{1/2}$= 13 TeV the correlation was almost absent ($r_{xy} \approx 0$), being weaker than that in p+p collisions at $(s)^{1/2}$=7 TeV. In contrast with the strong anticorrelation between parameters q and T for pions, the q for protons and antiprotons proved to be strongly positively correlated with T with $r_{xy} \approx +1$ in both p+p collisions at $(s)^{1/2}$=7 and 13 TeV. A significant positive correlation between the q for the charged pions and q for the charged kaons was obtained in both p+p collisions at $(s)^{1/2}$=7 and 13 TeV. The positive correlation was significantly larger in p+p collisions at $(s)^{1/2}$=7 TeV compared to that at $(s)^{1/2}$=13 TeV. The q for the charged pions was strongly anticorrelated with q for the protons and antiprotons in both collisions. The significantly different behavior of the q (n) versus $\langle dN_{ch}/d\eta\rangle$ dependencies in regions $\langle dN_{ch}/d\eta\rangle < 6$−7 and $\langle dN_{ch}/d\eta\rangle > 6$−7 was obtained for all studied particle species in both p+p collisions at $(s)^{1/2}$=7 and 13 TeV. The strong positive correlation between q for the charged pions and kaons and $\langle dN_{ch}/d\eta\rangle$ was obtained in region $\langle dN_{ch}/d\eta\rangle < 6$. In contrast with this, the q of these two particle species and $\langle dN_{ch}/d\eta\rangle$ was strongly anticorrelated with $r_{xy} \approx -1$ in region $\langle dN_{ch}/d\eta\rangle > 6$ in p+p collisions at $(s)^{1/2}$=7 TeV. The observed totally opposite correlations between q (pions and kaons) and $\langle dN_{ch}/d\eta\rangle$ in regions $\langle dN_{ch}/d\eta\rangle < 6$ and $\langle dN_{ch}/d\eta\rangle > 6$ are consistent with the finding of Ref. [34] suggesting the possible onset of deconfinement phase transition at $\langle dN_{ch}/d\eta\rangle \approx 6.1\pm0.3$. Contrary to the behavior of q versus $\langle dN_{ch}/d\eta\rangle$ dependencies of pions and kaons, the non-extensivity parameter q for protons and antiprotons demonstrated a strong positive correlation with $\langle dN_{ch}/d\eta\rangle$ with r_{xy} being close to +1 in both $\langle dN_{ch}/d\eta\rangle < 6$ and $\langle dN_{ch}/d\eta\rangle > 6$ regions in p+p collisions at $(s)^{1/2}$=7 TeV.

The correlation between exponent parameter n (for the charged pions and kaons) and $\langle dN_{ch}/d\eta\rangle$ was significantly negative in region $\langle dN_{ch}/d\eta\rangle < 6$ ($\langle dN_{ch}/d\eta\rangle < 7$) and strongly positive in region $\langle dN_{ch}/d\eta\rangle > 6$ ($\langle dN_{ch}/d\eta\rangle > 7$) in p+p collisions at $(s)^{1/2}$=7 TeV ($(s)^{1/2}$=13 TeV). The observed opposite correlations between n (for pions and kaons) and $\langle dN_{ch}/d\eta\rangle$ in regions $\langle dN_{ch}/d\eta\rangle < 6$ ($\langle dN_{ch}/d\eta\rangle < 7$) and $\langle dN_{ch}/d\eta\rangle > 6$ ($\langle dN_{ch}/d\eta\rangle > 7$) are consistent with and support the finding of Ref. [34] (Ref. [35]) suggesting the possible onset of deconfinement phase transition at $\langle dN_{ch}/d\eta\rangle \approx 6.1\pm0.3$ ($\langle dN_{ch}/d\eta\rangle \approx 7.1\pm0.2$) in p+p collisions at $(s)^{1/2}$=7 TeV ($(s)^{1/2}$=13 TeV). In contrast with the behavior of n versus $\langle dN_{ch}/d\eta\rangle$ dependencies for pions and kaons, the exponent parameter n for protons and antiprotons was strongly anticorrelated with $\langle dN_{ch}/d\eta\rangle$ in both $\langle dN_{ch}/d\eta\rangle < 6$ ($\langle dN_{ch}/d\eta\rangle < 7$) and $\langle dN_{ch}/d\eta\rangle > 6$ ($\langle dN_{ch}/d\eta\rangle > 7$) regions in p+p collisions at $(s)^{1/2}$=7 TeV ($(s)^{1/2}$=13 TeV).

Completely opposite correlations between q (n) (for pions and kaons) and $\langle dN_{ch}/d\eta\rangle$ observed in two regions of $\langle dN_{ch}/d\eta\rangle$, preceding and following the estimated $\langle dN_{ch}/d\eta\rangle$ for a possible deconfinement phase transition, could possibly indicate a significant change in mechanisms of hadron production taking place at a probable crossover phase transition from a gas of hadrons to QGP state in both p+p collisions at $(s)^{1/2}$=7 and 13 TeV. Quite strong positive correlation between exponent parameter n for the charged pions and n for the charged kaons was obtained in both p+p collisions at $(s)^{1/2}$=7 and 13 TeV. This result proved to be consistent with the significant positive correlation observed between parameter q for the charged pions and q for the charged kaons. This could be due to similarity of mechanisms of production of pions and kaons, which have a similar structure consisting of one quark and one antiquark, in high-energy collisions. The substantial differences in the characters of parameter correlations observed for protons and antiprotons, on the one hand, and pions and kaons, on the other hand, could be due to significant differences in the quark structure and corresponding mechanisms of production of baryons and mesons in high-energy collisions.

Acknowledgment **–** The work of the coauthors from Kazakhstan, Uzbekistan, and China was supported by the Science Committee of the Ministry of Education and Science of the Republic of Kazakhstan (Grant No. AP14869032), Agency of Innovative Development of the Ministry of Higher Education, Science and Innovation of Uzbekistan (Grant № F3-20200929146), and by the National Natural Science Foundation of China (Grant № 11575103) and the Shanxi Provincial Natural Science Foundation (Grant № 201901D111043), respectively.

References

[1] H. Song *et al.*, 200 A GeV Au+Au Collisions Serve a Nearly Perfect Quark-Gluon Liquid, Phys. Rev. Lett. **106,** 192301 (2011).
[2] P. Huovinen and P. Ruuskanen, Hydrodynamic Models for Heavy-ion Collisions, Ann. Rev. Nucl. Part. Sci. **56**, 163 (2006).
[3] B. Muller and J. L. Nagle, Results from the Relativistic Heavy-ion Collider, Ann. Rev. Nucl. Part. Sci. **56**, 93 (2006).
[4] Braun-Munzinger, P.; Koch, V.; Schäfer, T.; and Stachel, J. Properties of hot and dense matter from relativistic heavy-ion collisions. Phys. Rept. **2016**, 621, 76. arXiv:1510.00442 [nucl-th].
[5] ALICE Collab. (B. Abelev *et al.*), Centrality dependence of π, K, and p production in Pb-Pb collisions at $(s_{nn})^{1/2}$=2.76 TeV, Phys. Rev. C **88,** 044910 (2013), arXiv: 1303.0737 [hep-ex].
[6] A. Adronic *et al.*, The thermal model on the verge of the ultimate test: particle production in Pb–Pb collisions at the LHC, J. Phys. G **38**, 124081 (2011).
[7] A. Adronic, P. Braun-Munzinger, and J. Stachel, Thermal hadron production in relativistic nuclear collisions: The hadron mass spectrum, the horn, and the QCD phase transition, Phys. Lett. B **673**, 142 (2009).
[8] J. Cleymans and K. Redlich, Unified Description of Freeze-Out Parameters in Relativistic Heavy-ion Collisions, Phys. Rev. Lett. **81**, 5284 (1998).
[9] Khusniddin K. Olimov *et al.*, Correlations among parameters of the Tsallis distribution and Hagedorn function with embedded transverse flow in proton-protons collisions at $(s)^{1/2}$ = 7 and 13 TeV, Eur. Phys. Journ. Plus **138**, 414 (2023). https://doi.org/10.1140/epjp/s13360-023-04037-7
[10] Khusniddin K. Olimov, Fu-Hu Liu, Kobil Musaev, Maratbek Shodmonov, Multiplicity Dependencies of Midrapidity Transverse Momentum Distributions of Identified Charged Particles in Proton-Proton Collisions at $(s)^{1/2}$ = 7 TeV at the LHC, Universe **8**, 174 **(2022)**. https://doi.org/10.3390/universe8030174

[11] Kh.K. Olimov *et al.*, Multiplicity dependencies of midrapidity transverse momentum spectra of identified charged particles in $p+p$ collisions at $(s)^{1/2}$=13 TeV at LHC, Int. J. Mod. Phys. A **36**, 2150149 (2021). https://doi.org/10.1142/S0217751X21501499

[12] ALICE Collab. (S. Acharya *et al*.), Multiplicity dependence of light flavor hadron production in *pp* collisions at $(s_{nn})^{1/2}$=7 TeV, Phys. Rev. C **99** (2), 024906 (2019), arXiv: 1807.11321v2 [nucl-ex].

[13] ALICE Collab. (S. Acharya *et al.*), Multiplicity dependence of π, K, and p production in *pp* collisions at $(s)^{1/2}$=13 TeV, Eur. Phys. J. C **80**, 693 (2020), arXiv: 2003.02394v1 [nucl-ex].

[14] G. Wilk and Z. Wlodarczyk, Power-laws in elementary and heavy-ion collisions. A story of fluctuations and nonextensivity? Eur. Phys. J. A **40**, 299 (2009).

[15] R. N. Patra, B. Mohanty, T. K. Nayak, Centrality, transverse momentum and collision energy dependence of the Tsallis parameters in relativistic heavy-ion collisions, Eur. Phys. J. Plus **136**, 702 (2021). https://doi.org/10.1140/epjp/s13360-021-01660-0

Dependencies of the average transverse momenta of the charged particles on particle species, centrality and collision energy in Au+Au collisions from the BES program at the RHIC

Khusniddin K. Olimov[1,2,*], Igor A. Lebedev[3], Anastasiya I. Fedosimova[3,4], Fu-Hu Liu[5], Boburbek J. Tukhtaev[1], Azizjon Tokhirov[1], Shokhida A. Khudoyberdieva[1]

[1]*Physical-Technical Institute of Uzbekistan Academy of Sciences, Chingiz Aytmatov str. 2[b], 100084 Tashkent, Uzbekistan*
[2]*National University of Science and Technology MISIS (NUST MISIS), Almalyk branch, Almalyk, Uzbekistan*
[3]*Institute of Physics and Technology, Satbayev University, Almaty, Kazakhstan*
[4]*Institute of Nuclear Physics, Almaty, Kazakhstan,*
[5]*Institute of Theoretical Physics & Collaborative Innovation Center of Extreme Optics & State Key Laboratory of Quantum Optics and Quantum Optics Devices, Shanxi University, Taiyuan 030006, China*

* Corresponding author e-mail address: khkolimov@gmail.com; kh.olimov@uzsci.net

ORCID Numbers: 0000-0002-1879-8458 (Khusniddin.Olimov), 0000-0002-7562-9925 (Igor.Lebedev), 0000-0001-9607-6074 (Anastasiya.Fedosimova), 0000-0002-2261-6899 (Fu-Hu.Liu)

***Abstract*—** The experimental spectra of the average transverse momentum, $<p_t>$, versus the average number of participant nucleons, $<N_{part}>$, dependencies of the identified charged particles at midrapidity in Au+Au collisions from the Beam Energy Scan (BES) program at the RHIC in $(s_{nn})^{1/2}$= 7-39 GeV energy range have been described very well with the proposed simple power model function. The degree of flattening of $<p_t>$ of the charged pions and kaons, protons and antiprotons in the analyzed heavy-ion collisions in $(s_{nn})^{1/2}$=7-39 GeV energy range have been investigated analyzing the dependencies of the obtained exponent parameter *alpha* of the simple power function on the particle species and collision energy $(s_{nn})^{1/2}$. On the whole, the exponent parameter *alpha* for the charged kaons, protons and antiprotons decreases noticeably with increasing collision energy of Au+Au collisions from $(s_{nn})^{1/2}$= 7 to 39 GeV. While for the charged pions the power parameter *alpha* decreases weakly in range $(s_{nn})^{1/2}$=7-20 GeV and practically does not change in region $(s_{nn})^{1/2}$=20-39 GeV. The significant gap between parameter *alpha* for the protons and antiprotons has been observed in region $(s_{nn})^{1/2}$=7-20 GeV. The normalization fitting constant *C* and power parameter *alpha* of the simple power function have been strongly anticorrelated for all studied particle species. The differences observed between parameter *alpha* versus collision energy dependencies of the particles and antiparticles have been related to the ratios of antiparticle and particle yields and differences in the mechanisms of production of particles and antiparticles. The observed dependencies of the evolution of the parameter *alpha* with changing Au+Au collision energy for the particles and antiparticles could reflect the interplay between associated particle production, which is dominant at the low energy range of BES at the RHIC, and pair production mechanism, which becomes dominant at the high energy range of BES. It is deduced that the parameter *alpha* can

be sensitive to the particle production mechanism(s) and its significant change could be related to the change in mechanisms of particle production or/and phase transitions in a nuclear/hadronic matter.

Keywords — *Heavy-ion collisions at the RHIC; average transverse momenta of particles; flattening of the average p_t; mechanisms of particle production; onset of deconfinement phase transition; mixed phase of QGP and hadrons*

Introduction

In the present work, we study the particle species and collision energy dependencies of an important variable – the average transverse momentum ($<p_t>$) of identified charged particles in Au+Au collisions from the BES program at the RHIC in $(s_{nn})^{1/2}$=7-39 GeV energy range. This variable was first proposed by Van Hove [1] to identify the deconfinement phase transition in high-energy proton-antiproton collisions with an anomalous behavior – a plateau-like structure of the average transverse momentum as a function of multiplicity of hadrons. Van Hove suggested [1] that the observed flattening of dependence of the experimental average transverse momentum at midrapidity versus the particle multiplicity per unit rapidity should indicate the deconfinement phase transition (the growth of entropy density at constant temperature) in a system with high energy density. Initially, Van Hove's idea was suggested to investigate the correlations between $<p_t>$ and hadron multiplicity in high-energy proton-antiproton collisions [1,2]. Nowadays we can analyze such correlations in high-statistics heavy-ion collisions at the RHIC and LHC energies [3-7]. In Ref. [6] the experimental spectra of $<p_t>$ versus the average pseudorapidity multiplicity density, average number of binary collisions ($<N_{coll}>$), and the average number of participant nucleons ($<N_{part}>$) dependencies of the identified charged particles at midrapidity in Au+Au and Pb+Pb collisions at RHIC and LHC in $(s_{nn})^{1/2}$= 62-5020 GeV energy interval were reproduced very well with the proposed simple power model function. The degree of flattening of $< p_t >$ of the charged pions and kaons, protons and antiprotons in heavy-ion collisions at RHIC and LHC in $(s_{nn})^{1/2}$=62-5020 GeV energy range were investigated from analysis of the dependencies of the extracted exponent parameter α of the simple power function on the particle species and collision energy $(s_{nn})^{1/2}$. The coincidence of the parameter α for pions and kaons in Pb+Pb collisions at $(s_{nn})^{1/2}$=5.02 TeV, reflecting practically identical shapes of $< p_t >$ versus the average pseudorapidity multiplicity density, $< N_{coll} >$, and $< N_{part} >$ spectra for pions and kaons in these collisions, was obtained. This result was interpreted as being due to the creation of the highly thermalized QGP, where the difference between u, d, and s flavors almost disappears, which results in the similar mechanisms of production of pions and kaons in Pb+Pb collisions at $(s_{nn})^{1/2}$=5.02 TeV. In present work we have performed the minimum $\chi 2$ fits of the experimental dependencies [7] of the average transverse momentum ($< p_t >$) on $< N_{part} >$ of the charged pions, charged pions, and protons+antiprotons, produced at midrapidity ($|y| < 0.1$) in Au+Au collisions at $(s_{nn})^{1/2}$=7.7, 11.5, 19.6, 27, and 39 GeV, with the proposed simple power model function:

$$< p_t >= C \cdot < N_{part} >^{\alpha}, \qquad (1)$$

where α is the exponent parameter, C is the fitting constant, and $<N_{\mathrm{part}}>$ is the average number of participant nucleons.

Analysis and Results

The minimum χ2 fit curves along with the experimental $< p_t >$ versus $< N_{part} >$ dependencies, obtained [7] by STAR Collaboration at midrapidity in Au+Au collisions from BES program, are shown in Fig. 1. As seen from Fig. 1, the simple power function in Eq. (1) reproduces very well all the studied experimental $< p_t >$ versus $< N_{part} >$ dependencies.

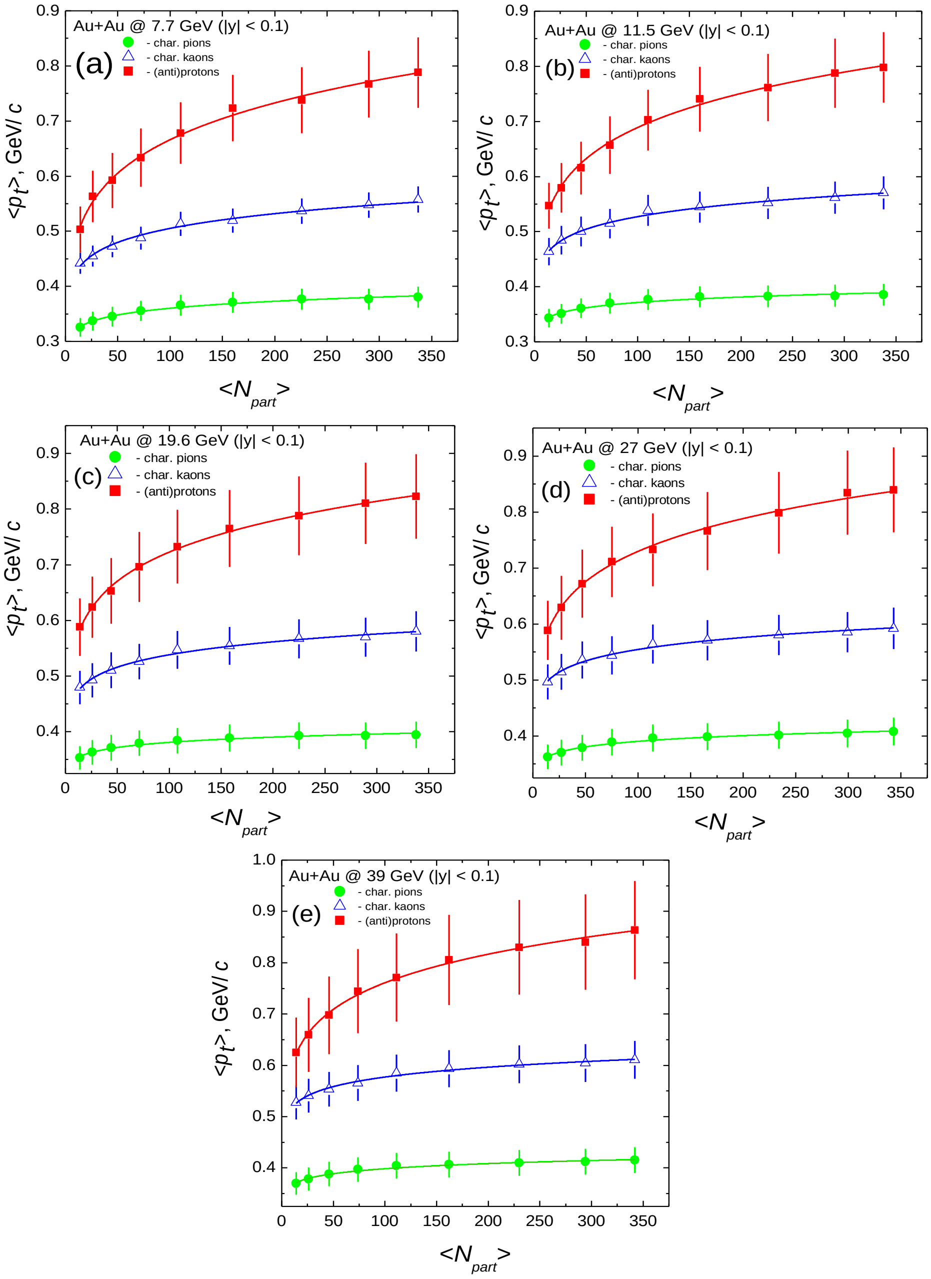

Fig. 1. Minimum χ2 fits (solid curves) with the simple power model function (Eq. (1)) of the experimental average transverse momentum, $< p_t >$, versus $< N_{part} >$ dependencies for the

charged pions, charged kaons, protons+antiprotons produced at midrapidity ($|y| < 0.1$) in Au+Au collisions at $(s_{nn})^{1/2}$=7.7 (a), 11.5 (b), 19.6 (c), 27 (d), and 39 (e) GeV. The vertical errors are combined systematic and statistical errors (added in quadrature). The combined errors are dominated by the systematic uncertainties.

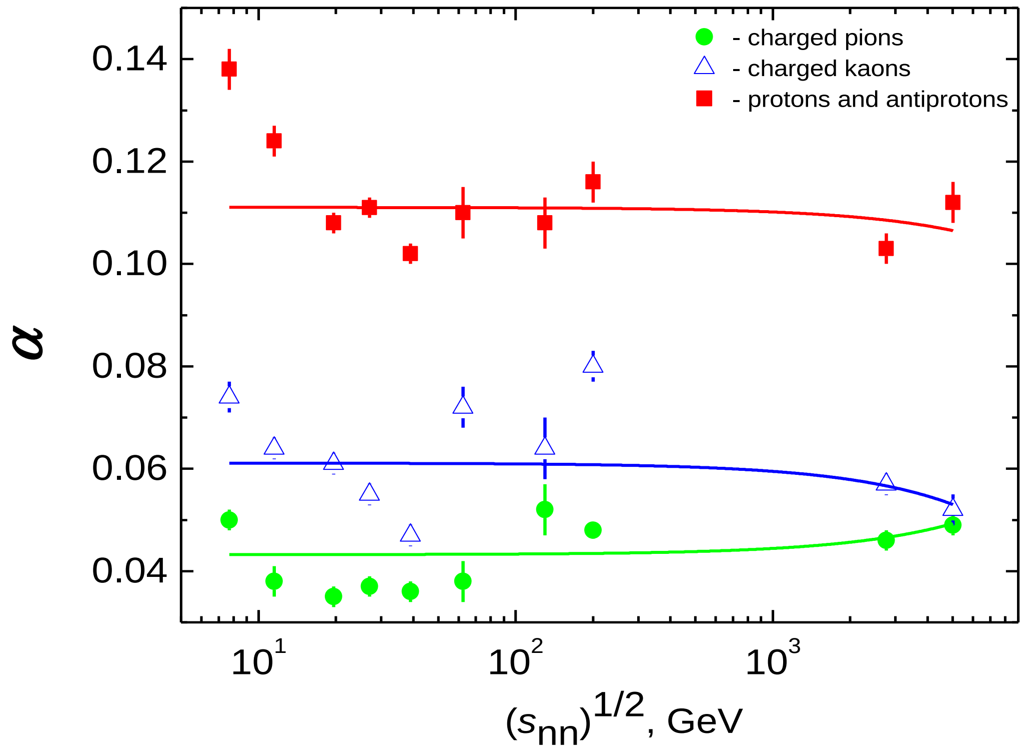

Fig. 2. The dependence on collision energy $(s_{nn})^{1/2}$ of the exponent parameter α for the charged pions, charged kaons, protons+antiprotons, extracted in present work from minimum $\chi 2$ fits by $< p_t >= C \cdot < N_{part} >^{\alpha}$ (Eq. (1)) function of the experimental midrapidity $< p_t >$ versus $< N_{part} >$ dependencies of the charged pions and kaons, protons+antiprotons in Au+Au collisions in $(s_{nn})^{1/2}$=7−39 GeV energy range. The corresponding results, obtained in Ref. [6] from analysis of the experimental $< p_t >$ data of STAR Collaboration for midrapidity Au+Au collisions at $(s_{nn})^{1/2}$=62.4, 130 and 200 GeV, and those of ALICE collaboration for midrapidity Pb+Pb collisions at $(s_{nn})^{1/2}$=2.76 and 5.02 TeV, are presented for a comparison. For guiding the eyes, the spectra are fitted (solid curves) by a linear function $y = Ax + B$. The straight lines appear as the solid curves because of the logarithmic scale on the horizontal x axis.

Figure 2 shows the collision energy, $(s_{nn})^{1/2}$, dependencies of the power parameter α for the charged pions, charged kaons, protons+antiprotons produced at midrapidity in Au+Au collisions at BES energies, extracted in present work. The corresponding results, obtained in Ref. [6] from analysis of the experimental $< p_t >$ data of STAR Collaboration for midrapidity Au+Au collisions at $(s_{nn})^{1/2}$=62.4, 130 and 200 GeV, and those of ALICE collaboration for midrapidity Pb+Pb collisions at $(s_{nn})^{1/2}$=2.76 and 5.02 TeV, are also presented in Fig. 2 for a comparison. As observed from Fig. 2, we have α(pion) < α(kaon) < α((anti)proton) inequality in the whole BES energy range. A similar hadron mass dependence for the parameter α of the simple power function was obtained in Ref. [6] from analysis of the experimental $< p_t >$ data of STAR Collaboration for midrapidity Au+Au collisions at $(s_{nn})^{1/2}$=62.4, 130 and 200 GeV, and those of ALICE collaboration for midrapidity Pb+Pb collisions at $(s_{nn})^{1/2}$=2.76 and 5.02 TeV. Since the degree of flattening of the spectrum rises as exponent α approaches zero, the largest degree of flattening is observed for the pion spectra − hadrons with the lowest mass, and the lowest degree of flattening is obtained for (anti)protons – hadrons with the largest mass among the studied particles. As observed from Fig. 2, the α values (and corresponding degree of flattening) of kaon spectra are located in between those for pions and (anti)protons at the BES energy range. As stated in Ref. [6], the power parameter α should contain the combined information for both the degree of thermalization and particle production mechanism(s). Then we can understand that the pions, hadrons with the lowest production threshold energy, should have the largest degree of thermalization and thermalize at the significantly smaller system temperature (smaller energy density) compared to kaons and (anti)protons, which are characterized by the significantly larger production threshold energies. This can be seen from the observed higher degree of flattening, reflected by the smaller α values, of the charged pion spectra in Fig. 1 compared to those for the charged kaons and (anti)protons.

Figure 2 shows the clear dependencies of the exponent α on collision energy, $(s_{nn})^{1/2}$, for the charged pions, charged kaons, and (anti)protons in Au+Au collisions at BES energy range, $(s_{nn})^{1/2}$ = 7−39 GeV. Generally, the power parameter α for the charged kaons, and (anti)protons shows a noticeable decreasing behavior with increasing collision energy from $(s_{nn})^{1/2}$= 7 to 39 GeV. For the charged pions, as observed from Fig. 2, the exponent parameter α decreases quite weakly in range $(s_{nn})^{1/2}$=7-19 GeV and then remains constant within uncertainties in region $(s_{nn})^{1/2}$ = 19-39 GeV, and further up to 62 GeV. It is necessary to mention that in Ref. [7] STAR Collaboration obtained a linear increase in pion yields as a function of collision energy, $(s_{nn})^{1/2}$, in range up to around 19.6 GeV with a subsequent kink structure seen at about 19.6 GeV. It was interpreted [7] as a substantial change in particle production mechanism in Au+Au collisions at $(s_{nn})^{1/2} \approx$ 19.6 GeV. The energy dependence of pion yields has changed a slope: the slope below 19.6 GeV is significantly different from that above 19.6 GeV [7]. It agrees with the significant change of the $(s_{nn})^{1/2}$ dependence of the power parameter α for the charged pions obtained at $(s_{nn})^{1/2} \approx$ 19.6 GeV in Fig. 2 in presenthe t work.

Even though the exponent α demonstrates generally a decrease with an increase in $(s_{nn})^{1/2}$ energy for both charged kaons and (anti) protons in $(s_{nn})^{1/2}$ = 7−39 GeV energy range, the small kinks are observed in regions 19−27 GeV and 11−19 GeV in Fig. 2 for (anti)protons and the charged kaons, respectively. Figure 2 demonstrates that the power parameter α for (anti)protons does not change within uncertainties in the wide energy range $(s_{nn})^{1/2}$ = 62−5020 GeV. In present work we observe that parameter α for the charged kaons increases substantially in region $(s_{nn})^{1/2}$ = 39−62 GeV after an overall decrease in range $(s_{nn})^{1/2}$ = 7−39 GeV, which can also reflect a significant change in production mechanism(s) of the charged kaons in Au+Au collisions at $(s_{nn})^{1/2} \approx$ 39−50 GeV. We observe the anticorrelated behavior of the parameter α

for the charged pions and charged kaons in regions $(s_{nn})^{1/2} \approx 62-130$ GeV and $(s_{nn})^{1/2} \approx 62-130$ GeV: in these two regions an increase of the parameter α for one particle species goes along with a decrease of the α for the second particle species, and vice versa.

Figure 2 shows that with an increase in $(s_{nn})^{1/2}$ in region $(s_{nn})^{1/2} > 200$ GeV, the exponent α for charged kaons approaches that for charged pions, with the parameter α for kaons coinciding with that for pions at the largest collision energy $(s_{nn})^{1/2}$=5.02 TeV. The coincidence of the power parameter α for pions and kaons, produced at midrapidity in Pb+Pb collisions at $(s_{nn})^{1/2}$=5.02 TeV, reflecting practically identical shapes of $< p_t >$ versus $< N_{part} >$, $< \frac{dN_{ch}}{d\eta} >$, and $< N_{coll} >$ spectra for pions and kaons, was obtained in Ref [6]. This result was interpreted [6] as being due to production of the highly thermalized QGP, in which the difference among u, d, and s flavors practically disappears, which leads to the similar mechanisms of production of pions and kaons in Pb+Pb collisions at $(s_{nn})^{1/2}$=5.02 TeV at the Large Hadron Collider.

Acknowledgment – The work of the coauthors from Kazakhstan, Uzbekistan, and China has been supported by the Science Committee of the Ministry of Education and Science of the Republic of Kazakhstan (Grant No. AP14869032), Agency of Innovative Development of the Ministry of Higher Education, Science and Innovation of Uzbekistan (Grant № F3-20200929146), and by the National Natural Science Foundation of China (Grant № 11575103) and the Shanxi Provincial Natural Science Foundation (Grant № 201901D111043), respectively.

References

[1] L. Van Hove, *Phys. Lett. B* **118,** 138 (1982).
[2] M.I. Gorenstein *et al.*, *Phys. Lett. B* **567,** 175 (2003).
[3] STAR Collab. (B. I. Abelev *et al.*), *Phys. Rev. C* **79,** 034909 (2009).
[4] ALICE Collab. (B. Abelev *et al.*), *Phys. Rev. C* **88,** 044910 (2013), arXiv: 1303.0737v3 [hep-ex].
[5] ALICE Collab. (S. Acharya *et al.*), *Phys. Rev. C* **101,** 044907 (2020), arXiv: 1910.07678v2 [nucl-ex].
[6] Khusniddin K. Olimov, Fu-Hu Liu, Kobil A. Musaev, Alisher K. Olimov, Boburbek J. Tukhtaev, Nasir Sh. Saidkhanov, Bekhzod S. Yuldashev, Kosim Olimov and Kadyr G. Gulamov, "Particle species and collision energy dependencies of the midrapidity average transverse momenta of identified charged particles in Au + Au and Pb + Pb collisions in $(s_{nn})^{1/2}$ = 62-5020 GeV energy range", International Journal of Modern Physics E, 30, 04, 2150029 (2021). https://www.worldscientific.com/doi/abs/10.1142/S0218301321500294
[7] STAR Collaboration, L. Adamczyk *et al.*, Bulk Properties of the Medium Produced in Relativistic Heavy-Ion Collisions from the Beam Energy Scan Program, Phys. Rev. C **96**, 044904 (2017), arXiv:1701.07065 [nucl-ex].

Nuclear Structure of even-even $^{114\text{-}118}$Cd isotopes under the framework of IBM-1

Abdurahman Büber[1*], Mahmut Böyükata[2]

[1]Kırıkkale University, Graduate School of Natural and Applied Sciences, Physics Department, Kırıkkale, Türkiye
[2] Kırıkkale University, Faculty of Arts and Sciences, Physics Department, Kırıkkale, Türkiye

* Corresponding author e-mail address: abdurahman.buber@gmail.com

ORCID Numbers: 0000-0002-8222-0204 (Abdurahman Büber), 0000-0002-8065-9993 (Mahmut Böyükata)

Abstract — In this proceeding, some nuclear structural properties of even-even $^{144\text{-}118}$Cd isotopes were studied by using the Interacting Boson Model-1 (IBM-1). First, the parameters of the model Hamiltonian were fitted to experimental data by analyzing the energy ratios along the isotopic chain. Later, the energy levels and B(E2) values were calculated, and the results are in good agreement with the experimental data. Moreover, the $\mathbf{R_L}$ ratio of $\mathbf{E(L^+)}$ to $\mathbf{E(2_1^+)}$ were studied of low-lying collective states in comparison to the experimental data.

Keywords — *Cd isotopes, energy levels, B(E2) values, IBM-1 mode*

Introduction

Recently, even even Cd isotopes were actively studied as given in Refs. [2-6]. Energy levels, B(E2) values, and two-neutron separation energies of even-even $^{106\text{–}122}$Cd isotopes were studied along U(5)-SO(6) transitional region within the SU(1,1)-based Hamiltonian of the IBM model [2]. The large-scale shell-model calculations were performed to investigate the yrast states of the even-even $^{98\text{–}108}$Cd isotopes [3]. Deformations and energy spectra of the even-even $^{108\text{–}116}$Cd isotopes were investigated by using the self-consistent mean-field approach and IBM-2 model [4]. The quadrupole deformations and shape transition in even-even $^{96\text{–}136}$Cd isotopes were studied by using covariant density functional theory [5]. Some of the structural properties of even-even $^{110\text{-}116}$Cd isotopes were investigated within the IBM-2 model along SU(5) - SU(3) transition [6]. In this work, the calculations of the Interacting Boson Model-1 (IBM-1) [1] is performed for the energy levels and B(E2) values along the Z=48 isotopic chain. Obtained results for even-even $^{114\text{-}118}$Cd isotopes are presented in this proceeding. First, the Hamiltonian parameters o were fitted by analyzing the energy ratios in the ground state band. Then, the energy levels and B(E2) values were calculated within the IBM-1 model. Later, $\mathrm{R_L} = \mathrm{E(L^+)/E(2_1^+)}$ were studied as a function of angular momentum (L) for the low-lying levels in the ground state bands of given even-even Cd isotopes in comparison to the experimental data.

Interacting Boson Model-1

The IBM-1 model [1] is used to investigate the nuclear structural properties of even-even isotopes. This model is based on the interaction of s-boson (L=0) and d-boson (L=2) [7].

Because of the six components of these bosons, IBM-1 is described in terms of the U(6) unitary group and this group has three possible subgroups called the dynamical symmetries. These possible symmetries are labeled by U(5), SU(3) and O(6) for spherical, axially deformed and γ-unstable nuclei, respectively [7]. Another concept called as critical point symmetries introduced by labelled [8] and labelled by X(5) located in between U(5) - SU(3) symmetries and E(5) is in between U(5) - O(6).

For present study multipole form of IBM-1 Hamiltonian was used

$$H = \varepsilon\, \hat{n}_d + a_0 \hat{P}^{\dagger}\hat{P} + a_1 \hat{L}\cdot\hat{L} + a_2 \hat{Q}\cdot\hat{Q} + a_3 \hat{T}_3\cdot\hat{T}_3. \quad (1)$$

Here, ε'',a_0, a_1, a_2, a_3 are free parameters, and $\hat{n}_d$, $\hat{P}$, $\hat{L}$, $\hat{Q}$, $\hat{T}_3$ are d-boson, pairing, angular momentum, quadrupole, octupole operators.

$E2$ transition operator of IBM-1 is

$$\hat{T}^{(E2)} = \alpha_2[\hat{d}^{\dagger} \times \tilde{s} + \hat{s}^{\dagger} \times \hat{d}\,]^{(2)} + \beta_2\, [\hat{d}^{\dagger} \times \hat{d}\,]^{(2)} \quad (2)$$

where $\hat{d}$ and $\hat{s}$ are boson operator, $\alpha_2$and β_2 are free parameters.

B(E2) values is calculated by;

$$(E2;\, \mathrm{L_f} \rightarrow \mathrm{L_i}\ ) = \frac{1}{2\mathrm{L_i}+1}\left|\langle\langle \mathrm{L_f}\|\, \hat{\mathrm{T}}^{(E2)} \|\mathrm{L_i}\rangle\rangle\right|^2 \quad (3)$$

where L is angular momentum, $\mathrm{L_i}$ and $\mathrm{L_f}$ refer to the initial and final states, respectively [1]

Results

For the presented study, the parameters of the model Hamiltonian given in Eq. (1) were fitted to by analyzing the energy ratios given in left panel of Fig. 1. This figure includes experimental data [9] and calculated energy ratio ($R_{4/2}$) of even-even $^{114-118}$Cd isotopes. As seen this panel, given Cd isotopes are located between U(5) and O(6) transitional region. The ^{114}Cd is close to the E(5) critical point while ^{118}Cd isotope is near to γ-unstable case.

Table 1. Boson numbers and Hamilton parameters (in units of MeV) of the $^{114-118}$Cd isotopes.

Isotopes	N	ε	a_0	a_1	a_2	a_3
^{114}Cd	9	0.062	-	0.026	-	0.06
^{116}Cd	8	-	0.0713	0.0318	-	0.06
^{118}Cd	7	0.0094	-	0.024	-0.018	0.057

Fitted set of Hamiltonian parameters are listed in Table 1 including boson numbers. The boson number of each nucleus is the sum of the proton and neutron boson numbers given by N=N_π+N_ν. Here, N denotes the total number of bosons, N_π and N_ν are the number of the number of proton and neutron bosons. The PHINT and PBEM codes [10] of IBM-1 model were used to calculate the energy levels and B(E2) values of these isotopes. The energy levels of given Cd isotopes were calculated by using the set of parameters given in Table 1, and as seen in right side of Fig. 1, the calculations are in well agreement with the experimental data [9].

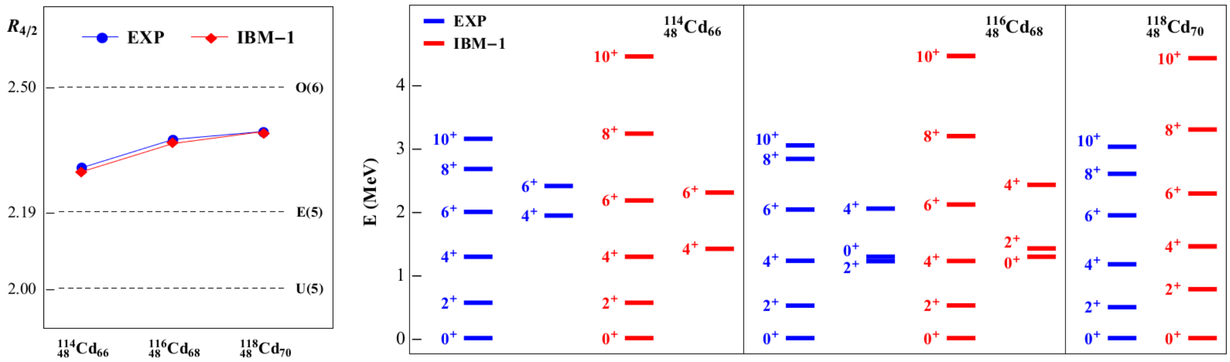

Fig. 1. The experimental and calculated energy ratios (left panel) and energy levels (right side) of given Cd isotopes.

Later, B(E2) values were calculated by fitting the constants of the reduced matrix elements given in Eq. (2). The experimental $B(E2: 2_1^+ \rightarrow 0_1^+)$ values of given isotopes were used to fit free parameters and as seen left side of Fig. 2, these values are almost same with experimental data. Right side of Fig. 2 includes $B(E2: 4_1^+ \rightarrow 2_1^+)$ values and the calculated B(E2) values of $^{114\text{-}116}$Cd isotopes are close to experimental data, this panel also includes prediction $B(E2: 4_1^+ \rightarrow 2_1^+)$ values of ^{118}Cd isotope.

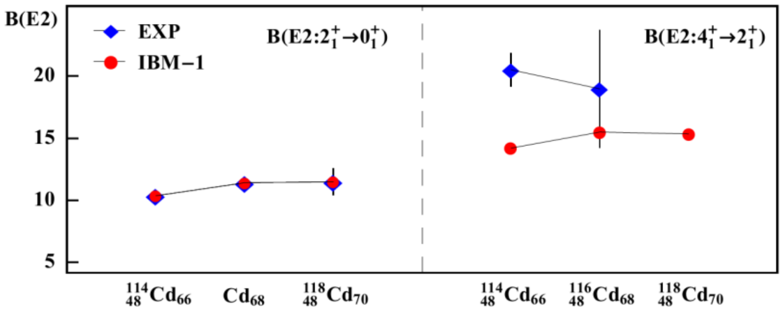

Fig. 2. The experimental (blue) and calculated (red) B(E2) values in unit e^2b^2 for $^{114\text{-}118}$Cd isotopes. $B(E2: 2_1^+ \rightarrow 0_1^+)$ is given in left panel and $B(E2: 4_1^+ \rightarrow 2_1^+)$ is in right panel.

The $R_L = E(L^+)/E(2_1^+)$ were investigated as a function of angular momentum (L) in the ground state bands of given even-even Cd isotopes. These ratios include the comparisons of the IBM-1 calculations with experimental data [9]. As seen Fig. 3, the calculations and the experimental data are mostly well agreement expecting the higher levels because the experimental 8^+ and 10^+ levels of the ground state bands are close to each other. The calculated R_L ratio increase towards higher levels.

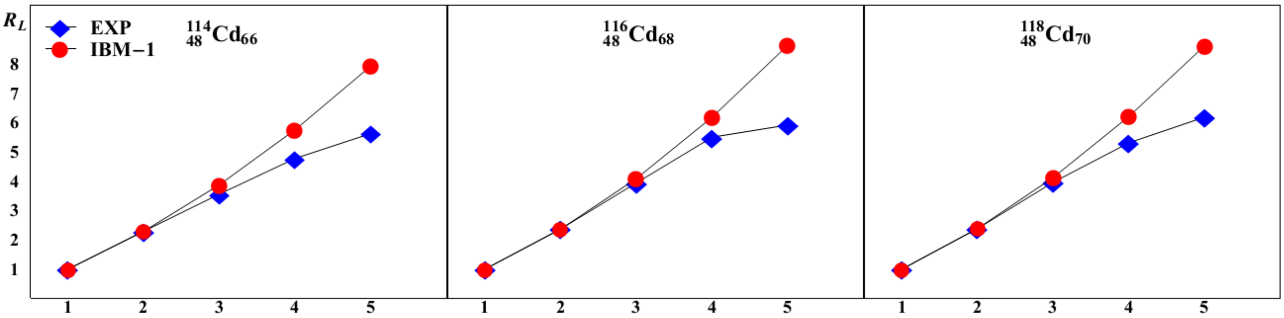

Fig. 3. Comparison of $R_L = E(L^+)/E(2_1^+)$ ratios as a function of angular momentum (L) in the ground state band for ^{114,116,118}Cd isotopes

Conclusion

In this work, the energy levels and the electromagnetic transition probabilities of $^{114\text{-}118}$Cd isotopes were investigated within the IBM-1 model. For the calculations of energy levels, the Hamiltonian parameters were fitted to experimental data of the energy ratio $R_{4/2}$ in the ground state bands for each Cd isotopes. The calculated energy levels and B(E2) values are well agreement with their experimental data [9]. According to the values of the energy ratio, the Cd isotopes are in between E(5) - O(6) symmetries of the U(5) - O(6) transitional region. The ^{114}Cd is close to the E(5) critical point symmetry and ^{118}Cd is close to O(6) case. The R_L ratio were investigated as a function of angular momentum (L) in the ground state bands of each Cd isotopes in the comparisons of calculations and experimental data [9]. According to these results, ^{114}Cd and ^{118}Cd isotopes exhibit similar behavior. In summary, in this proceeding, some nuclear structure properties of the selected even $^{114\text{-}118}$Cd isotopes were investigated and results are compared with experimental data. The more detail investigation of all even-even Cd isotopes along isotopic chain are in progress and will be presented in the forthcoming study.

References

[1] F. Iachello and A. Arima, "The Interacting Boson Model" Cambridge University Press, 1987.
[2] H. Sabri, "A theoretical study of energy spectra and two-neutron separation energies of $^{106–122}$Cd isotopes in the transitional region of IBM", Eur. Phys. J. Plus, 129, 138 (2014).
[3] A. Blazhev, K.Heyde, J.Jolie, and T. Schmidt, "A shell-model study of the light Cd isotopes", EPJ Web. Conf., 93, 01016. (2015)
[4] K. Nomura and J. Jolie, "Structure of even-even cadmium isotopes from the beyond-mean-field interacting boson model", Phys. Rev. C, 98, 024303 (2018).
[5] P. Kumar and S. K. Dhiman, "Microscopic study of shape evolution and ground state properties in even-even Cd isotopes using covariant density functional theory", Nucl. Phys. A, 1001, 121935 (2020).
[6] H. H. Sharqi and S. N. Abood, "Interacting boson model applied to the Cadmium isotopes", Eur. J. Phys. Sci., 5(2), 1 - 7 (2022).
[7] R. F.Casten and D. D. Warner, "The interacting boson approximation", Rev. Mod. Phys., 60, 389-469 (1988).
[8] F. Iachello, "Dynamic symmetries at the critical point. Phys. Rev. Lett., 85, 3580–3583 (2000).
[9] National Nuclear Data Center (NNDC), http://www.nndc.bnl.gov (2023).
[10] O. Scholten, "Computer codes PHINT and PBEM", KVI report. (unpublished).

Magnetic Moment Inference and Modeling of $^{53-81}$Cu Nuclei with Anfis

Büruce Öztürk[1*], Hakan Yakut[2] and Elif Kemah[2]

[1] *Sakarya University, Institute of Natural Sciences, Biomedical Engineering, Sakarya, Türkiye*
[2] *Sakarya University, Faculty of Science, Physics Department, Sakarya, Türkiye*

* Corresponding author's e-mail address: buruce.ozturk@ogr.sakarya.edu.tr

ORCID Numbers: 0000-0003-0358-2272 (Büruce1.Öztürk1), 0000-0002-3903-5863 (Hakan2 Yakut2), 0000-0001-9512-5524 (Elif3.Kemah3)

***Abstract*—** This study includes the investigation of the magnetic properties of odd-mass Cu nuclei, which are very popular in biomedical applications. With the Adaptive Neuro-Fuzzy Inference Systems (Anfis) inferences were made about the magnetic moments of the $^{53-81}$Cu isotopes with odd mass numbers. For this inference system, 600 nuclei were trained, and 200 nuclei were tested. Two successful processes encouraged inferences about odd-A Cu isotopes that do not have experimental magnetic moment values in the literature. The very small, calculated error rate supports the reliability of the inference result about ^{53,55,79,81}Cu isotopes without experimental magnetic moment data. These inference results were also supported by a theoretical method, the Quasiparticle-Phonon Nuclear Method (QPNM).

***Keywords*—** Anfis, Magnetic Moment, $^{53-81}$Cu, Artificial Intelligence, QPNM

Introduction

Magnetic dipole moment is an interesting topic for nuclear physicists as it gives a lot of information about the structure of the nuclei. Many nuclear models have been developed to theoretically explain magnetic moment values. However, the application of these models to nuclei is still unsatisfactory [1-2]. Artificial intelligence (AI) methods can be a good alternative to support the results in some cases where theoretical and experimental data are insufficient, as it is a fast, easy, and reliable method that can be used in mathematical calculations and modelling thanks to its learning, generalization, and inference capabilities.

Material and Methods

Anfis is a neural network system that works with fuzzy logic rules. Lutfi A. Zadeh [3] introduced fuzzy logic and fuzzy logic theory in 1965. In fuzzy sets, the belonging of an element to the set is defined by its membership degrees. Membership functions express these membership degrees. A fuzzy inference system is created with If-Then rules. Multiple input parameters relate to AND-OR processors [4]. Our fuzzy rules were created for the system with three input values and seven membership values for each input. The parameter set pi, qi, ri, and the result parameters form the rule bases and are integrated into the input value. Equation (1) gives the fuzzy rules created for the system.

$$\begin{aligned}
&Rule1 = \textbf{IF } A \text{ is } A_1 \textbf{ AND } Z \text{ is } B_1 \textbf{ AND } I \text{ is } C_1 \textbf{ THEN } f_1 = p_1A+q_1Z+r_1I \\
&Rule2 = \textbf{IF } A \text{ is } A_2 \textbf{ AND } Z \text{ is } B_2 \textbf{ AND } I \text{ is } C_2 \textbf{ THEN } f_2 = p_2A+q_2Z+r_2I \\
&\vdots \\
&Rule343 = \textbf{IF } A \text{ is } A_{343} \textbf{ AND } Z \text{ is } B_{343} \textbf{ AND } I \text{ is } C_{343} \textbf{ THEN } f_{343} = p_{343}A+q_{343}Z+r_{343}I
\end{aligned} \tag{1}$$

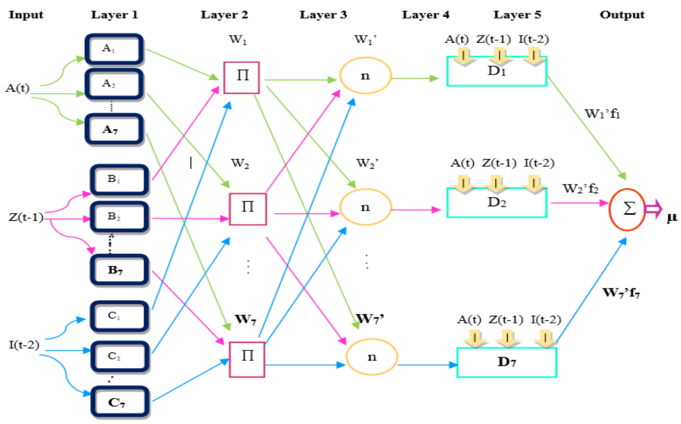

Fig.1. Adaptive Neuro-Fuzzy Inference System (ANFIS) With Three Inputs and One Output

A different process is performed on each layer. Layer 1 is where the input values are fuzzied with the membership function. The Gaussian function is given in Equation (2). The input parameters fuzzied by the Gaussian membership function are given by the Eqs. (3-5). In layer 3, each neuron calculates the normalized effect of a given rule, and Layer 4 is the layer where the input data fuzzied in layer 1 is defuzzied. Layer 5 contains a single node where the sum of all incoming signals and the final result is calculated. The mathematical formulas in each layer are adapted from Jang (1993) [4].

$$f(x;\sigma,c) = e^{\frac{-(x-c)^2}{2\sigma^2}} \tag{2}$$

$$Q_{1,i} = \mu_{Ai}(A(t)) = e^{\frac{1}{2}\left(\frac{A-c_i^A}{\sigma_i^A}\right)^2} \tag{3}$$

$$Q_{1,i} = \mu_{Bi-2}(Z(t-1)) = e^{\frac{1}{2}\left(\frac{Z-c_i^Z}{\sigma_i^Z}\right)^2} \tag{4}$$

$$Q_{1,i=}\mu_{ci-3}(I(t-2)) = e^{\frac{1}{2}\left(\frac{I-c_i^I}{\sigma_i^I}\right)^2} \tag{5}$$

Here, Q1, i represents the node i in Layer 1, the fuzzy sets A_i, B_{i-2}, and C_{i-3}, and the input A(t), Z(t-1), and I(t-3). I. signals at the node. Each node in layer 2 is computed by multiplying the effect of each fuzzy rule by the AND operation.

$$Q_{2,i} = W_i = \mu_{Ai}(A(t))\,\textbf{AND}\,\mu_{Bi-2}(Z(t-1))\,\textbf{AND}\,\mu_{Ci-3}(I(t-2)) \tag{6}$$

The error rates of the Anfis model were tested with R^2 and Root Mean Square Error (RMSE) values. These values are calculated as Ref [5].

Results and Discussions

In this study, MATLAB (MATLAB 2023a) program was used for data analysis. Input and output data are taken from references [6-7]. Mass number (A), proton number (Z), spin value (I), and magnetic moment (μ) data of nuclei with $1 \leq Z \leq 108$ protons were used. 80% of the data is reserved for the training process and 20% for the testing process. The training and test processes were successfully completed with an R^2 value of 0.98% and RMSE of 0.026489. The RMSE and R^2 values for the test were found to have a very small error value of 0.036 and 0.99%, respectively. After these two processes were completed, inferences were made about the magnetic moment values of $^{53-81}$Cu nuclei. Within this isotope series, there are no available experimental magnetic moment values for ^{53,55,79,81}Cu nuclei. Experimental values and the results of Anfis inference are given in Table 1. These values are supported by the Quasiparticle Phonon Nuclear Model (QPNM), which is a theoretical method, detailed descriptions of which are given in Ref. [8-23].

Table 1. Comparison of experimental values of $^{53-81}Cu_{29}$ isotopes with Anfis Inferences and QPNM Calculation

Nuclei	I^π	$\mu_{EXP.}$	μ_{Anfis}	μ_{QPNM}	Nuclei	I^π	$\mu_{EXP.}$	μ_{Anfis}	μ_{QPNM}
^{53}Cu	$3/2^-$	-	2.133	2.009	^{69}Cu	$3/2^-$	2.8383	2.83	2.1994
^{55}Cu	$3/2^-$	-	2.476	2.145	^{71}Cu	$3/2^-$	2.2747	2.27	2.0560
^{57}Cu	$3/2^-$	2.582	2.622	2.397	^{73}Cu	$3/2^-$	1.7426	2.001	2.0976
^{59}Cu	$3/2^-$	1.8910	2.21	2.2758	^{75}Cu	$5/2^-$	1.0062	1.688	2.0571
^{61}Cu	$3/2^-$	2.1083	2.177	2.666	^{77}Cu	$5/2^-$	1.61	1.61	2.016
^{63}Cu	$3/2^-$	2.2236	2.2236	2.2556	^{79}Cu	$5/2^-$	-	1.153	2.423
^{65}Cu	$3/2^-$	2.3817	2.38	2.2321	^{81}Cu	$5/2^-$	-	1.250	2.111
^{67}Cu	$3/2^-$	2.5142	2.51	2.2084					

As can be seen in Table 1, the microscopic QPNM results are in agreement with the predictions of Anfis. As can be seen here, the spin values of the nuclei have a great effect on the magnetic moment. However, it should be noted that the agreement between Anfis results and experimental data is much better and more satisfactory than the agreement between QPNM results and experimental data.

Conclusions

This work presents a previously unstudied argument in nuclear structure physics. For nuclei whose experimental magnetic moments have not yet been measured, inferences about the magnetic moments of Cu isotopes were made for the first time with an artificial intelligence-supported system (Anfis). The reliability of this system is compared with the calculations made with QPNM. It has been observed that the numerical values calculated by the Anfis are much closer to the experimental data than the QPNM method. It has also been observed that artificial intelligence-supported systems can be a good alternative to theoretical calculations. Theoretical studies on this subject are limited. The study showed that AI-based systems can overcome this problem and achieve accurate results close to experimental values, which can be a good reference point for future work in nuclear structure physics.

References

[1] J. Li, J. Meng, P. Ring, J. M. Yao and A. Arima, Prog. theory. Phys. 125 (2011) 1185

[2] J. Li, J. Meng, P. Ring, J. M. Yao and A. Arima, Sci. China Phys. Mech. Astron. 52 (2011) 204.

[3] L. A. Zadeh. Fuzzy sets. Information and Control, 8:338–353, 1965.

[4] J.-S. R. Jang, "ANFIS: adaptive-network-based fuzzy inference system," IEEE Trans. Syst. Man. Cybern., vol. 23, no. 3, pp. 665–685, 1993, DOI: 10.1109/21.256541.

[5]https://www.mathworks.com/help/matlab/ref/rmse.html?searchHighlight=rmse&s_tid=srchtitle_rmse_1, Date of Access=08.05.2023.

[6] Stone, N.J., Table of nuclear magnetic dipole and electric quadrupole moments. Atomic Data and Nuclear Data Tables, 90, 75-176, 2005.

[7] G. Audi, O.Bersillon, J. Blachot, A.H. Wapstra" The NUBASE evaluation of nuclear and decay properties ", Nuclear Physics A 729 (2003) 3–128.

[8] Yakut, H., Investigation of Electric and Magnetic Dipole Properties of Collective Dipole States in Rare-Earth Deformed Cores. Ph.D. Thesis, Sakarya University, Institute of Science and Technology, 2009.

[9] Yakut, H., Guliyev, E., Guner, M., Tabar, E., Zenginerler, Z., QPNM calculation for the ground state magnetic moments of odd-mass deformed nuclei: 157–167Er isotopes. Nuclear Physics A, 888, 23-33, 2012

[10] Yakut, H., Tabar, E., Kuliev, A.A., Zenginerler, Z., Kaplan, P., Ground state magnetic properties of odd neutron Dy isotopes. International Journal of Modern Physics E, 22, 1350076(1–13), 2013.

[11] Yakut, H., Tabar, E., Kuliev, A.A., Guliyev, E., The ground-state magnetic moments of odd-mass Hf isotopes. Central European Journal of Physics, 12, 843-850, 2014.

[12] Tabar, E., Investigation of the Scissor Mode Excitation of Odd-Mass Deformed Rare-Earth Nuclei. Ph.D. Thesis, Sakarya University Institute of Science and Technology, 2015.

[13] Tabar, E., Yakut, H., Kuliev, A.A., Microscopic description of ground state magnetic moment and low-lying magnetic dipole excitations in heavy odd mass 181Ta nucleus. International Journal of Modern Physics E, 25, 1650053, 2016.

[14] Tabar, E., Kuliev, A.A., Microscopic investigation of the low-lying magnetic dipole transitions in the odd-mass 155–169 Ho isotopes. Nuclear Physics A, 964, 1-17, 2017.

[15] Yakut H, Kuliev A, AGuliyev E," Investigations of the g_k -factors in the ^{175,177,179}Hf Isotopes", AIP Conference Proceedings 1072, 258 (2008)

[16] Yakut H, Kuliev A, A Guliyev E, Zenginerler Z," Intrinsic g(K) factors of odd-mass Lu167-179 isotopes", Pramana 73(5):829-83,2009

[17] Hoşgör G, Yakut H, Tabar E," Spin polarization effects on magnetic dipole moment of ^{153,155}Eu", AIP Conference Proceedings 1815, 060011 (2017)

[18] Tabar E, Yakut H, Kuliev A.A, Quliyev H, Hoşgör G," Magnetic moments and g-factors in odd-A Ho isotopes", *Chinese Phys. C* 41 074101,2017

[19] Yakut H, Tabar E, Hoşgör G,” Effects of the isoscalar and isovector interaction on the ground-state magnetic moments of odd-mass $^{137–145}$Ce nuclei”, Canadian Journal of Physics, Volume 97 • Number 11 1187 – 1190, (2019).
[20] Tabar E,” Magnetic properties of K = 1/2 states in deformed odd-mass nuclei” Nucl. Phys. A, 986 (2019), pp. 150-166.
[21] Tabar E,” A theoretical investigation of the magnetic dipole moment of the ground- and excited-states below 600keV in well-deformed ^{183,185}W, ^{185,187}Re and ^{187,189}Os”, International Journal of Modern Physics E Vol 28, No. 06, 2019
[22] Tabar E, “A theoretical study on the ground and low-energy magnetic dipole characteristics of ^{239}Pu nucleus” Nuclear Physics A Volume 987, Pp 202-221-2019.
[23] Tabar E, Kemah E, Yakut H, Hoşgör G,” First Theoretical Identification of the Magnetic Dipole Moment of the 97.43 keV State in 153Eu” Sakarya University Journal of Science,Volume 26, Issue 5, 967 - 973, 2022.

Creating an Online Calculation Tool for Fission Barrier Energy based on Machine Learning Methods

Serkan Akkoyun[1*], Cafer Mert Yeşilkanat[2] and Tuncay Bayram[3]

[1]*Department of Physics, Sivas Cumhuriyet University, Sivas, Türkiye*
[2]*Department of Mathematics and Science Education, Artvin Çoruh University, Artvin, Türkiye*
[3]*Department of Physics, Karadeniz Technical University, Trabzon, Türkiye*

* Corresponding author e-mail address: sakkoyun@cumhuriyet.edu.tr

ORCID Numbers: 0000-0002-8996-3385 (Serkan Akkoyun), 0000-0002-7508-7548 (Cafer Mert Yeşilkanat), 0000-0003-3704-0818 (Tuncay Bayram)

***Abstract*—** Fission barrier height is an important component for many reasons, including stellar nucleosynthesis, estimating the survival probabilities of the produced stable super-heavy nuclei, and calculating the competition between the fission process and neutron evaporation. It is not possible to observe directly, but it is estimated theoretically by using various methods. In this study, the fission barrier height estimation has been performed by artificial neural network method. Also, the results obtained in the calculations with different machine learning approaches were published as an online calculation module on an open access website. By entering basically proton, neutron, and mass numbers of the nuclei, it can be obtained fission barrier height information with the statistical error indicators of the machine learning methods.

***Keywords*—** *Fission barrier height, nuclear structure, machine learning*

Introduction

Accurate knowledge of fission barrier height is an important in nuclear physics studies such as stellar nucleosynthesis [1], estimating the survival probabilities of the produced stable super-heavy nuclei [2], and calculating the competition between the fission process and neutron evaporation [3]. Barrier height is not observed directly [4], although little experimental information is available [5]. However, by using various models it can be calculated theoretically. In this study, we used artificial neural network (ANN) method as an alternative approach to determine the fission barrier height information. It has been seen that increasing the number of hidden layers used in the ANN and the number of neurons in this layer improves the results. However, the structure in which the number of hidden layers is 3 and there are 18 neurons in each layer can make good enough predictions. Also, we published the estimations of the fission barrier heights from six different machine learning approaches (Cubist, XGBoost, Random Forest, Support Vector Regression, Multivariate Adaptive Regression Splines and ANN) in an open access web page. An online computation module has been developed that includes the results of fission barrier height estimation using these different machine learning approaches. Thus, in cases where experimental data is not available, the results of different machine learning approaches are calculated online by entering the proton and neutron numbers of the atomic nuclei whose fission barrier height value is desired. The results are provided to users along with statistical error indicators.

Materials and Methods

A. Cubist Model

Cubist is a rule-based machine learning model that is an extension of Quinlan's M5 model tree [6]. In this model, a tree is grown which includes linear regression models of the terminal leaves. Intermediate linear models are also present at each rung of the tree. A prediction is made at the terminal node of the tree using the linear regression model. But it is "smoothed" considering the prediction from the linear model at the previous node of the tree. The tree was originally reduced to a set of rules, which are paths from the top of the tree to the bottom. Rules are pruned out and/or combined for simplification.

B. Random Forest (RF)

The Random Forest (RF) algorithm based on many decision tree structures was first created by Brieman [7] as a combination of bagging and random subspace approaches. The training dataset is randomly divided into sub-data. The RF final estimate is determined by averaging all the results from each tree to produce an estimate. However, to increase forecast success, trees that fail the forecast result are pruned and their level of influence on the final forecast result is reduced. By increasing the weight coefficients of the trees that make the correct prediction, more contribution is made to the correct prediction.

C. Extreme Gradient Boosting (XGBoost)

Extreme gradient boosting (XGBoost) initially started as a research project by Tianqi Chen [8] as part of the Distributed (Deep) Machine Learning Community group. Notable features that make XGBoost different from other gradient boosting algorithms include intelligent punishment of trees, proportional shrinkage of leaf nodes, Newton upgrade, extra randomization parameter, application and non-core computing on single, distributed systems and automatic feature selection. XGBoost works as a Newton-Raphson in function space, unlike gradient boosting which works as a gradient descent in the function space, a quadratic Taylor approximation is used in the loss function to con-nect with the Newton Raphson method.

D. Support Vector Regression (SVR)

Support Vector Regression (SVR) is a supervised machine learning model with associated learning algorithms that analyse data for regression analysis and classification [9]. SVR is one of the popular a machine learning model that can be used in classification problems or class assignment where data cannot be separated linearly. A kernel is a function that places a low-dimensional plane into a higher-dimensional space where it can be broken up using a plane. That is, data that is not linearly separable is converted into separable data by adding more dimensions. There are three cores that SVM uses most. Linear kernel is dot product between two given observations, polynomial kernel allows curved lines in input space, radial basis function creates complex regions in feature space.

E. *Multivariate Adaptive Regression Splines (MARS)*

In statistics, multivariate adaptive regression splines (MARS) method is a form of regression analysis introduced by Jerome H. Friedman [10]. MARS is a non-parametric regression technique, and it can be seen as an extension of linear models. It does this by partitioning the data and run a linear regression model on each different partition. The methos automatically models nonlinearities and interactions between variables. MARS builds a model in two phases: the forward and the backward pass. This two-stage approach is the same as that used by recursive partitioning trees.

F. *Artificial Neural Network (ANN)*

Artificial neural network (ANN) mimics brain functionality [11]. Neurons, which are artificial nerve cells that perform operations, are connected to each other by synaptic weights, forming the ANN. In feedforward ANNs, the data flow is forward. The data is processed with the weight values of the connections a transmitted to the neurons in the next layer. All data entering a neuron is combined with an appropriate function. Then, the net data obtained inside the neuron is activated by an appropriate function. The main purpose of the method is to determine the final weight values for each connection between neurons based on random values. ANN, which has the best weights, can give outputs close to the desired values.

Results and Discussions

In the study performed with ANN structures with different hidden layers and hidden neuron numbers, fission barrier height data of odd-odd and odd-even 988 isotopes were used [12]. 30% of these data were used as test data in testing the model. The data range is between 91 and 120 for the number of protons and between 140 and 215 for the number of neutrons. Proton, neutron, and mass numbers are used as inputs of the ANN. Table 1 shows mean absolute error (MAE), mean square error (MSE) and median absolute error (MedE) values for the estimations of the ANN in different structures. As can be seen from the table, the number of hidden layers was increased from 1 to 4 and calculations were made separately. As for the number of neurons in the hidden layers, either 6, 12 or 18 were used. The smallest MAE, MSE and MedE values were obtained in the structure of (3-18-18-18-18-1) as seen. In this structure, there are four hidden layers and there are 18 hidden neurons in each layer. MAE, MSE and MedE values were obtained as 0.06, 0.005 and 0.06, respectively.

In cases where the number of hidden layers is considered as constant, it is seen that the increase in the number of hidden neurons leads to a decrease in MAE, MSE and MedE values. It is seen that the increase in the number of hidden layers causes similar results, that is, increases the performance. However, it was concluded that there is no significant difference between 3 hidden layers and 4 hidden layers, so a significant improvement cannot be achieved after 3 hidden layers.

Table 1. Statistical performances of the different structures of the used ANN

Hidden Layer #	NN Structure		MAE	MSE	MedE
1	(3-6-1)		0.19	0.05	0.19
	(3-12-1)		0.20	0.06	0.18
	(3-18-1)		0.15	0.03	0.13
2	(3-6-6-1)		0.14	0.03	0.13
	(3-12-12-1)		0.12	0.02	0.10
	(3-18-18-1)		0.10	0.02	0.09
3	(3-6-6-6-1)		0.11	0.02	0.10
	(3-12-12-12-1)		0.09	0.01	0.07
	(3-18-18-18-1)		0.07	0.007	0.06
4	(3-6-6-6-6-1)		0.11	0.02	0.10
	(3-12-12-12-12-1)		0.07	0.008	0.06
	(3-18-18-18-18-1)		0.06	0.005	0.06

In the upper panel of Fig. 1, the distributions of the estimates of the calculations made with the ANN in the structure (3-8-8-8-8-1) versus the theoretical values available in the literature are shown. As can be seen, this distribution is concentrated around the diagonal line. In the lower panel of the figure, the differences of the estimates from the theoretical values are shown. It is seen that this distribution of the differences is between +2 and -1. There are several outliers that cross these boundaries. Both these figures and statistical performance indicators indicate that the ANN method can be a useful tool for determining fission barrier height.

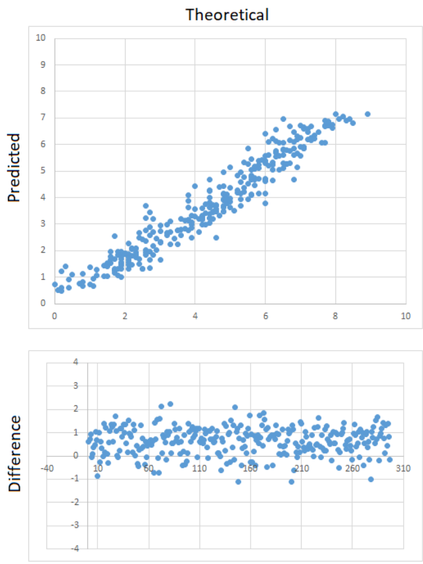

Fig.1. Comparisons of theoretical and ANN predictions for fission barrier heights (upper panel). Differences between theoretical and predicted values on test data shown in the lower panel.

Fission barrier height estimations made with six different machine learning can be accessed with the online calculation module at "*https://cunsg.shinyapps.io/FisBar/*". Estimates of different models can be calculated by entering the number of protons and neutrons belonging to the isotope whose barrier height is desired to be calculated. In addition, statistical performance indicators of each model and the comparisons with current theoretical values in the literature are also presented by graphics on the page.

References

[1] K. Mahata, S. Kailas and S.S. Kapoor, “Fission barriers and shell corrections at the saddle point for mass ~200”, Prog. Part. Nucl. Phys., vol. 59, pp. 305–7, 2007.

[2] S. Akkoyun and T. Bayram, “Estimations of fission barrier heights for Ra, Ac, Rf and Db nuclei by neural networks”, Int. J. Mod. Phys. E, vol. 23, pp. 1–9, 2014.

[3] M. Kowal, P. Jachimowicz and A. Sobiczewski, “Fission barriers for even-even superheavy nuclei”, Phys. Rev. C—Nucl. Phys., vol. 82, pp. 1–10, 2010.

[4] M. Bender, et al, “Future of nuclear fission theory”, J. Phys. G Nucl. Part. Phys., vol. 47, pp. 113002, 2020.

[5] M.G. Itkis, Y.T. Oganessian and V.I. Zagrebaev, “Fission barriers of superheavy nuclei”, Phys. Rev. C—Nucl. Phys., vol. 65, pp. 7, 2002.

[6] J. R. Quinlan, “Learning with continuous classes”, Aust. Jt. Conf. Artif. Intell., vol. 92, pp. 343, 1992.

[7] L. Breiman, “Random Forests”, Mach. Learn., vol. 45, pp.5, 2001.

[8] T. Chen and C. Guestrin, “XGBoost: A Scalable Tree Boosting System”, arXiv:1603.02754v3, 2016.

[9] H. Drucker, C. J. C. Surges, L. Kaufman, A. Smola and V. Vapnik, “Support Vector Regression Machines”, Adv. Neural Inf. Process. Syst., vol. 1, pp. 15, 1997.

[10] J.H. Friedman, "Multivariate Adaptive Regression Splines", The Annals of Statistics, vol. 19, pp. 1–67, 1991.

[11] S. Haykin, Neural Networks: a Comprehensive Foundation, Englewood Cliffs, Prentice-Hall, New Jersey, 1998.

[12] A. Mamdouh, J.M. Pearson, M. Rayet and F. Tondeur, “Fission barriers of neutron-rich and superheavy nuclei calculated with the ETFSI method”, Nucl. Phys. A, vol. 679, pp. 337–58, 2001.

Comparing the concentration of radon in the old and new residential houses in Karabük city/Türkiye using the passive method

Abdulrahman Ahmed Mustafa[1], Khalid H. Mahdi Aal-Shabeeb[1*]

[1]*Karabuk University, Science Faculty, Physics Department, Karabük, 78050, Türkiye*

* Corresponding author e-mail address: khalidaal-shabeeb@karabuk.edu.tr

ORCID Numbers: 0000-0002-1995-6892 (Khalid Mahdi)

Abstract **–** This study is an update of the little information about Radon concentration available for Karabuk region, especially the old residential houses, 10 old residential houses and 15 modern houses were selected in the summer season and 10 old and the same new houses in the winter season. 180 CR-T9 track detectors, four detectors for each house, were suspended in the living and sleeping rooms for a period of one month. The detectors were then collected and chemically etchted. The results indicated that the average radon concentrations in the old houses (with a range of 82.884 to 113.083 Bq/m^3) were higher than in the modern ones (with a range of 55.884 to 77.581 Bq/m^3) by 52.78% in the winter season, and 39.78% in the summer season (with a range of 34.845 to 60.487 Bq/m^3) and (with a range of 32.215 to 51.282 Bq/m^3) respectivily. This is due to the nature of the building materials used and the style of construction (where we find glass facades that occupy larger areas in modern houses). The radioactive indices of radon gas were also calculated, so they were higher in the old houses than in the modern houses, but we find both of them are less than the values recommended by scientific institutions [UNSCEAR & ICRP].

Keywords — *CR-39 Detector, Radon, Old residential houses.*

Introduction

Radon is a noble gas that emitted as result of the decay of radium-226 in the series of natural decay of uranium-238, which is present in the indoor air of residential homes, in addition to the products polonium-218, lead-214, bismuth-214 or polonium 214, as result of its decay with a half-life of 3.8 days. [1,2]. Workers of some professions, especially miners, are exposed to some levels of radiation as result of exposure to radon, which poses a great danger to them by inhalation and ingestion of radon gas, so as for both students and teachers in schools, and peoples in their residential homes [1,3]. In updating information on national exposure to this gas in 66 countries, its found that radon is the second cause of lung cancer [4]. The deaths by this gas as result of exposure amounted to 3% of the total cancer deaths of 226 thousand in 2012, as mentioned by the reference [5]. In addition to this study anther study conducted by Darby (2005) [6], shown an increase in the probability of lung cancer by 16%, when the radon concentration increased by 100 Bq/m^3. While Olsthoom et al. (2022) found a relatively weak positive correlation between the concentration of uranium-238 in the bedrock and according to the type of housing with the concentration of radon in indoor air was statistically significant [7]. International studies have shown that the indoor radon concentration is higher in the winter than in the summer. Due to the high temperature and low pressure, which leads to the escape of leaking radon. Radon accumulates inside the residential homes by existence of cracks in walls, ground foundations, and gaps in pipes and cables, in addition to its emission from building materials and water sources [2,8,9]. The ventilation of the house plays a major role in reducing the annual accumulated dose, which is a source of health concern in the long term [10,11]. The present work was for monitoring the concentrations of indoor radon in Karabuk province by using the alpha-track technique (CR-39) **in** residential buildings that maybe exceed correlate the indoor radon concentrations with house material, geological structure, and designs of houses according to their ages, then estimate the annual effective dose to average adults.

Method and Material

The first step in this work is to record the coordinates of the residential sites that chosen, and their symbols, which presented in table number one. Houses selected as follow, 10 old residential houses and 15 new houses in the summer season 2022, 10 old and the same new houses in the winter season 2022. One hundred eighty CR-39 track detectors was cut into an area of 1 cm^2 and distributed as follow, four detectors in each house, which suspended in the living and sleeping rooms for a period of one month. These detectors were kept inside a sponge in suitable dimensions to preserve them as in figure-1.

Fig. 1. The hanging of the detector in a sponge.

Table 1. The coordinates of the residential sites and their symbols.

Modern residential (new)					Old residential				
	North	*East*	*symbol*			*North*	*East*	*symbol*	
			summer	*winter*				*summer*	*winter*
1	41° 22' 07"	32° 66' 53"	S1na,b	W1na,b	1	41° 19' 81"	32° 61' 68"	S1oa,b	W1oa,b
2	41° 22' 23"	32° 66' 67"	S2na,b	W2na,b	2	41° 19' 82"	32° 61' 67"	S2oa,b	W2oa,b
3	41° 21' 95"	32° 67' 09"	S3na,b	W3na,b	3	41° 21' 17"	32° 62' 49"	S3oa,b	W3oa,b
4	41° 21' 18"	32° 62' 49"	S4na,b	W4na,b	4	41° 22' 01"	32° 67' 30"	S4oa,b	W4oa,b

5	41° 22' 06"	32° 66' 54"	S5na,b	W5na,b	5	41° 22' 05"	32° 66' 50"	S5oa,b	W5oa,b
6	41° 21' 84"	32° 65' 44"	S6na,b	W6na,b	6	41° 21' 78"	32° 65' 72"	S6oa,b	W6oa,b
7	41° 22' 14"	32° 66' 06"	S7na,b	W7na,b	7	41° 13' 42"	32° 39' 40"	S7oa,b	W7oa,b
8	41° 22' 07"	32° 66' 00"	S8na,b	W8na,b	8	41° 13' 42"	32° 40' 03"	S8oa,b	W8oa,b
9	41° 21' 80"	32° 66' 13"	S9na,b	W9na,b	9	41° 14' 37"	32° 41' 39"	S9oa,b	W9oa,b
10	41° 21' 86"	32° 66' 19"	S10na,b	W10na,b	10	41° 12' 16"	32° 37' 47"	S10oa,b	W10oa,b
11	41° 23' 07"	32° 66' 52"	S11na,b	W11na,b					
12	41° 13' 55"	32° 40' 07"	S12na,b	W12na,b					
13	41° 14' 10"	32° 40' 45"	S13na,b	W13na,b					
14	41° 15' 04"	32° 40' 46"	S14na,b	W14na,b					
15	41° 12' 14"	32° 37' 32"	S15na,b	W15na,b					

The detectors were collected after a period of exposure, then detectors transferred to a chemical etching process using a sodium hydroxide solution with normality of 6.25 at a temperature of 60^o C for 6 hours, these detectors cleaned with distilled water, then dried. After that tracks density were calculating using an optical microscope type (Zoomex XSP-44SM) with a magnification of 400X to get radon concentration, after comparing it with the standard source (Fig -2) using the following equations [12]:

$C_{Rn}= E_s/\rho_s \cdot (\rho/t)$ ....(1)

where ρ the track density (number of tracks / mm^2) of the detectors.t : the exposure time (days), E_s: the radon exposure of standard source (Bq.day.m^{-3}) and ρ_s: the track density of the standard source. If *k* is the calibration factor, then equation (1) can be written as the following:

$C_{Rn}\ (Bq/m^3\ ) = (\rho/kt)$ ....(2)

where *k* is the slope in Fig. (2), which is equal to 0.169 Track. m^3 / Bq.Day.mm^2. The graph done by a group in college of education for pure sciences / Ibn Al-Haithem / University of Baghdad. Radiation indices were calculated by using the following equations:

a- The annual effective dose given by[13]:

$$D\ (mSv/y) = C_{Rn}.E.h.t.f \quad \text{......................(3)}$$

b- The lung cancer cases for each year for every million people given by [14,15]:

$$LCCP\ (\ WLM\ ) = D\ x18x10^{-6} \quad \text{......................(4)}$$

c-The concentration of potential Alpha energy given by [14, 15]:

$$PAE\ (WL) = E\ .C_{Rn}/3700 \quad \text{................................(5)}$$

d- The dose rate for soft tissue and lungs by inhaled radon given by[16]:

$$\dot{D}_{soft\ tissues}\ (nGyh^{-1}) = 0.005\ C_{Rn.air}\ (Bq/m^3) \quad \text{.................(6)}$$

$$\dot{D}_{soft\ tissues}\ (nGyh^{-1}) = 0.004\ C_{Rn.air}\ (Bq/m^3) \quad \text{.................(7)}$$

e- The effective equivalent dose rate given by[17]:

$$\dot{H}_{eff}\ (nSvh^{-1}) = 0.18C_{Rn.air}\ (Bq/m^3) \quad \text{........................(8)}$$

Results and Discussion

Observing the results in tables 1, 2, 3, and 4, it was found in Table 1 that the highest concentration of radon recorded in sample No. W3oa was (113.084 Bq/m$^{3)}$ and the lowest concentration in sample W5oa was (82.183 Bq/m^3) in the winter season and for the old residential homes. As Table 2 indicates that the highest concentration of radon in the modern residential homes for the winter season was 77.581 Bq/m^3 in sample W1na, and the lowest concentration was (55.834 Bq/m^3) in sample W2na. Table No. 3 for the the old residential houses in summer season indicated that the highest concentration of radon was 61.144 Bq/m^3 in the S2oa sample, and the lowest concentration was (34.848 Bq/m^3)in the S1oa sample. In table number four, we note that the highest radon concentration was (51.282 Bq/m^3)in the sample S4nb, and the lowest concentration of radon was (30.901 Bq/m^3) in the sample S8nb. The results in the four tables indicate an increase of 52.78% in the old residential floors over the modern residential floors in the winter season. In the summer, the increase a rate of 39.78%, and this increase for radon is due to more than one reason, including. First, the main reason, as it is known and proven in scientific research, the internal ventilation, which is due to the design of the residential floors. We find that the old ones have little ventilation due to the nature of the cold weather, as most of their walls consist of small windows, while we find the modern ones with large windows that can occupy 30 % of the building. Secondly, the use of more building materials in the abutments and partitions of the old houses, and this, as is well known, contributes to building materials that lead to an effective increase in radon concentration because they contain uranium. Thirdly, since radon is one of the daughters of uranium, which is present in the earth's crust, so we find that the concentration of radon varies from one region to another. Accordingly, we need more information about this role and its specifications, in addition to the latest information about radioactivity in the surface soil, and the type of building materials, for the purpose of identifying the real causes that contribute to the increase in radon concentration and working to reduce its impact. The Health Physics Department of the Cekmece Nuclear Research and Training Centre (CNAEM), was the first how start working with internal radon measurements in Turkey. start in 1984, until 2007 published their data about their work [18]. The work included 53 provinces in addition to the work done by Koksal in 1993, Gurel and Cobanoglu 1997[18], these studies did not include Karabuk governorate, except the study done by Celebi and Ulug, 2002[19], which did not follow the comparison approach between the old and modern residential homes for the summer and winter seasons. Table 5 shows the most important results of local studies. As for Table No. 6, shows some results of the internal radon concentration of some countries near and far from Turkey, where the results of this work can be compared with the results mentioned in the two tables, which show their compatibility with the local results, and their closeness to the results of nearby countries with close geological formation. The tables 1,2,3, and 4 also showed that radiation indices AED (mSv/y), LCR (WLM) per 10^6 persons, PAEC (mWL), D_{soft} (nGy/h), D_{lung} (nGy/h), and H_{eff} (nSv/h) ranged (1.140-2.853),(4.15x10^{-2}-8.39x10^{-2}),(0.006797-0.013753),(0.279-0.411),(2.235-3.287), and(10.059-14.793) respectivily for winter season, and (0.783-1.543),(2.29x10-2-4.54x10-2),(0.003758-0.007436),(0.155-0.306),(1.236-2.446), and (5.562-11.006) for summer season. All these results less than the values recomanded by by the international agencies UNSCEAR, WHO&ICRP [8,18, 16].

Table 1. Radon concentrations and it`s indices for old residential in winter season.

s.no	**track density (rho) (track/ mm^2)**	**Rn conc. (C_{Rn}) (Bq/m^3)**	**AED (mSv/y)**	**LCR (WLM) per 10^6 persons**	**PAEC (mWL)**	**D_{soft} (nGy/h)**	**D_{lung} (nGy/h)**	**H_{eff} (nSv/h)**
W1oa	1500	98.619	2.488047	7.32E-02	0.011994	0.493	3.945	17.751
W1ob	1530	100.592	2.537808	7.46E-02	0.012234	0.503	4.024	18.107
W2oa	1270	83.498	2.106547	6.19E-02	0.010155	0.417	3.340	15.030
W2ob	1430	94.017	2.371938	6.97E-02	0.011435	0.470	3.761	16.923
W3oa	1720	113.084	2.852961	8.39E-02	0.013753	0.565	4.523	20.355
W3ob	1670	109.796	2.770026	8.14E-02	0.013354	0.549	4.392	19.763
W4oa	1550	101.907	2.570982	7.56E-02	0.012394	0.510	4.076	18.343
W4ob	1400	92.045	2.322178	6.83E-02	0.011195	0.460	3.682	16.568
W5oa	1250	82.183	2.073373	6.1E-02	0.009995	0.411	3.287	14.793
W5ob	1330	87.442	2.206069	6.49E-02	0.010635	0.437	3.498	15.740
W6oa	1520	99.934	2.521221	7.41E-02	0.012154	0.500	3.997	17.988
W6ob	1620	106.509	2.687091	7.9E-02	0.012954	0.533	4.260	19.172
W7oa	1320	86.785	2.189482	6.44E-02	0.010555	0.434	3.471	15.621
W7ob	1590	104.537	2.63733	7.75E-02	0.012714	0.523	4.181	18.817
W8oa	1440	94.6746	2.388525	7.02E-02	0.011514	0.473	3.787	17.041
W8ob	1260	82.840	2.08996	6.14E-02	0.010075	0.414	3.314	14.911
W9oa	1390	91.387	2.305591	6.78E-02	0.011115	0.457	3.655	16.450
W9ob	1500	98.619	2.488047	7.32E-02	0.011994	0.493	3.945	17.751
W10oa	1540	101.249	2.554395	7.51E-02	0.012314	0.506	4.050	18.225
W10ob	1500	98.619	2.488047	7.32E-02	0.011994	0.493	3.945	17.751

Table 2. Radon concentrations and it`s indices for new residential in winter season.

s.no	**track density (rho) (track/ mm^2)**	**Rn conc. (C_{Rn}) (Bq/m^3)**	**AED (mSv/y)**	**LCR (WLM) per 10^6 persons**	**PAEC (mWL)**	**D_{soft} (nGy/h)**	**D_{lung} (nGy/h)**	**H_{eff} (nSv/h)**
W1na	1180	77.581	1.957264	5.75E-02	0.009435	0.388	3.103	13.965
W1nb	960	63.116	1.59235	4.68E-02	0.007676	0.316	2.525	11.361
W2na	850	55.884	1.409893	4.15E-02	0.006797	0.279	2.235	10.059
W2nb	920	60.487	1.526002	4.49E-02	0.007356	0.302	2.419	10.888
W3na	940	61.801	1.559176	4.58E-02	0.007516	0.309	2.472	11.124
W3nb	920	60.487	1.526002	4.49E-02	0.007356	0.302	2.419	10.888
W4na	940	61.801	1.559176	4.58E-02	0.007516	0.309	2.472	11.124
W4nb	900	59.172	1.492828	4.39E-02	0.007197	0.296	2.367	10.651
W5na	870	57.199	1.443067	4.24E-02	0.006957	0.286	2.288	10.295
W5nb	990	65.089	1.642111	4.83E-02	0.007916	0.325	2.604	11.716
W6na	900	59.172	1.492828	4.39E-02	0.007197	0.296	2.367	10.651
W6nb	990	65.089	1.642111	4.83E-02	0.007916	0.325	2.604	11.716
W7na	930	61.144	1.542589	4.54E-02	0.007436	0.306	2.446	11.006
W7nb	980	64.431	1.625524	4.78E-02	0.007836	0.322	2.577	11.598
W8na	850	55.884	1.409893	4.15E-02	0.006797	0.279	2.235	10.059

W8nb	1080	71.006	1.791394	5.27E-02	0.008636	0.355	2.840	12.781
W9na	1060	69.691	1.75822	5.17E-02	0.008476	0.348	2.788	12.544
W9nb	1040	68.376	1.725046	5.07E-02	0.008316	0.342	2.735	12.308
W10na	930	61.144	1.542589	4.54E-02	0.007436	0.306	2.446	11.006
W10nb	960	63.116	1.59235	4.68E-02	0.007676	0.316	2.525	11.361

Table 3. Radon concentrations and it`s indices for old residential in summer season.

s.no	track density (rho) (track/m m^2)	Rn conc. (C_{Rn}) (Bq/m^3)	AED (mSv/y)	LCR (WLM) per 10^6 persons	PAEC (mWL)	D_{soft} (nGy/h)	D_{lung} (nGy/h)	H_{eff} (nSv/h)
S1oa	900	59.172	1.492828	4.39E-02	0.007197	0.296	2.367	10.651
S1ob	800	52.597	1.326959	3.9E-02	0.006397	0.263	2.104	9.467
S2oa	930	61.144	1.542589	4.54E-02	0.007436	0.306	2.446	11.006
S2ob	790	51.940	1.310372	3.85E-02	0.006317	0.260	2.078	9.349
S3oa	920	60.487	1.526002	4.49E-02	0.007356	0.302	2.419	10.888
S3ob	900	59.172	1.492828	4.39E-02	0.007197	0.296	2.367	10.651
S4oa	810	53.254	1.343546	3.95E-02	0.006477	0.266	2.130	9.586
S4ob	890	58.514	1.476241	4.34E-02	0.007117	0.293	2.341	10.532
S5oa	770	50.625	1.277198	3.76E-02	0.006157	0.253	2.025	9.112
S5ob	810	53.254	1.343546	3.95E-02	0.006477	0.266	2.130	9.586
S6oa	740	48.652	1.227437	3.61E-02	0.005917	0.243	1.946	8.757
S6ob	730	47.995	1.21085	3.56E-02	0.005837	0.240	1.920	8.639
S7oa	770	50.625	1.277198	3.76E-02	0.006157	0.253	2.025	9.112
S7ob	780	51.282	1.293785	3.8E-02	0.006237	0.256	2.051	9.231
S8oa	770	50.625	1.277198	3.76E-02	0.006157	0.253	2.025	9.112
S8ob	730	47.995	1.21085	3.56E-02	0.005837	0.240	1.920	8.639
S9oa	790	51.940	1.310372	3.85E-02	0.006317	0.260	2.078	9.349
S9ob	730	47.995	1.21085	3.56E-02	0.005837	0.240	1.920	8.639
S10oa	530	34.846	1.094741	3.22E-02	0.005277	0.217	1.736	7.811
S10ob	530	34.846	0.87911	2.58E-02	0.004238	0.174	1.394	6.272

Table 4. Radon concentrations and it`s indices for new residential in summer season.

s.no	track density (rho) (track/m m^2)	Rn conc. (C_{Rn}) (Bq/m^3)	AED (mSv/y)	LCR (WLM) per 10^6 persons	PAEC (mWL)	D_{soft} (nGy/h)	D_{lung} (nGy/h)	H_{eff} (nSv/h)
S1na	500	32.873	0.829349	2.44E-02	0.003998	0.164	1.315	5.917
S1nb	540	35.503	0.895697	2.63E-02	0.004318	0.178	1.420	6.391
S2na	530	34.846	0.87911	2.58E-02	0.004238	0.174	1.394	6.272
S2nb	600	39.448	0.995219	2.93E-02	0.004798	0.197	1.578	7.101
S3na	570	37.475	0.945458	2.78E-02	0.004558	0.187	1.500	6.746
S3nb	640	42.079	1.061567	3.12E-02	0.005118	0.210	1.683	7.574
S4na	680	44.707	1.127915	3.32E-02	0.005437	0.224	1.788	8.048
S4nb	780	51.282	1.293785	3.8E-02	0.006237	0.256	2.051	9.231
S5na	650	42.735	1.078154	3.17E-02	0.005198	0.214	1.709	7.692

S5nb	760	49.967	1.260611	3.71E-02	0.006077	0.250	1.999	8.994
S6na	580	38.133	0.962045	2.83E-02	0.004638	0.191	1.525	6.864
S6nb	630	41.420	1.04498	3.07E-02	0.005038	0.207	1.657	7.456
S7na	600	39.448	0.995219	2.93E-02	0.004798	0.197	1.578	7.101
S7nb	630	41.420	1.04498	3.07E-02	0.005038	0.207	1.657	7.456
S8na	720	47.337	1.194263	3.51E-02	0.005757	0.237	1.893	8.521
S8nb	470	30.901	0.779588	2.29E-02	0.003758	0.155	1.236	5.562
S9na	570	37.475	0.945458	2.78E-02	0.004558	0.187	1.499	6.746
S9nb	550	36.160	0.912284	2.68E-02	0.004398	0.181	1.446	6.509
S10na	580	38.133	0.962045	2.83E-02	0.004638	0.191	1.525	6.864
S10nb	640	42.078	1.061567	3.12E-02	0.005118	0.210	1.683	7.574
S11na	590	38.790	0.978632	2.88E-02	0.004718	0.194	1.552	6.982
S11nb	620	40.763	1.028393	3.02E-02	0.004958	0.204	1.631	7.337
S12na	550	36.160	0.912284	2.68E-02	0.004398	0.181	1.446	6.509
S12nb	670	44.050	1.111328	3.27E-02	0.005357	0.220	1.762	7.929
S13na	580	38.133	0.962045	2.83E-02	0.004638	0.191	1.525	6.864
S13nb	570	37.475	0.945458	2.78E-02	0.004558	0.187	1.500	6.746
S14na	530	34.846	0.87911	2.58E-02	0.004238	0.174	1.394	6.272
S14nb	550	36.160	0.912284	2.68E-02	0.004398	0.181	1.446	6.509
S15na	620	40.763	1.028393	3.02E-02	0.004958	0.204	1.631	7.337
S15nb	490	32.216	0.812762	2.39E-02	0.003918	0.161	1.289	5.799
Global limit		200 - 300 (Bq/m3) [20]	3-10 (mSv/y) [18]	170-230 [8]				3-10 mSv.y^{-1} [17]

Table 5. Some important local studies in Türkiye.

Area	**Mean concentration of radon Bq/m^3**	**Reference**	**Author**	**Year**
İzmir -Dikili geothermal area	114	14	Y. Yarar	2006
Sivas	120	18	Mihci, M et al.	2010
Artvin and Ardahan provinces	21-321 & 53-736	13	B. Kucukomeroglu et al.	2011
Samsun province	106	15	B. Kucukomeroglu et al.	2012
81 province	81	19	N. Celebi et.al.	2014
Karabuk (average)	60-92 at winter 37-51 at summer	Present work		2022

Table 6. Average radon concentrations in some countries.

No.	**Country**	**Average Radon Concentration (Bq/m^3)**	**Reference**
1	**Cyprus**	7	(22)
2	**Greece**	73	(23)
3	**Italy**	75	(24)
4	**France**	62	(25)
5	**Hungary**	107	(26)
6	**Iran**	82	(27)
7	**Syria**	10	(28)

8	**Pakistan**	30	(29)
9	**Egypt**	9	(30)
10	**UNSCEAR**	**Median** 46	(8)

Conclusion

Through the results obtained, we conclude that radon concentrations inside old dwelling in karabuk province were more than modern ones. This is due to the nature of the building materials used and the style of construction (where we find glass facades that occupy larger areas in modern houses), these results were in agreement with N. Celebi et al (2014,2022). The radioactive indices of radon gas were also calculated, so they were higher in the old houses than in the modern houses, but we find both of them are less than the values recommended by scientific institutions [UNSCEAR & ICRP]. This study is an addition and update to the data available in Türkiye.

References

[1] ICRP, Lung cancer risk from radon and progeny and statement on radon. ICRP Publication 115. Ann. ICRP 40 (1), 2010.

[2] WHO, WHO handbook on indoor radon: a public health perspective. World Health Organization 9789241547673, 2009.

[3] Abdallah S. M., Habib R. R., Nuwayhid R. Y., Chatila M., and Katul G., "Radon measurements in well and spring water in Lebanon," *Radiat Meas*, vol. 42, no. 2, pp. 298–303, 2007, doi: 10.1016/j.radmeas. 11.004. 2006.

[4] Gaskin, J., Coyle, D., Whyte, J., Krewski, D., Global estimate of lung cancer mortality attributable to residential radon. Environ. Health Perspect. 126 (5), 057009. https://doi.org/10.1289/EHP2503. 2018.

[5] Christopher L. Rääf , Martin T., Mats I., Robert ., "Average uranium bedrock concentration in Swedish municipalities predicts male lung cancer incidence rate when adjusted for smoking prevalence": Indication of a cumulative radon induced detriment, Science of the Total Environment, 855, 158899,2023.

[6] Darby S., et al., "Radon in homes and risk of lung cancer: collaborative analysis of individual data from 13 european case-control studies". BMJ 330 (7485), 223, DOI: 10.1136/bmj.38308.477650.63. 2005.

[7] Olsthoorn, B., Ronnqvist, T., Lau, C., Rajasekaran, S., Persson, T.,Månsson, M., Balansky, A.V., 811, 151406, https://doi.org/10.1016/j.scitotenv.2021.151406. 2022.

[8] United Nations Scientific Committee on the Effects of Atomic Energy, UNSCEAR 2000 Report to the General Assembly, with Scientific Annexes. Volume I: SOURCES, Annex A: Dose Assessment Methodologies. United Nations, New York. http://www.unscear.org/docs/reports/annexa.pdf. 2000.

[9] Cinelli, G., De Cort, M., Tollefsen, T. (Eds.), European Atlas of Natural Radiation. Publication Office of the European Union, Luxembourg, 2019.

[10] World Health Organization (WHO), Fact Sheets, Radon and Health, 2 February 2021, Radon and health (who.int), 2021.

[11] International Commission on Radiological Protection, Radiological Protection against Radon Exposure. Oxford: Pergamon Press; ICRP Publication 126, Ann. ICRP, 43(3), 2014.

[12] Turkish Atomic Energy Authority."Regulations for the radiation safety, Official Journal, Date/Number: 24.03. 2000.

[13] B. Kucukomeroglu, Y. O. Yesilbag, A. Kurnaz, N. Celik, U. Cevik, and N. Celebi, Radiological characterisation of Artvin and Ardahan provinces of Turkey, Radiation Protection Dosimetry, vol. 145, no. 4, pp. 389-394, 2011.

[14] Yarar, T. Günaydi and N. Çelebi, Determination of radon concentrations of the Dikili geothermal area in western Turkey, Radiation Protection Dosimetry, vol. 118, no. 1, pp. 78-81, 2006.

[15] B. Kucukomeroglu, F. Maksutoglu, N. Damla, U. Cevik and N. Celebi, A study of environmental radioactivity measurements in the Samsun province, Turkey, Radiation Protection Dosimetry, vol. 152, no. 4, pp. 369-375, 2012.
[16] H. Zeeb, F. Shannoun, and W. H. Organization, WHO Handbook on Indoor Radon: A Public Health Perspective World Health Organization, 2009.
[17] International Commission on Radiological Protection(ICRP),"Protection against Radon-222 at home and at work," PERGAMON, publishing 65,volume 2,No.2,1993.
[18] M. Mihci, A. Buyuksarac, A. Aydemir, N. Celebi, "Indoor and outdoor Radon concentration measurements in Sivas, Turkey,in comparison with geological setting," Journal of Environmental Radioactivity 101 (2010) 952-957.
[19] N. Celebi, B. Ataksor, H. Taskın and N. Albayrak Bingoldag "Indoor Radon Measurements In Turkey Dwellings", Radiation Protection Dosimetry, pp. 1–7(2014).
[20] S. Kansal, R. Mehra and N. P. Singh, "Life time fatality risk assessment due to variation of indoor radon concentration in dwellings in western Haryana",Applied Radiation and Isotopes, vol. 70, no. 7, pp. 1110-1112, 2012.
[21] International Commission on Radiological Protection (ICRP), "Statement on Radon", 2009.
[22] Christofides, S. and G. Christodoulides. 1993 Airborne 222Rnconcentration in Cypriot houses. Health Phys. 64(4): 392-396 .
[23] Georgiou, E. Ntalles, K. Molfetas, M. Athanassiadis, A. Proukakis, C., "Radon measurements in Greece", Radiation Protection Practice. Proceedings of the 7th International Congress of the International Radiation Protection Association (V- 1). Pergamon Press, Sydney. INIS,V20,N13,1988.
[24] De Bortoli, M. and P. Gaglione;" ^{226}Ra in environmental materials and foods". Health Phys. 22: 43-48. 1972.
[25] Rannou, A. and G. Tymen. "Lesresultats des campagnesdemesures de radon etfacteursexplicatifs". Exposition au Radon dans les Habitations – Aspects Technique et Sanitaires. SFRP, Paris. p. 42-63 ,1989.
[26] Nikl, I. "The radon concentration and absorbed dose rate in Hungarian dwellings". Radiat. Prot. Dosim. 67(3): 225-228, 1996.
[27] Sohrabi, M. and Solaymanian A.R., Indoor radon level measurements in Iran using AEOI passive dosimeters. Radiation Protection Practice. Proceedings of the 7th International Congress of the International Radiation Protection Association (V-1) Pergamum Press, Sydney. p. 242-245, 1988.
[28] Bem, H. Domanski, T. Bakir, Y.Y. Al-Zenki S.,"Radon survey in Kuwait houses. IRPA9, 1996 International Congress on Radiation Protection. Proceedings, Volume 2. IRPA,Vienna. p. 101-103,1996.
[29] Tufail M., Amin M., Akhtar W., Khan H.A., Qureshi A.A., Manzoor S., "Radon concentration in some houses of Islamabad and Rawalpindi", Pakistan. Nucl. Tracks Radiat. Meas. 19: 429-430. 1991.
[30] Kenawy, M.A. and Morsy A.A.,"Measurements of environmental ^{222}Rn concentration in indoors and outdoors in Egypt". Nucl. Tracks Radiat. Meas. 19: 343-345.1991.

The Utilization of Some Boron-Containing Minerals As Fast Neutron Shielding In Nuclear Power Plants

[1] Rezvan Rezaeizadeh, [2]İlknur Şahin, [3*]Aybaba Hançerlioğullari

[1]*Department of Physics, University Campus -2, University of Guilan, Rasht/Iran*
[2]*Kastamonu University Central Research Laboratory Application and Research Center, Kastamonu/Türkiye*
[3*]*Department of Physics, Faculty of Science, Kastamonu University, Kastamonu/Türkiye*

*Corresponding author: aybabah@gmail.com

ORCID Numbers:0000-0001-6219-6174 ([1]Rezvan.Rezaeizadeh),0000-0002-4383-3817 ([2]ilknur Şahin), 0000-0000-1700-8480 ([3]*Aybaba Hançerlioğullari)

Abstract – In this study, 3 different boron-doped minerals concentrations shielding materials of cross-sections of calculated with the help of the MCNP program for the use of neutron shielding in nuclear reactors. In addition, some physical and chemical properties, properties and usage areas of these minerals are given. MCNP can be called as the calculation of physical events using probability distribution functions [5]. Deterministic methods answer the question of what is the average response resulting from interactions in the system when the transport of particles in the system is examined. For this purpose, boron, which has many uses the compounds made by the minerals and the places where these compounds are used are investigated. Neutron shielding is most effective is the nucleus of the shield material has about the same mass as the neutron. This makes hydrogen rich materials excellent neutron shits. There needs also to be something to absorb the neutrons, boron being the poison of choice. We have investigated fast neutron shielding properties of Vimsite ($CaB_2O_2(OH)4$), Sussexite ($Mn^{+2}BO_2(OH)$and Veatchite ($Sr_2B_{11}O_{16}(OH)5.(H_2O)$ samples simulation process. Recently shielding is an important issue because of neutrons which have many applications today do not harm living tissue. Different compounds, alloys and composites are usually preferred against neutrons as shielding material.

Keywords – *Cross-sections, Boren, nuclear fission, nuclear power plane, neutron shilding, MCNP*

Introduction

Boron isotopes are neutrons during the nuclear reaction. It prevents and slows down the fission reaction of neutrons with uranium-235 with its absorption and slowing properties. Boron minerals and compounds contain ^{10}B and ^{11}B isotopes [1]. Therefore, boron enriched boron oxide is used in the construction of the moderators of the control rods of the nuclear reactor. In this study, the use of boron mineral, which has the largest reserve share in the world in Turkey, in the nuclear field, especially in nuclear power plants currently operating and under construction, as neutron capture and neutron shielding has been emphasized. In terms of boron reserves ownership, Turkey ranks first in world refined boron production with a share of approximately %72. In this study, MCNP (Monte Carlo Transport Particals) nuclear code used. Also, in simulation calculations, neutron macroscopic cross section and average path calculations were made for 3 different boron (Vimsite ($CaB_2O_2(OH)4$), Sussexite ($Mn^{+2}BO_2(OH)$ and Veatchite ($Sr_2B_{11}O_{16}(OH)5.(H_2O)$) doped materials. Monte Carlo codes extensively used for probabilistic simulation of various physical systems. These code are widely used in calculations of neutron radiation shielding and gamma ray transport in materials Monte Carlo methods are very different from deterministic transport methods. Deterministic methods, the most common of which is the discrete ordinates method, solve the transport equation for the average particle behavior. On the other hand, Monte Carlo does not solve an explicit equation, but rather obtains answers by simulating individual particles and recording some aspects of their average behavior. Boron minerals are generally old in the earth's crust occurs between sedimentary layers [3-5]. However, in boron regions, volcanic rocks are also are found. Volcanic rocks are usually andesite. Boron-containing minerals and compounds are increasing day by day. The importance of its use in nuclear reactor technology was emphasized. Boron minerals are generally Na+, Ca++ and they are aqueous borates combined with an alkali cation such as Mg++. Many of the more than 2100 boron minerals found in nature although they are very similar in composition, they differ due to the different amount of crystal water they contain in their structures. Boron minerals contain boron oxide in different proportions in their structures. Those with the commercial value; Borax, Colemanite, Ulexite, Probertite, Boracite, Pandermite, Hydroboracite and Kernit. Boron in the manufacture of control rods in nuclear reactors steels, boron carbides and titanium boron alloys are used. These are mostly in the form of amorphous boron or crystalline boron. Stainless boron steel as neutron absorber preferred. Each boron atom absorbs about one neutron. Calcium boron is also used for neutron shielding in the storage of nuclear waste. Bore is used as a neutron barrier. With the control systems of nuclear reactors. Boron used in cooling pools and emergency shutdown of the reactor (^{10}B).

The Neutron Shielding of Materials

Neutron particles create different effects from other types of radiation due to their direct interaction with the atomic nucleus and their indirect ionization structure. High-energy radiation (Gamma, Alpha, Beta, X-rays etc.) resulting from shielding of neutrons produced in applications is of great importance in terms of both human health and the safety of the reactor, as well as protection from radiation in terms of long-term work of the working personnel. For this aim, armoring of doors and walls in the radiation zone is required. Depending on the type of radiation generated, the shielding materials to be used differ. For example, lead for gammas etc. While materials are used, materials containing hydrogen and boron are generally used for neutron shielding. Neutron shielding is most effective is the nucleus of the shield material has about the same mass as the neutron. This makes hydrogen rich materials excellent neutron shits [3-6].There needs also to be something to absorb the neutrons, boron being the poison of choice. Conversely gamma shielding requires neutrons with very high mass were it not for the presence of the neutrons, depleted or native uranium would be the best choice (in fact depleted uranium is commonly used as shielding material for X-ray machines and radiography sources), but since neutrons and uranium shielding would be counterproductive, lead is used instead. Nuclear studies is to determine the neutron flux distribution in the environment of (n,p), (n,d), (n,t), (n,3He), (n,α) nuclear reactions in itiated by neutrons, the reaction. Since the formation of neutron products is a function of neutron energy, the neutron flux distribution depends on the neutron energy must also be stated accordingly [7-8]. Factors affecting neutron flux distribution, neutron and nucleus and the atomic density of the medium material and the geometry of the medium with neutrons. The reactions between the media material can be expressed mathematically with the help of the cross section. In simplest form shielding involves interposing distance and materials between the source and recipient of radiation. Design considerations and the calculation of resultant dose complicate the problem. To gain some insight into shielding into shielding calculations we shall consider an oversimplified situation which involves a point source of radiation [9-11]. According to the inverse-square law, the intensity of radiation on the surface of a sphere of radius R will be where P is the source strength (number of particle)

$$I=P/4\Pi R^2 \tag{1}$$

If we place enough distance between ourselves and the source, the intensity of radiation will be reduced to safe levels. However, if we place material between ourselves and the source, we can take advantage of a collimated beam of gammas. The intensity of radiation follows an exponential curve

$$I=I_0\, e^{-\mu x} \tag{2}$$

where μ is linear absorption coefficient and has dimensions of reciprocal centimeters.
A mass absorption coefficient may be defined by $\mu_m = \mu/\rho$. The various types of interactions of neutrons with matter are combined. into a total macroscopic cross section value;

$$\sum_{TOTAL} = \sum_{fission} + \sum_{capture} + \sum_{scatter} + \ldots\ldots\ldots \tag{3}$$

The MCNP Simulations of Boren Materials

The Monte Carlo method is a system based on probability theory. In Monte Carlo method, it is essential to simulate and solve an experiment or a physical event that needs to be solved with statistical and mathematical techniques by using random numbers repeatedly. Today, this method gives good results in nuclear transport calculations using the MCNP (Monte Carlo Particle Transport) code for solving physics and mathematical problems. Monte Carlo simulation more realistic geometry of the facility. Neutron sources are more important in neutron shield measurements. The neutrons originate from spontaneous fission and from some (a,n) reactions in the source materials. The spontaneous fission and (a,n) neutron source terms are dependent on the kind of isotope and the decay time .For the prevent harm living tissue, shielding is an important issue. There are different compounds, alloys or composites are preferred against neutron particles using like shield.The purpose of this study was to shield against neutron radiation can be used as a material in three different mineral containing boron and hydrogen, and the evaluate of interaction these minerals with 4.5 MeV energy neutron using Monte Carlo simulation method. Neutron shielding is most effective is the nucleus of the shield material has about the same mass as the neutron [5-6].This makes hydrogen rich materials excellent neutron shits. It needs also to be something to absorb the neutrons, boron being the poison of choice. Conversely gamma shielding requires neutrons with very high mass. Were it not for the presence of the neutrons, depleted or native uranium would be the best choice (in fact depleted uranium is commonly used as shielding material for X-ray machines and radiography sources), but since neutrons and uranium shielding would be counterproductive, lead is used instead. This nuclear code enables the use of possibility for particles from thermal energy neutrons to all other particles having energy and extensive radiation ranges. Shielding must be provided around a reactor to protect both personnel and material. Shielding that is adequate for neutrons and gamma rays will also stop alfa and beta particles. The weight of shielding to be used is almost independent of the shielding material itself. Table 1 shows that physical properties of boron-containing minerals Veatchite, Sussexite and Vimsite respectively.

Table 1. Some Physical Properties of Boron-Containing Minerals [9].

Properties	**Vimsite**	**Sussexite**	**Veatchite**
Color	Colorless	White, Greenpink, Straw yellow	Colorless, Pearl White
Density	2.54 gr/cm^3	3.12gr/cm^3	2.62gr/cm^3
Hardness	4-Fluorite	3-Calcite	2-Gypsum
Streak	White	White	White
Locality	Siberia-Russia, Buriatia	South Africa, Kalahari	USA,Tick Canyon, Los Angeles,Califonia
Molecular Weight	CaO % 34.67, B_2O_3%43.05, H_2O %22.28	MnO %61.82, B_2O_3 %30.33, H_2O %7.85	SrO %31.73%, B_2O_3 %9.65, H_2O %58.62
Magnetism and Radioactivity	No	No	No

Results and Conclusions

The effects of cross section for high performance materials such as Veatchite, Sussexite and Vimsite were calculated, and also the parameters of the neutron armor of these materials measured. There are many advantage using materials having hydrogen and boron in terms of neutron shielding technology because the neutron shielding capability. Figure-2 shows that compare neutron absorption cross sections minerals and concrete. Simulation shown according to these results, the highest performance among the minerals is Vimsite for the neutron shielding. Interaction of three different boron-containing mineral particles and 4.5 MeV energy neutron were simulated by Monte Carlo techniques. Figure-1 shows that neutron energy of double differentials cross sections flow curve for Mineral Veatchite.

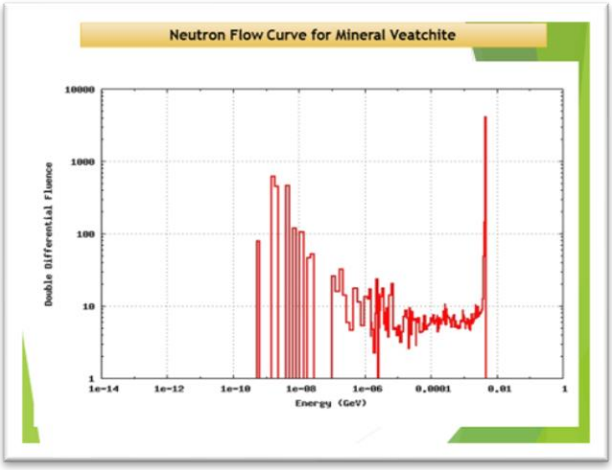

Fig. 1. The neutron flow curve for mineral veatchite

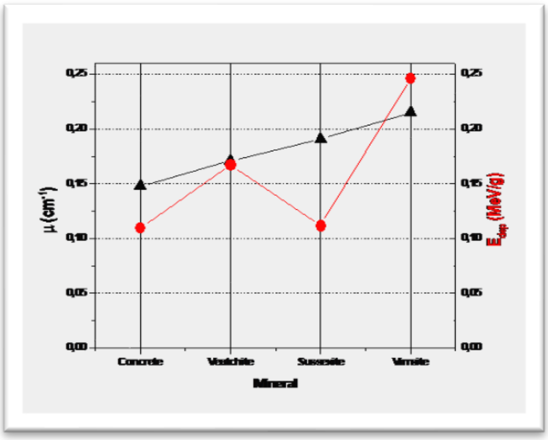

Fig. 2. The compared neutron absorption cross sections minerals and concrete

Conclusion

We have investigated fast neutron shielding properties of Vimsite, Sussexite and Veatchite samples simulation process. Interactivities of neutron particles with 4.5 MeV energy with three different mineral containing boron was simulated by Monte Carlo method. In the consequence of simulation study, isotope production rates, neutron flux and secondary radiation curve was obtained. As a result of interactivities, there were no radioactive isotopes found. Furthermore no secondary radiation with high flux were found. In order to evaluate the minerals in terms of neutron screening, total macroscopic cross sections (μ) and stored energy values identified. For the concrete used in neutron shielding studies, the same values were calculated. It was found that three of the minerals were a better shielding material than concrete[10-11]. It was found that the mineral which has the highest neutron shielding performance among these minerals is Vimsite. The results of this investigation have provided new information about the total macroscopic cross sections, secondary radiation, neutron flow absorbed doses and deposited energies by low energy neutron interaction of fast neutrons through materials including different amounts of boron and hydrogen atoms per unit volume. As a result of simulation studies minerals isotope production rates for the neutron radiation, flows and secondary curves were obtained. According to these results, the highest performance among the minerals is Vimsite for the neutron shielding. As a result of interactions has not found radioactive isotopes.

References

[1] Agosteo S., Magistris M., Mereghetti, A., Shielding data for 100-250 MeV proton accelerators: Double differential neutron distributions. Nuclear instruments and methods in physics research B. 265,581-598, 2007.

[2] Battistoni, G., Francesco, B., Markus, B., Mauro C., et al., Application of FLUKA Monte Carlo code for nuclear and accelerator physics. Nuclear instruments and methods in physics research B.Doi:10.1016/j. nimb, 269.issu 24, 2850-2856, 2011.

[3] Battistoni, G., Ferrari A., Montraruli T., Sala P.R., The FLUKA atmospheric neutrino flux calculation. Astroparticle Physics. 19 269-290, 2003.

[4] Borio di tigliole, A., Cesana, A., Dolfini R. et al., FLUKA simulations for low-energy neutron interactions and experimental validation. Nuclear instruments and methods in physics research A. 469,347-353, 2001.

[5] Bremister J., MCNP-4A General Monte Carlo Code N-Particle Transport Code, Version 4a, La-12625, New-Mexico, 1993.

[6] Gonçalves, I.F., Martinho, E., SalgadoJ., Monte Carlo calculation of epithermal neutron resonance self-shielding factors in wires of different materials. Applied Radiation and Isotopes. 55, 447-451, 2001.

[7] Gonçalves, I.F., Martinho, E., Salgado J., Monte Carlo calculation of resonance self-shielding factors for epithermal neutron spectra. Radiation physics and chemistry and Isotopes. 61, 461-462, 2001.

[8] Hançerlioğulları, A, Monte Carlo simulation method and MCNP code system, Kastamonu Education Journal. 14 545-556. 2006.

[9] http:\\www.mindat.org; http:\\webmineral.com\data,2006.

[10] Korkut, T., Karabulut, A., Budak, G. et al., Investigation of neutron shielding properties depending on number of boron atoms for colemanite, Ulexite and tincal ores by experiments and Fluka Monte Carlo simulations. Applied Radiation and Isotopes. 70, 341-345, 2012.

[11] Patil, B.J., Chavan, S.T, PetheS.N., Krishnan R., DholeS., Measurement of angular distribution of neutron flux for the 6 MeV race-track microton based pulsed neutron source. 68, 1743-1745, 2010.

Rapidity Distributions of Nuclei and Hypernuclei

Nihal Büyükçizmeci[1,*]

[1]*Department of Physics, Faculty of Science, Selçuk University, Konya, Türkiye*

* Corresponding author e-mail address: *nihal@selcuk.edu.tr*

ORCID Numbers: 0000-0002-6030-9574 (Nihal.buyukcizmeci)

Abstract— Rapidity distributions of light nuclei and hypernuclei are benchmarked by using hybrid models including the Ultra-relativistic Quantum Molecular Dynamics Model (UrQMD) and Dubna Cascade Model (DCM) together with Statistical Multifragmentation Model (SMM). As a conclusion, UrQMD results are in agreement with STAR experimental data and very promising for the further investigations in the facilities such as FAIR, LHC, and NICA.

Keywords— *rapidity, UrQMD model, DCM model, SMM model.*

Introduction

According to the knowledge in the literature, relativistic central nucleus-nucleus collisions are one of the scopus sources to obtain new nuclei and hypernuclei [1,2]. Solving the puzzle of formation of nuclei and hypernuclei will contribute to understand nucleosynthesis in the universe. Recent experiments in Refs. [3,4] show that the detection of hypernuclei in relativistic nuclear collisions will be helpful to extend border of the nucleosynthesis investigations for nuclear matter. In this study, on the survey of hybrid model assumptions, comparison of preliminary theoretical results with STAR experimental data [4] for Au+Au collision is presented.

Discussion of Theoretical Hybrid Formalisms

Usage of hybrid approaches have become the 'Standard Model' for heavy-ion collisions. These approaches are successful for the description of dynamics. In the literature, there are many hybrid models to describe stages of collision perspective starting form initial fast processes, to the formation of nuclei and fragmentation processes [5-12]. Recently, I have examined the Ultra-relativistic Quantum Molecular Dynamics Model (UrQMD) [9] and Dubna Cascade Model (DCM) [5, 6] together with Statistical Multifragmentation Model (SMM) [7, 8, 13, 14]. In our previous studies [7,8], we have investigated coalescence mechanism by connecting SMM for the formation of nuclei and hypernuclei at lower energies 20A MeV, 50A MeV, 100A MeV and 200A MeV. In this work, the excited states of nuclei and hypernuclei are taken into account in hybrid model, then one can use hybrid SMM calculations by using coalescence approach and by connecting DCM and UrQMD at higher relativistic energies 1A GeV, 2A GeV and 3A GeV for Au+Au collisions.

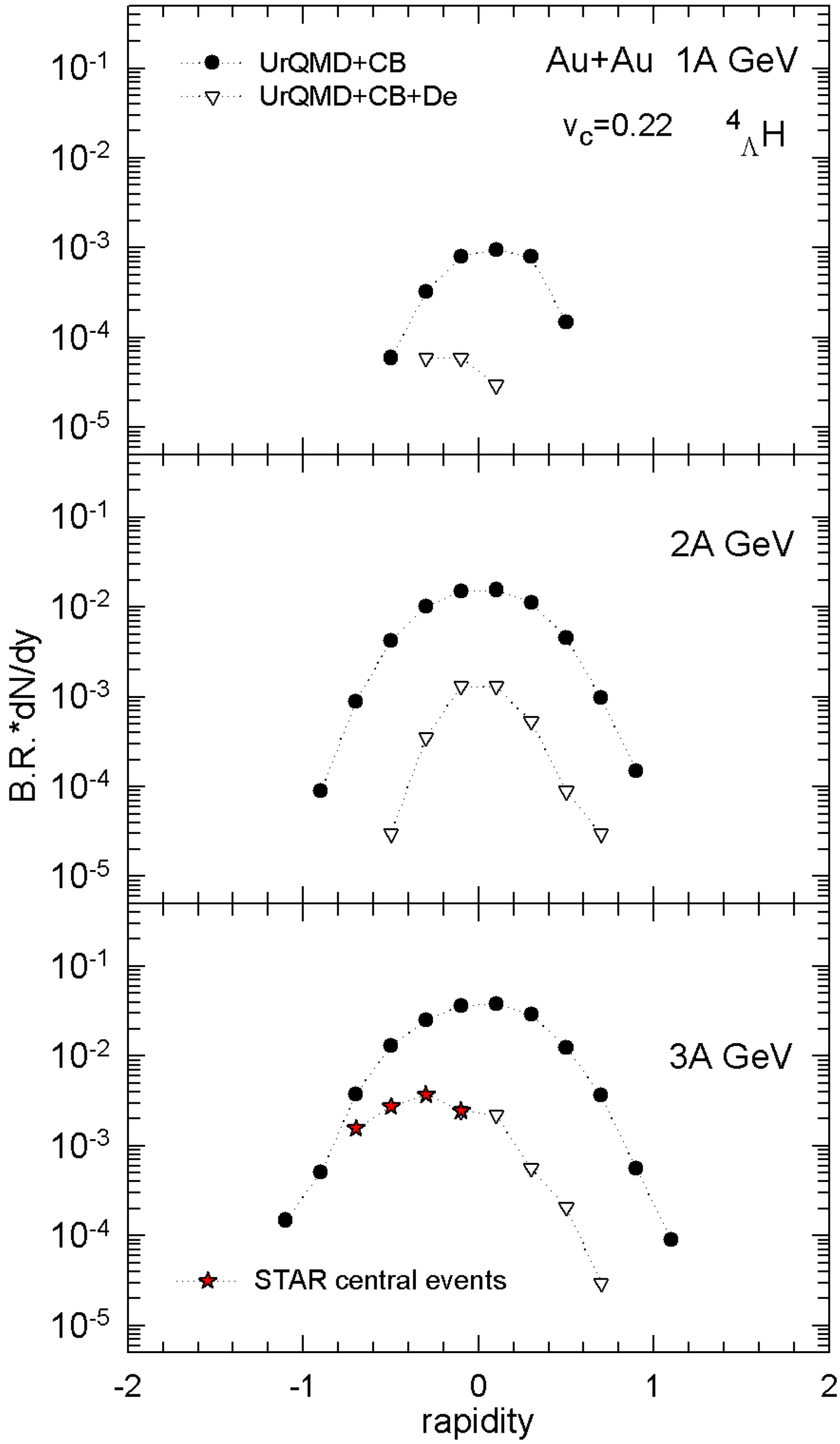

Fig. 1. Comparison of the calculations of the rapidity distributions $^4_\Lambda H$ hypernuclei with STAR experimental data [4]. The model parameters and the rapidity intervals are shown in the panels.

Results and Discussions

Recently, rapidity distribution of ${}^{4}_{\Lambda}H$ hypernuclei produced in Au+Au collision at $\sqrt{s_{NN}}$=3A GeV enegy has been reported in Ref. [4], that is why it is initiated to investigate rapidity distributions. It is also examined 1A GeV, 2A GeV and 3AGeV energies to bridge from small energies to the higher ones. In this study, UrQMD+CB and UrQMD+CB+De (UrQMD+SMM) results are demonstrated for Au+Au collisions at 1A, 2A and 3A GeV energies in Figure 1. STAR experimental data [4] red stars in the bottom panel of Figure 1 for ${}^{4}_{\Lambda}H$ are in agreement with theoretical UrQMD+CB+De (UrQMD+SMM) results. For this calculation freeze-out assumption is used for the formation of initial nucleons in the UrQMD model, after that coalescence mechanism and de-excitation processes are applied by connected via SMM model. The branching decay ratios (B.R.) are taken into account in the calculations for hot primary nuclei (UrQMD+CB) and cold final nuclei (UrQMD+CB+De). Rapidity distributions have Gaussian type distributions in all panels. While rapidity values of hot nuclei have higher probability, after the de-excitation of hot nuclei final nuclei will be formed with lower probability. As a conclusion, it is presented very promising results for the further investigations in the facilities FAIR, LHC, and NICA.

Acknowledgements – N.B. thanks to A.S. Botvina and M. Bleicher for their fruitful discussions and acknowledges support from the Scientific and Technological Research Council of Türkiye (TUBITAK) support under Project No. 121N420.

References

[1] Neubert, W., & Botvina, A. S. (2000). What is the physics behind the 3He-4He anomaly? Eur. Phys. J. A 7, 101.

[2] Reisdorf, W., et al. (2010). Systematics of central heavy ion collisions in the 1A GeV regime. Nucl. Phys. A 848, 366.

[3] Adam, J., et al. (ALICE Collaboration). (2016). ${}^{3}_{\Lambda}H$ and ${}^{3}_{\bar{\Lambda}}\bar{H}$ production in Pb-Pb collisions at $\sqrt{s_{NN}}$=2.76 TeV. Phys. Lett. B 754, 360.

[4] Abdallah, M. S., et al. (STAR Collaboration). (2022). Measurements of ${}^{3}_{\Lambda}\mathbf{H}$ and ${}^{4}_{\Lambda}\mathbf{H}$ lifetimes and yields in Au+Au collisions in the high baryon density region. Phys. Rev. Lett. 128, 202301.

[5] Botvina, A. S., Gudima, K. K., Steinheimer, J., Bleicher, M. & Pochodzalla, J. (2017). Formation of hypernuclei in heavy-ion collisions around the threshold energies. Phys. Rev. C 95, 014902.

[6] Botvina, A. S., Gudima, K. K., & Pochodzalla, J. (2013). Production of hypernuclei in peripheral relativistic ion collisions. Phys. Rev. C 88, 054605.

[7] Botvina, A. S., Buyukcizmeci, N., & Bleicher, M. (2021). Coupling dynamical and statistical mechanisms for baryonic cluster production in nucleus collisions of intermediate and high energies. Phys. Rev. C 103, 064602.

[8] Botvina, A. S., Buyukcizmeci, N., & Bleicher, M. (2022). Evolution of the statistical disintegration of finite nuclei toward high energy. Phys. Rev. C 106, 014607.

[9] Bleicher, M. et al. (1999). Relativistic hadron-hadron collisions in the ultra-relativistic quantum molecular dynamics model. J. Phys. G 25, 1859.

[10] Bondorf, J. P., Botvina, A. S., Iljinov, A. S., Mishustin, I. N. & Sneppen, K. (1995). Statistical multifragmentation of nuclei. Phys. Rep. 257, 133.
[11] Aichelin, J., Bratkovskaya, E., LeFevre, A., Kireyeu, V., Kolesnikov, V., Leifels, Y., Voronyuk, V. & G. Coci, G. (2020). Phys. Rev. C 101, 044905.
[12] Ogul, R., et al. (2011). Isospin-dependent multifragmentation of relativistic projectiles. Phys. Rev. C 83, 024608.
[13] Botvina, A. S., & Pochodzalla, J. (2007). Production of hypernuclei in multifragmentation of nuclear spectator matter. Phys. Rev. C 76,024909.
[14] Buyukcizmeci, N., Botvina, A. S., Ergun, A., Ogul, R., & Bleicher M. (2018). Statistical production and binding energy of hypernuclei. Phys. Rev. C 98, 064603.

16th International Conference on Nuclear Structure Properties (NSP2023),
May 8 – 10, 2023, Karabük University, Karabük, Türkiye

Gamow-Teller Transition Logft Value for Pd-114 Isotope

Mehmet Dağ[1,2*], Necla Çakmak[2]

[1]*Karabük University, Department of Medical Services and Techniques, Vocational School of Health Services, Karabük, Türkiye*
[2]*Karabük University, Faculty of Sciences, Department of Physics, Karabük, Türkiye*

* Corresponding author e-mail address: *mehmetdag@karabuk.edu.tr*

ORCID Numbers: 0000-0002-0074-307X (Mehmet Dağ), 0000-0001-5989-6663 (Necla Çakmak)

Abstract— GT transitions are one of the most common types of spin-isospin-type weak interactions in atomic nuclei [1]. Gamow-Teller (GT) transition is one of the allowed beta decay processes and the isospin selection rule is $\Delta T = 0, \pm 1$. Along with giving information about the nuclear structure, GT transitions are also important for our understanding of many processes in nuclear astrophysics [2]. In this study, the Gamow-Teller transition properties of the Pd-114 isotope were investigated. In the literature, there are studies on beta decay modes of Palladium A=114-120 isotopes using Quasiparticle Random Phase Approximation (QRPA) formalism [3]. The beta decay of the 0+ ground state of Pd-114 is dominated by the beta decay to the 1^+ ground state of Ag-114. Allowed Gamow-Teller (GT) transition was estimated using the Pyatov Method (PM) and Schematic Model (SM) for even-even neutron-rich isotopes of palladium. GT-force and loft values were also compared with experimental results and studies in the literature.

Keywords— *Beta decay, Gamow-Teller transition, pn-QRPA, Pyatov Method, Woods-Saxon potential*

Introduction

Beta decay can be defined as any nuclear decay process in which the mass number (A) of the nucleus remains the same and the atomic number (Z) changes. There are three main types of beta decay. Beta (β^-) minus decay involves the emission of a negative beta particle or negative electron from the nucleus. Beta (β^+) plus decay, in which a positive beta particle or a positively charged electron is released from the nucleus. Electron capture (EC) decay does not result in any beta particle emission [4]. Due to the orbital angular momentum L carried by the β particle and the neutrino, β decay is classified as allowed (L = 0), first forbidden (L = 1). The selection rules for allowable β decay are total angular momentum change $\Delta T = \pm 0, \pm 1$ and no parity change between initial decaying and final filled states [5]. This is $\Delta T = 0$ of isospin selection for allowed Fermi transitions and $\Delta T = 0, \pm 1$ for allowed Gamow-Teller transitions. Gamow-Teller (GT) transitions in single and double beta decays play an important role in understanding nuclear structure. They also serve as tests for fundamental strong and electroweak interactions between hadrons [6]. In this paper, we used the proton-neutron quasi-particle random phase approximation (pn-QRPA) model to calculate the GT power and associated β-decay half-lives of Pd-114, taking into account new theoretical and experimental results.

Theoretical Formalism

The pn-QRPA is a widely used microscopic approach for accurate and reliable calculations of β-decay half-lives. We used the proton-neutron quasi-particle random phase approximation model to examine the effect of coupling gaps on the calculated GT power and associated β-decay half-lives. This section gives the formalities used in PM, SM, and pn-QRPA models. The schematic model Hamiltonian for GT excitations in the quasi-particle representation is given as

$$H_{SM} = H_{sqp} + h_{ph} + h_{pp} \tag{1}$$

where H_{sqp} is the single quasi-particle (sqp) Hamiltonian, h_{ph} and h_{pp} are GT effective interactions in particle-hole (ph) and particle-particle (pp) channels, respectively. The effective interaction constants in the ph and pp channels are fixed from the experimental value of the GTR energy and the β-decay log ft values between the low energy states of the parent and daughter nuclei.

The supersymmetry property of the matching part in the total Hamiltonian was restored according to the Pyatov method. Certain terms invariant with the GT operator were subtracted from the total Hamiltonian, and the commutativity of the remainder, which was disrupted by the shell model mean-area approximation, was restored by adding an effective interaction term h_0 as follows [7-8]:

$$\left[H_{SM} - \left(h_{ph} + h_{pp}\right) - (V_1 + V_C + V_{ls} + h_0, G^{\pm}_{1\mu})\right] = 0 \tag{2}$$

or

$$\left[H_{sqp} - V_1 - V_C - V_{ls} + h_0, G^{\pm}_{1\mu})\right] = 0 \tag{3}$$

where V_1, V_C, and V_{ls} are the isovector, Coulomb, and spin-orbit terms of the shell model potential, respectively. According to the Quasiboson approximation, the GT operator in quasiparticle space is given as:

$$G^{-}_{1\mu} = \sum_{np}\left[\bar{b}_{np}C^{\dagger}_{np} + (-1)^{1+\mu} b_{np}C_{np}(-\mu)\right], \tag{4}$$

$$G^{\dagger}_{1\mu} = [G^{-}_{1\mu}]^{\dagger} \tag{5}$$

where $G^{\dagger}_{np}(\mu)$ and $C_{np}(\mu)$ are the quasiboson creation and annihilation operators. The total Hamiltonian of the system concerning PM is given as:

$$H_{PM} = H_{sqp} + h_{ph} + h_0. \tag{6}$$

The $\beta^{\pm}$ reduced matrix elements are given by

$$\mathrm{B}_{\mathrm{GT}}^{(\pm)}(\mathrm{w_i}) = \sum_{\mu} \left|\mathrm{M}^{\mathrm{i}}_{\beta\pm}(0^+ \rightarrow 1_i^+)\right|^2. \tag{7}$$

Total GT- and GT+ strengths are $B(GT)_- - B(GT)_+ = 3(N - Z)$ related with the Ikeda Sum Rule; where N and Z are the numbers of neutrons and protons, respectively [9-10].

$$\mathrm{S}^{\pm} = \sum_{i} \mathrm{B}_{\mathrm{GT}}^{(\pm)}(\mathrm{w_i}) \tag{8}$$

The ft values for Gamow-Teller transitions are as follows:

$$(ft)_{\beta^{\mp}} = \frac{D}{\left(\frac{g_A}{g_V}\right)^2 4\pi B_{GT}(I_i \rightarrow I_f, \beta^{\mp})} \tag{9}$$

Results and Discussion

In this study, the broken commutation condition between the Hamiltonian of the shell model of the kernel and the Gamow-Teller operator is restored based on the Pyatov method. An efficient interaction h_0 contributed to the Hamilton operator of the system as a result of the restoration. Allowable GT β-decay half-lives were investigated for the selected Palladium isotope. GT 1^+ states in the 114-Pd isotope were investigated within the framework of the pn-QRPA method. The Chepurnov parameterized Woods-Saxon potential was used in the numerical calculations and the pairwise correlation constants for open shell cores were chosen as $C_n = C_p = 12/\sqrt{A}$. The energies were calculated from the ground state of the daughter nuclei in the calculations. The basis used in the calculations included all neutron-proton transitions that change the radial quantum number n by Δn = 0, 1, 2, 3. The reliability of our foundation was tested by calculating the Ikeda sum rule (ISR). Table 1 and Table 2 show the comparison of the calculated ISR values with the theoretically calculated results. As can be seen from the tables, the experimental and theoretical results of both logft and ISR values are close to each other.

Table 1. Logft values for Palladium-114 nucleus.

Nucleus	*Logft (exp.)*	*Logft (PM)*	*Logft (SM)*
Pd-114	4.199	4.137	4.221

Table 2. ISR values for Palladium -114 nucleus.

Nucleus	*ISR (theoretical)*	*ISR (PM)*	*ISR (SM)*
Pd-114	66	65.912	65.897

Figure 1 shows the decay of Pd-114. The 1^+ excited states in the low-energy region consist of proton-neutron quasiparticle transitions with $\Delta_n = 0$, and these transitions are weakly collectivized. An excited state of 1^+ with the largest B_{GT} value in the spectrum is considered a GTR state. The β^- transition logft values calculated by the Pyatov method were found to be close to the experimental values. This result shows how important it is to restore the disturbed commutation condition between the shell model of the kernel and the Gamow-Teller operator in the calculations.

$$^{114}_{46}Pd \longrightarrow {}^{114}_{47}Ag + e^{-} + \bar{\nu}$$

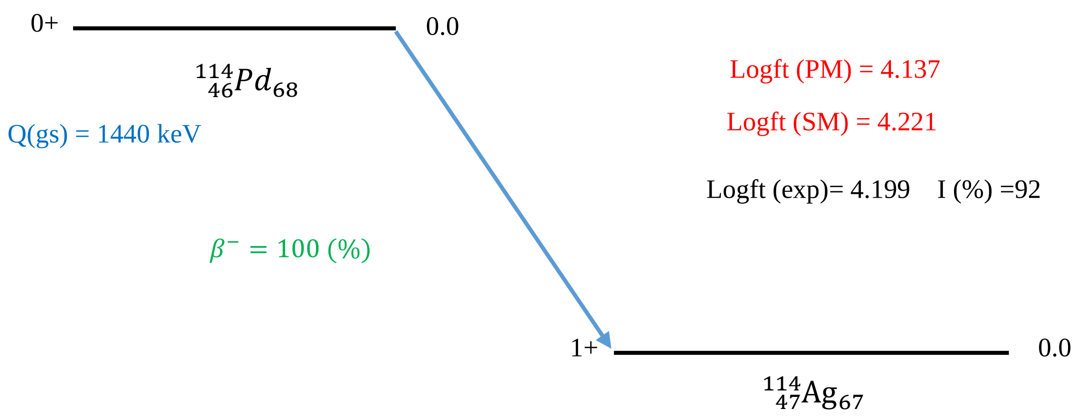

Fig. 1. The Pd-114 decay scheme taken from NUDAT [11].

References

[1] Osterfeld, F. (1992). Nuclear spin and isospin excitations. Reviews of Modern Physics, 64(2), 491.
[2] Fujita, Y., Rubio, B., & Gelletly, W. (2011). Spin–isospin excitations probed by strong, weak, and electro-magnetic interactions. Progress in Particle and Nuclear Physics, 66(3), 549-606.
[3] Suhonen, J., & Civitarese, O. (1992). Calculation of the beta decay of 114–120Pd. Quasiparticle random phase approximation results. Physics Letters B, 280(3-4), 191-197.
[4] L'Annunziata, M. F. (2016). Radioactivity: introduction and history, from the quantum to quarks. Elsevier.
[5] Berry, T. A., Podolyak, Z., Carroll, R. J., Lică, R., Grawe, H., Timofeyuk, N. K., ... & De Witte, H. (2019). Investigation of the Δn= 0 selection rule in Gamow-Teller transitions: The β-decay of 207Hg. Physics Letters B, 793, 271-275.
[6] Cheoun, M. K., Faessler, A., Šimkovic, F., Teneva, G., & Bobyk, A. (1995). Total Gamow-Teller strength, ground-state correlations and sum rules in QRPA with neutron-proton pairing. *Nuclear Physics A*, *587*(2), 301-317.
[7] Pyatov, N.I. & Salamov, D.I. (1977). Conservation laws and collective excitations in nuclei. *Nukleonika*, 22: 127-141.
[8] Cakmak, N., Unlu, S., & Selam, C. (2010). Gamow-Teller 1^{+} states in $^{112-124}$Sb isotopes. *Pramana Journal of physics*, 75:649-663.
[9] Ikeda, K., Fujii, S., & Funjita, J. I. (1963). The (p, n) reactions and beta decays. *Phys. Letters*, *3*.
[10] Cakmak, S., Nabi, J. U., Babacan, T., & Maras, I. (2015). Spin-isospin transitions in chromium isotopes within the quasiparticle random phase approximation. *Advances in Space Research*, *55*(1), 440-453.
[11] National Nuclear Data Center (2023, April 30).
https://www.nndc.bnl.gov/nudat3/getdecayscheme.jsp?nucleus=114AG&dsid=114pd%20bM%20decay&unc=nds

U1F Transition Log*ft* Value for As-74 Isotope by pn-QRPA

Najm Abdullah Saleh Saleh[1*], Mehmet Dağ[1,2], Necla Çakmak[1]

[1]*Karabük University, Faculty of Sciences, Department of Physics, Karabük, Türkiye*
[2]*Karabük University, Department of Medical Services and Techniques, Vocational School of Health Services, Karabük, Türkiye*

* Corresponding author e-mail address: najmabdola2014@gmail.com

ORCID Numbers: 0000-0001-6118-3582 (Najm Abdullah Saleh Saleh), 0000-0002-0074-307X (Mehmet Dağ), 0000-0001-5989-6663 (Necla Çakmak)

Abstract – The weak interaction is one of the four fundamental forces found in nature. It plays an important role in many astrophysical processes such as strong, electromagnetic, and gravitational forces [1]. It is well known that β decay processes are very important to understand the weak interaction processes and the nuclear structure. Although there are many theoretical and experimental studies on allowed β transitions in the literature, scientists have not shown the same interest in forbidden transitions [2]. In β decays, the energy spectrum is characterized by transitions and change in parity, where the total angular momentum in the daughter and parent nuclei differs by ΔJ = 2 units. Such decays are known as unique first forbidden (U1F) decays [3]. It was concluded that U1F transitions contributed significantly to beta decay half-lives [4]. The 2^+ ground state of tungsten As-74 decays to the 0^- ground state of Ge-74 with a probability of 66% [5]. This is a transition of the first forbidden unique type. In this study, the ft values and reduced matrix elements for the ΔJ = 2 transitions for the As-74 nuclei were calculated using proton-neutron Quasiparticle Random Phase Approximation (pn-QRPA) model. The Woods-Saxon potential is used in our calculations. The calculated the pn-QRPA formalism results were compared with the experimental results and discussed.

Keywords — *Beta decay, U1F transition, pn-QRPA, Pyatov Method, Woods-Saxon potential.*

Introduction

Major astrophysical events consist mainly and decisively of weak decay processes. Also, weak interactions play another essential function in further significant phenomena including neutralization of the stellar nucleus toward capturing electrons by free nuclei and protons. Moreover, weak interactions cause the collapse of the massive star's core, which take over into a supernova explosion. Heavier elements other than iron are formed by the effect of weak interactions through the r-process, throughout the delayed phases of enormous star development. The mass of the core is specified by weak rates and estimates for the strength of the shock wave and the fate of the shock formed by the explosion of the supernova refs. [6-17]. The pn-QRPA form was utilized by Nabi et al.[18,20] to determine the allowed weak interaction rates for the nuclei sd- shell in a stellar environment of densities (10≤ρYe (gcm−3) ≤1011) and temperatures (107 ≤T(K) ≤30 ×109). This research concentrate on the masses ranging from A = 18 -100 of 709 nuclei, the calculation of the twelve weak rates was studied for every nucleus with temperature and density function.

Muto et al. [19] found the derivation of general formalism of a proton-neutron QRPA. The measurement proceeds for phonon correlations of the Quasi Random Phase Approximation in the first-order perturbation for the transitions of the quasiparticle from parent nuclei with odd-odd and odd mass. The conservation paid attention to all provisions in the RPA order, and any particular estimations on the transitions of one-body charge-changing or on the remaining interaction are not presented. The first forbidden beta decay transition of ½+↔ ½- states were researched by Selam [21], C. (2019) for ΔJ=0 in spherical nuclei of odd mass. In this model, the probabilities of transition were investigated within the dimensionless parameter approximation (ξ-approximation) which refers to the Coulomb energy magnitude approaching to1.2ZA−1/3. In order to determine the FF transition, the Woods–Saxon potential basis in the Chepurnov parameterization was taken into account when pn-QRPA model is utilized with a schematic separable interaction. The investigating of logft values of FF transitions were in good agreement with the measured data when comparison was carried out. Çakmak, N. and Abdul utilized [22] researched some isotopes of neutron-rich Tellurium in order to study the strength of the first forbidden (|ΔJ|=0, 1, and 2) transition. The estimation of transition probabilities was carried out on the Woods-Saxon potential basis. The general formalism of a proton-neutron QRPA was considered in the ph channel (particle hole channel). The comparison between logft values of FF beta decay and experimental data showed better agreement.

Formalism

The Hamiltonian which produces the spin-isospin-dependent vibrational modes (rank 2) in odd-odd nuclei within the pn-QRPA(WS) model is specified by

$$\hat{H} = \hat{H}_{sqp} + \hat{h}_{ph} \tag{1}$$

the single quasi-particle (sqp) Hamiltonian of the system is given as follows

$$\hat{H}_{sqp} = \sum_{j\tau} \varepsilon_{j_\tau} \alpha^{+}_{j_\tau m_\tau} \alpha_{j_\tau m_\tau} \tag{2}$$

where $\boldsymbol{\varepsilon_{j_\tau}}$ and $\boldsymbol{\alpha^{+}_{j_\tau m_\tau}\alpha_{j_\tau m_\tau}}$) represent the nucleon sqp energy and the quasi-particle creation (annihilation) operators, respectively. The $\boldsymbol{\hat{h}_{ph}}$ is the spin-isospin effective interaction for U1F transition in the particle-hole (ph) channel and generally given as

$$\hat{h}_{ph} = \frac{2x_2}{g_A} \sum_{j_p\, j_n\, j_{\acute{p}}\, j_{\acute{n}}\, \mu} \left\{ b_{j_p j_n} A^{+}_{j_p j_n}(\lambda\mu) + (-1)^{\lambda-\mu} \bar{b}_{j_p j_n} A_{j_p j_n}(\lambda-\mu) \right\} \times \left\{ b_{j_{\acute{p}}\, j_{\acute{n}}} A_{\,j_{\acute{p}}\, j_{\acute{n}}}(\lambda\mu) + (-1)^{\lambda-\mu} \bar{b}_{\,j_{\acute{p}}\, j_{\acute{n}}} A^{+}_{j_{\acute{p}}\, j_{\acute{n}}}(\lambda-\mu) \right\}$$

where $\hat{h}_{ph}$ is the *ph* effective interaction constant.

$A^{+}_{j_p j_n}(\lambda\mu)$ and $A_{\,j_{\acute{p}}\, j_{\acute{n}}}(\lambda\mu)$ are the quasi-boson creation and annihilation operators and given by

$$A^{+}_{j_p j_n}(\lambda\mu) = \sqrt{\frac{2\lambda+1}{2j_p+1}} \sum_{m_p\, m_n} (-1)^{j_n - m_n} \langle j_n m_n \lambda\mu | j_p m_p \rangle \alpha^{+}_{j_p m_p} \alpha^{+}_{j_n m_n}$$

$$\left\{A^{+}_{j_p j_n}(\lambda\mu)\right\}^{\dagger} = A_{j_p j_n}(\lambda\mu)$$

The $b_{j_p j_n}$, $\bar{b}_{j_p j_n}$ are the reduced matrix elements of the non-relativistic multipole operators and defined by

$$b_{j_p j_n} = \langle\, j_p\, (l_p s_p) \| r_k \{Y_1(r_k)\sigma(k)\}_{2\mu} j_n (l_n s_n)\, \rangle\, V_{j_p} U_{j_p} ,$$
$$\acute{b}_{j_p j_n} = \langle\, j_p\, (l_p s_p) \| r_k \{Y_1(r_k)\sigma(k)\}_{2\mu} j_n (l_n s_n)\, \rangle\, V_{j_n} U_{j_n}$$

where U_{j_p} (U_{j_n})and V_{j_p} (V_{j_n}) are the standard BCS occupation amplitudes. The Hamiltonian Eq. (1) can be linearized in the pn-QRPA(WS) model. Hence the charge-exchange 2^{-} vibration modes in add-odd nuclei are considered photon excitations and are defined by

$$|\Psi_i\rangle = Q_i^{+}(\mu)|0\rangle = \sum_{j_p\, j_n} \left\{\psi^{i}_{j_p\, j_n}(\mu)\, A^{+}_{j_p\, j_n}(\lambda\mu) - \varphi^{i}_{j_p j_n}(\mu)\, A_{j_p j_n}(\lambda\mu)\right\}|0\rangle ,$$

where $Q_i^{+}(\mu)$ is the pn-QRPA phonon creation operator, $|0\rangle$ is the phonon vacuum which corresponds to the ground state of an even-even nucleus and performs $Q_i(\mu)|0\rangle = 0$ for all i. the $\psi^{i}_{j_p\, j_n}(\mu)$ and $\varphi^{i}_{j_p j_n}(\mu)$ are the forward and backwards quasi-boson amplitudes, respectively. The phonon operator satisfies the commutation relations

$$\langle 0|\left[Q_j(\mu)\, ,\; Q_j^{+}\, (\acute{\mu})\,\right]|0\rangle = \delta_{i\, j}\delta_{\mu\, \acute{\mu}} \text{ and } \langle 0|\left[Q_j(\mu)\, ,\; Q_j\, (\acute{\mu})\,\right]|0\rangle = 0$$

The quasi-boson amplitudes $\psi^{i}_{j_p\, j_n}(\mu)$ and $\varphi^{i}_{j_p j_n}(\mu)$ satisfy the orthonormalization condition

$$\sum_{j_p j_n \mu \acute{\mu}} \left\{\Psi^{i}_{j_p j_n}(\mu)\, \Psi^{\acute{i}}_{j_p j_n}(\acute{\mu}) - \varphi^{i}_{j_p j_n}(\mu)\, \varphi^{\acute{i}}_{j_p j_n}(\acute{\mu})\right\} = \delta_{i\, \acute{i}}\, \delta_{i\, \acute{i}} \qquad (3)$$

Solving equation of motion

$$[H\, , Q_i^{+}(\mu)]|0\rangle = \omega_i\, Q_i^{+}(\mu)|0\rangle \qquad (4)$$

where ωi is the ith 2− excitation energy in odd–odd nuclei which is counted from the ground state of the parent even–even nucleus. The pn-QRPA(WS) equations are taken the forms

$$\sum_{j_p j_n j_{p'} j_{n'} \mu} \left\{\rho_{j_p j_n j_{p'} j_{n'}} \psi^{i}_{j p j_n}(\mu) - \eta_{j_p j_n j_{p'} j_{n'}} \varphi^{i}_{j_p j_n}(\mu)\right\} = \omega_i \psi^{i}_{j p j_n}(\mu) \qquad (5)$$

$$\sum_{j_p j_n j_{p'} j_{n'} \mu} \left\{\eta_{j_p j_n j_{p'} j_{n'}} \psi^{i}_{j_p j_n}(\mu) - \rho_{j_p j_n j_{p'} j_{n'}} \varphi^{i}_{j_p j_n}(\mu)\right\} = \omega_i \varphi^{i}_{j_p j_n}(\mu) \qquad (6)$$

Hence $\rho_{j_p j_n j_{p'} j_{n'}}$ and $\eta_{j_p j_n j_{p'} j_{n'}}$ are the matrices of pn-QRPA(WS)

$$\rho j_p j_n j_{p'} j_{n'} = E_{j_p j_n} \delta_{j_n j_{n'}} \delta_{j_p j_{p'}} + 2\chi_2 \left\{ b_{j_p j_n} b_{j_{p'} j_{n'}} + \bar{b}_{j_p j_n} \bar{b}_{j_{p'} j_{n'}} \right\},$$

$$\eta_{j_p j_n j_{p'} j_{n'}} = -2\chi_2 (-1)^{\lambda-\mu} \left\{ b_{j_p j_n} \bar{b}_{j_{p'} j_{n'}} + b_{j_{p'} j_{n'}} \bar{b}_{j_p j_n} \right\}$$

which is $E_{jpjn} = \varepsilon_{jn} + \varepsilon_{jp}$ is the single particle energy. one could find from Eqs. (3), (5) and (6), the Excitation energies ω_i and $\psi^i_{jpj_n}(\mu)$, $\varphi^i_{j_p j_n}(\mu)$ amplitudes.

The first forbidden β- Decay transitions can be defined in terms of multipole operator. For the transitions $2^- \to 0^+$ these are

$$M^{U1F}_{\beta^\mp} = M^\mp(J_A, K = 1, \lambda = 2, \mu) = g_A \sum_{k=1}^{A} t_\pm(k) r_k \{Y_1(r_k)\sigma(k)\}_{2\mu} \quad (7)$$

$M^{U1F}_{\beta^\mp} = M^\mp(J_A, K = 1, \lambda = 2, \mu)$ is the non-relativistic unique first forbidden β −Decay multipole operator. All symbols have their usual meanings.

The transitions probability $B(I_i \to I_f \beta^\mp)$ is described by the reduced matrix element of the multipole operator (Eq. (7)). Thus, we may write

$$B(I_i \to I_f, \beta^\mp) = \frac{1}{2I_i+1} \left| \langle I_f \| M^\mp(j_A, k = 1, \lambda = 2) \| I_i \rangle \right|^2 \quad (8)$$

The reduce matrix elements $\langle 2_i^- \| M_{\beta^\mp} \| 0^+ \rangle$ within the framework of the pn-QRPA(WS) method are given as

$$\langle 2_i^- | M_{\beta^-}(\acute{\mu}) | 0^+ \rangle = \langle 0^+ | [Q_i(\mu), M_{\beta^-}(\acute{\mu})] | 2 \rangle = \sum_{j_p j_n} \delta_{\mu\acute{\mu}} \left\{ b_{j_p j_n} \psi^i_{j_p j_n}(\mu) + \acute{b}_{j_p j_n} \varphi^i_{j_p j_n}(\mu) \right\},$$

$$\langle 2_i^- | M_{\beta^+}(\acute{\mu}) | 0^+ \rangle = \langle 0^+ | [Q_i(\mu), M_{\beta^+}(\acute{\mu})] | 2 \rangle = \sum_{j_p j_n} \delta_{\mu\acute{\mu}} \left\{ \acute{b}_{j_p j_n} \psi^i_{j_p j_n}(\mu) + b_{j_p j_n} \varphi^i_{j_p j_n}(\mu) \right\}.$$

Transitions with $\lambda = n + 1$ are referred to as unique first forbidden transitions ref. [21], and the ft values are expressed as

$$(f\ t)_{\beta^\mp} = \frac{D}{(g_A/g_V)^2\, 4\pi\, B(I_i \to I_f,\ \beta^\mp)} \frac{(2n+1)!!}{[(n+1)!]^2 n!}$$

$$D = \frac{2\pi^3 \hbar^3 ln2}{g_v^2 m_e^5 c^4} = 6250\ sec, \frac{g_A}{g_v} = -1.254.$$

Results and Conclusion

The unique first forbidden U1F (|ΔJ| = 2) transition by using the pn-QRPA model with the Woods–Saxon (WS) potential basis was considered in this work. In numerical calculation done by the FTN77 programme did not use the quenching factor. The pair correlation function was chosen as $C_n = C_p = {}^{12}/_{\sqrt{A}}$ for the open-shell nuclei. The energies were calculated from the ground state of daughter nuclei in all calculations. The main contributions to the strength are situated at energies of the order (21–25) MeV and show the position of the giant FF resonance (FFR) in our calculations with $I^{\pi} = 2^{-}$. The pn-QRPA (WS) model result is in better agreement with the measured log*ft* value. The matrix element of non-relativistic β-moment is the major source of the orders of magnitude disagreement with the experimental data. This study may contribute to accelerating the r-process nucleosynthesis calculation.

Table 1. $^{74}_{33}\boldsymbol{As}$ nuclear properties [23]

Nuclide	Energy [keV]	J^{π}	Decay Modes BR [%]		Q_{β^-}[keV]	Q_{EC}	S_n	S_p	*Binding/A*
$^{74}_{33}\boldsymbol{AS}_{41}$	*0.0*	2^{-}	*Ec*, $\boldsymbol{\beta^-}$ $\boldsymbol{\beta^+}$	66 34	*1353.1*	*2562.4*	*7979*	*6851.5*	*8680.002*

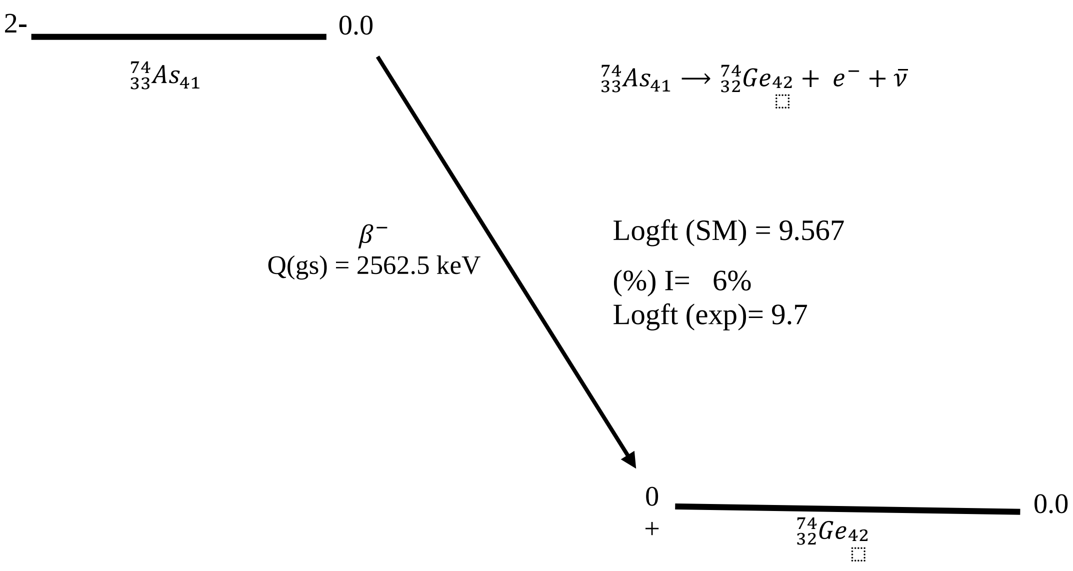

Fig. 1. The $^{74}_{33}As_{41}$ decay scheme from taken NUDAT [13]

References

[1] Langanke, K., & Martínez-Pinedo, G. (2003). Nuclear weak-interaction processes in stars. Reviews of Modern Physics, 75(3), 819.
[2] Cakmak, N., Manisa, K., Unlu, S., & Selam, C. (2010). The investigation of 0+↔ 0− β decay in some spherical nuclei. Pramana, 74, 541-553.
[3] Glick-Magid, A., Mishnayot, Y., Mukul, I., Hass, M., Vaintraub, S., Ron, G., & Gazit, D. (2017). Beta spectrum of unique first-forbidden decays as a novel test for fundamental symmetries. Physics Letters B, 767, 285-288.
[4] Nabi, J. U., Çakmak, N., Majid, M., & Selam, C. (2017). Unique first-forbidden β-decay transitions in odd–odd and even–even heavy nuclei. Nuclear Physics A, 957, 1-21.
[5] Balraj Singh, Ameenah R. Farhan, Nuclear Data Sheets 107, 1923 (2006).
[6] I.N. Borzov. (2006). Beta-decay rates. Nucl. Phys., A,777, 645-675.
[7] J.-U. Nabi. (2010). Adv. Space Res. 46. 1191–1207.
[8] K. Muto, et al., Z. Phys. A 341 (1992) 407.
[9] A. Bohr, B.R. Mottelson, Nuclear Structure, vol. 1, Benjamin, W.A. Inc., New York, 1969.
[10] H. Homma, et al., Phys. Rev. C 54 (1996) 2972.
[11] J.-U. Nabi, H.V. Klapdor-Kleingrothaus, At. Data Nucl. Data Tables 71 (1999) 149.
[12] J.-U. Nabi, H.V. Klapdor-Kleingrothaus, At. Data Nucl. Data Tables 88 (2004) 237.
[13] J.-U. Nabi, N. Cakmak, Z. Iftikhar, Eur. Phys. J. A 52 (1) (2016).
[14] J. Engel, P. Vogel, M.R. Zirnbauer, Phys. Rev. C 37 (1988) 731.
[15] K. Muto, E. Bender, H.V. Klapdor, Z. Phys. A 334 (47) (1989).
[16] P. Möller, J.R. Nix, At. Data Nucl. Data Tables 26 (1981) 165.
[17] G. Audi, et al., Chin. Phys. C 36 (2012) 1287.
[18] Nabi, J.-Un, Cakmak, N., Majid, M. and Selam, C., Nuclear Physics A 957 (2017).
[19] Muto, K., Bender, E., & Klapdor, H. V. (1989). Proton-neutron quasiparticle RPA and charge-changing transitions. Zeitschrift für Physik A Atomic Nuclei, 333(2), 125-129.
[20] Nabi, J. U., & Klapdor-Kleingrothaus, H. V. (1999). Weak interaction rates of sd-shell nuclei in stellar environment calculated in the proton-neutron quasiparticle random phase approximation. arXiv preprint nucl-th/9907106.
[21] Selam, C. (2019). First Forbidden Beta Transitions of ½+↔ ½-States forΔ J= 0 In Spherical Odd Mass Nuclei. ALKÜ Fen Bilimleri Dergisi, 174-182.
[22] Çakmak, N., & Abdul, M. (2019). First forbidden-Decay logft values of neutron rich Te isotopes. ALKÜ Fen Bilimleri Dergisi
[23] https://www-nds.iaea.org/ (2023, May,9).
[24]National Nuclear Data Center (2023,April,28). https://www.nndc.bnl.gov/nudat3/getdecayscheme.jsp?nucleus=44CA&dsid=44k%20bM%20decay%20(22.13%20m)&unc=nds.

Full-Text Contributions

NO	FIRST NAME	LAST NAME	AFFILIATION	COUNTRY	PARTICIPANT
1	Khusniddin K.	Olimov	Physical-Technical Institute of Uzbekistan Academy of Sciences	Uzbekistan	Invited Speaker
2	Serkan	Akkoyun	Sivas Cumhuriyet University	Türkiye	Invited Speaker
3	Dennis	Bonatsos	Institute of Nuclear and Particle Physics, NCSR	Greece	Speaker
4	Abdurahman	Büber	Kırıkkale University	Türkiye	Speaker
5	Mahmut	Böyükata	Kırıkkale University	Türkiye	Participant
6	Aybaba	Hançerlioğulları	Kastamonu University	Türkiye	Participant
7	Rezvan	Rezaeizadeh	University of Guilan	İran	Speaker
8	İlknur	Şahin	Kastamonu University	Türkiye	Participant
9	Igor A.	Lebedev	Institute of Physics and Technology, Satbayev University	Kazakhstan	Participant
10	Anastasiya I.	Fedosimova	Institute of Physics and Technology, Satbayev University	Kazakhstan	Participant
11	Fu-Hu	Liu	Institute of Theoretical Physics & Collaborative Innovation Center of Extreme Optics & State Key Laboratory of Quantum Optics and Quantum Optics Devices, Shanxi University	China	Participant
12	Elena	Dmitriyeva	National University of Science and Technology MISIS	Uzbekistan	Participant
13	Kobil A.	Musaev	Physical-Technical Institute of Uzbekistan Academy of Sciences	Uzbekistan	Participant
14	Kosim	Olimov	Physical-Technical Institute of Uzbekistan Academy of Sciences	Uzbekistan	Participant
15	Bekhzod S.	Yuldashev	Institute of Nuclear Physics of Uzbekistan Academy of Sciences	Uzbekistan	Participant
16	Tuncay	Bayram	Karadeniz Technical University	Türkiye	Participant
17	Büruce	Öztürk	Sakarya University	Türkiye	Speaker
18	Hakan	Yakut	Sakarya University	Türkiye	Participant
19	Elif	Kemah	Sakarya University	Türkiye	Participant
20	Sobir A.	Turakulov	Institute of Nuclear Physics – Academy of Sciences	Uzbekistan	Participant
21	Alisher S.	Kadyrov	Curtin University	Australia	Participant
22	Cafer Mert	Yeşilkanat	Artvin Çoruh University	Türkiye	Participant
23	Abdulrahman Ahmed	Mustafa	Karabük University	Türkiye	Participant
24	Khalid Hadi Mahdi	Aal-Shabeeb	Karabük University	Türkiye	Speaker
25	Najm Abdullah Saleh	Saleh	University of Duhok	Iraq	Speaker
26	Mehmet	Dağ	Karabük University	Türkiye	Speaker
27	Necla	Çakmak	Karabük University	Türkiye	Participant
28	Boburbek J.	Tukhtaev	Physical-Technical Institute of Uzbekistan Academy of Sciences	Uzbekistan	Participant
29	Azizjon	Tokhirov	Physical-Technical Institute of Uzbekistan Academy of Sciences	Uzbekistan	Participant

31	Sh. A.	Khudaiberdyeva	Institute of Physics and Technology, Satbayev University	Kazakhstan	Participant
32	Andriana	Martinou	Institute of Nuclear and Particle Physics, NCSR	Greece	Participant
33	Spyridon	Peroulis	Institute of Nuclear and Particle Physics, NCSR	Greece	Participant
34	Theo	Mertzimekis	National and Kapodistrian University of Athens	Greece	Participant
35	Nikolay	Minkov	Institute of Nuclear Research and Nuclear Energy, Bulgarian Academy of Sciences	Bulgaria	Participant
36	Nihal	Büyükçizmeci	Selçuk University	Türkiye	Participant